2004

Broadband counter-wound helix antenna for land mine detection

Shivandas, Dilipkumar

Monterey California. Naval Postgraduate School

http://hdl.handle.net/10945/1632

NAVAL POSTGRADUATE SCHOOL

MONTEREY, CALIFORNIA

THESIS

BROADBAND COUNTER-WOUND HELIX ANTENNA FOR LAND MINE DETECTION

by

Dilipkumar Shivandas

March 2004

Thesis Advisor: David C. Jenn
Second Reader: Daniel C. Schleher

Approved for public release, distribution is unlimited.

THIS PAGE INTENTIONALLY LEFT BLANK

REPORT DOCUMENTATION PAGE			*Form Approved OMB No. 0704-0188*
Public reporting burden for this collection of information is estimated to average 1 hour per response, including the time for reviewing instruction, searching existing data sources, gathering and maintaining the data needed, and completing and reviewing the collection of information. Send comments regarding this burden estimate or any other aspect of this collection of information, including suggestions for reducing this burden, to Washington headquarters Services, Directorate for Information Operations and Reports, 1215 Jefferson Davis Highway, Suite 1204, Arlington, VA 22202-4302, and to the Office of Management and Budget, Paperwork Reduction Project (0704-0188) Washington DC 20503.			
1. AGENCY USE ONLY *(Leave blank)*	**2. REPORT DATE** March 2004	**3. REPORT TYPE AND DATES COVERED** Master's Thesis	
4. TITLE AND SUBTITLE: Title (Mix case letters) Broadband Counter-wound Helix Antenna for Land Mine Detection			**5. FUNDING NUMBERS**
6. AUTHOR(S)			
7. PERFORMING ORGANIZATION NAME(S) AND ADDRESS(ES) Naval Postgraduate School Monterey, CA 93943-5000			**8. PERFORMING ORGANIZATION REPORT NUMBER**
9. SPONSORING /MONITORING AGENCY NAME(S) AND ADDRESS(ES) N/A			**10. SPONSORING/MONITORING AGENCY REPORT NUMBER**
11. SUPPLEMENTARY NOTES The views expressed in this thesis are those of the author and do not reflect the official policy or position of the Department of Defense or the U.S. Government.			
12a. DISTRIBUTION / AVAILABILITY STATEMENT Approved for public release, distribution is unlimited.			**12b. DISTRIBUTION CODE**

13. ABSTRACT (maximum 200 words)

Ground penetrating radars (GPRs), also known as subsurface radars, are used in many applications including detection of land mines and unexploded ordnance (UXO). Despite significant long-term investment in GPRs for mine and UXO detection, it remains true that no GPR system that meets operational requirements has yet been fielded; however, recent advances in several mine detection radars under development have produced significant improvements in detection performance and false-alarm mitigation over what was achievable only a few years ago. This research examines the suitability of modeling helical antennas to achieve a broadband characteristic for GPR implementation. Although the two-arm counter-wound helix provides the required spot illumination, it is expected that more arms may have to be added to reduce the radiation in the back direction and to match the input impedance to the feed line. Microwave Design Studio (MDS) has been used extensively to simulate the broadband characteristics of the helical antenna. An overall design strategy is outlined, together with a more detailed treatment of the ground penetrating radar subsystems and topics that are relevant to effective subsurface radar operation. These include soil characterization, the choice of the frequency of operation, as well as the design and construction of suitable helical antennas.

Finally, a new antenna structure called the counter-wound quadrifilar helical antenna (CQHA), which is suitable for subsurface radar applications, is examined. The counter-wound quadrifilar helical antenna has a broad bandwidth and a linear polarization with a controllable plane of polarization from a planar geometry.

14. SUBJECT TERMS Subsurface Radar, Ground Penetrating Radar System, GPR, Helical Antennas, Helix, Ground Dielectric Properties			**15. NUMBER OF PAGES** 111
			16. PRICE CODE
17. SECURITY CLASSIFICATION OF REPORT Unclassified	**18. SECURITY CLASSIFICATION OF THIS PAGE** Unclassified	**19. SECURITY CLASSIFICATION OF ABSTRACT** Unclassified	**20. LIMITATION OF ABSTRACT** UL

NSN 7540-01-280-5500

Standard Form 298 (Rev. 2-89)
Prescribed by ANSI Std. 239-18

THIS PAGE INTENTIONALLY LEFT BLANK

**BROADBAND COUNTER-WOUND HELIX ANTENNA
FOR LAND MINE DETECTION**

Dilipkumar Shivandas
MAJOR, Republic of Singapore Air Force
Bachelor of Engineering (Hons), Nanyang Technological University, 1995

Submitted in partial fulfillment of the
requirements for the degree of

MASTER OF SCIENCE IN SYSTEMS ENGINEERING

from the

**NAVAL POSTGRADUATE SCHOOL
March 2004**

Author: Dilipkumar Shivandas

Approved by: David C. Jenn
Thesis Advisor

Daniel C. Schleher
Second Reader

Dan C. Boger
Chairman, Department of Information Sciences

THIS PAGE INTENTIONALLY LEFT BLANK

ABSTRACT

Ground penetrating radars (GPRs), also known as subsurface radars, are used in many applications including detection of land mines and unexploded ordnance (UXO). Despite significant long-term investment in GPRs for mine and UXO detection, it remains true that no GPR system that meets operational requirements has yet been fielded; however, recent advances in several mine detection radars under development have produced significant improvements in detection performance and false-alarm mitigation over what was achievable only a few years ago. This research examines the suitability of modeling helical antennas to achieve a broadband characteristic for GPR implementation. Although the two-arm counter-wound helix provides the required spot illumination, it is expected that more arms may have to be added to reduce the radiation in the back direction and to match the input impedance to the feed line. Microwave Design Studio (MDS) has been used extensively to simulate the broadband characteristics of the helical antenna. An overall design strategy is outlined, together with a more detailed treatment of the ground penetrating radar subsystems and topics that are relevant to effective subsurface radar operation. These include soil characterization, the choice of the frequency of operation, as well as the design and construction of suitable helical antennas.

Finally, a new antenna structure called the counter-wound quadrifilar helical antenna (CQHA), which is suitable for subsurface radar applications, is examined. The counter-wound quadrifilar helical antenna has a broad bandwidth and a linear polarization with a controllable plane of polarization from a planar geometry.

THIS PAGE INTENTIONALLY LEFT BLANK

TABLE OF CONTENTS

LIST OF FIGURES

THIS PAGE INTENTIONALLY LEFT BLANK

LIST OF TABLES

THIS PAGE INTENTIONALLY LEFT BLANK

ACKNOWLEDGMENTS

I would first like to express my sincere appreciation towards Professor David C. Jenn to whom I am especially grateful for his guidance, support and supervision throughout this thesis. I also want to thank Professor Daniel C. Schleher for his advice and proofreading this report.

Additionally, I would like to thank my loving wife Vandana and my mum, for their unrelenting support, patience and encouragement without which I would not be able to complete my program in NPS successfully.

Lastly, I must thank my sponsor, RSAF, for providing me with this opportunity to pursue my postgraduate studies here at the Naval Postgraduate School.

THIS PAGE INTENTIONALLY LEFT BLANK

I. INTRODUCTION

A. BACKGROUND

The widespread use of land mines to impede the movement of troops traces roughly to World War I, although the history of mines dates back to 1277 when the Chinese used contact- fused explosive devices to repel the invading Mongols [1]. Widely published reports estimate that there are 110 million land mines in 70 countries [2]. Although chronic land mine problems exist around the world, the deployment of U.S. troops to Bosnia in 1995 and to Afghanistan in 2001 gave the land mine issue a particular sense of urgency. The U.S. Army has several ongoing programs in land mine detection technology development and actively evaluates the efficacy of individual sensors and integrated systems [2].

Very little technology is currently employed in the real world for the detection of land mines. Metal detectors are effective against metal-cased land mines, but many land mines are plastic cased, and there is no sensitive and reliable plastic mine detector. As such, when technical solutions to detecting land mines are discussed, it is almost always in the context of ongoing technology development, testing, and evaluation, not in the context of real-world deployment or de-mining activities [2]. The most heavily mined countries are among the poorest, and clearly cannot afford research and development programs for technology development. Most of the funding for land mine detection technology development originates from the U.S. Army where the lives of its men and women are taken very seriously [2].

Despite significant long-term investment in Ground Penetrating Radars (GPR) for mine and unexploded ordnance (UXO) detection, it remains true that at this time no GPR system that meets operational requirements has yet been fielded; however, recent advances in several mine detection radars under development have produced significant improvements in detection performance and false-alarm mitigation over what was achievable only a few years ago [3]. One of the most crucial and technological challenging components of the system is the antenna. It is thus imperative for an antenna to possess features that will enable it to perform its functions as a GPR. Such features

include wide bandwidth, operating close to the surface for subsurface penetration, adequate gain and resolution, and dual linear polarization. This research examines the suitability of helical antennas to achieve the desired characteristics for GPR applications.

B. PREVIOUS RESEARCH

Ground penetrating radar is a geophysical method that has been developed over the past thirty years for shallow, high-resolution, subsurface investigations of the earth. GPR has generated a great deal of debate since it was first introduced as a non-destructive testing tool in the field of geo-technical and civil engineering. Ground penetrating radars, like any other geophysical tool, depend on recognizing the limitations of the system as well as the positive potential. Applications include utility location, road and airport runway inspection, detection of land mines and UXO, mapping of groundwater contamination, archeology, avalanche victim search and other shallow investigations. While early GPR applications aimed at mapping subsurface discontinuities (e.g. depth to groundwater table, ice thickness), there is an increasing demand for GPR systems that are able to detect small (down to several centimeters) objects, such as landmines, and possibly to identify them.

Detection capability has been demonstrated for a number of radar implementations, particularly for close-in geometries and for metallic targets. In real-world tests, however, GPR is known to consistently suffer from prohibitively high false-alarm rates (FAR). Sensor design and performance requirements differ for specific applications of GPR to various counter-mine and UXO mission areas. Mine detection and UXO detection differ greatly in terms of the physical characteristics of the targets, environments, and depths at which targets will be found and to which detection must be accomplished.

The principle of GPR is broadly similar to seismic reflection profiling. The GPR system sends electromagnetic radiation pulses into the ground via a transmitting antenna, the resulting wavefront is partially reflected by changes in bulk electrical properties of the ground, and a receiving antenna picks up the reflection. The signals are processed and amplified to provide a time-travel record. This time-travel record is effectively a pseudo

cross-section of the ground. It is not a true section. A skilled interpreter is required to distinguish between noise and real data, and to recognize the characteristic radar signatures of certain items.

To be operationally effective, a GPR system entails: (i) the efficient coupling of the electromagnetic energy to the ground, (ii) adequate penetration of the ground with regard to the target depth, (iii) sufficient scattering from targets, and (iv) adequate bandwidth with regard to resolution and noise levels [4]. Figure 1 illustrates the various interaction mechanisms between the different subsystems of a typical GPR.

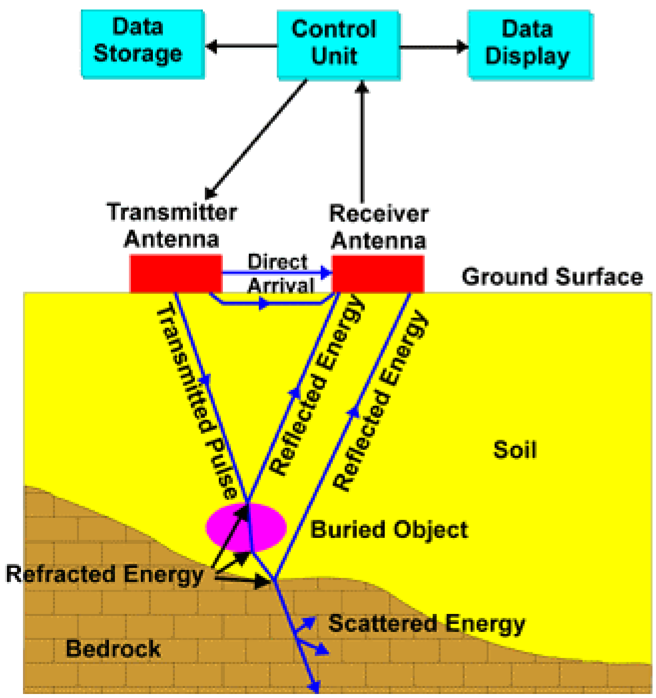

Figure 1. **Interactions between subsystems in a typical GPR.**

In GPR applications, very often the antenna is placed directly over the ground with its axis normal to the surface without contacting the surface of the earth, as illustrated in Figure 1. This allows rapid surveying of the subsurface during operation. For this application, antennas with uniform properties such as input impedance, gain, and linear polarization over a wide bandwidth are desirable, especially when the transmitted and received signal has a very large bandwidth. The counter-wound helical antenna discussed here has these characteristics in free space, and they are preserved to a great

degree when placed over the ground. Olhoeft [5] discussed several applications and frustrations in using ground penetrating radar systems.

C. THESIS OVERVIEW

The thesis is organized as follows. Chapter II discusses the primary differences between land mines and UXOs and the detection techniques employed for detecting them. It reviews the characteristics of ground penetrating radars, highlighting those features that differ from conventional radar techniques. Lastly it introduces the various considerations and limiting factors for a GPR system that predominantly depend upon parameters such as type and texture of soil, soil water content, electrical properties of soil, soil density and operating frequency. Chapter III commences with the discussion of a monofilar (single-arm) helical antenna and proceeds with a brief introduction of bifilar (dual-arm), quadrifilar (four-arm), counter-wound and non-counter-wound helical antennas, illustrating the important antenna parameters. A simple design of a Counter-wound Quadrifilar Helical Antenna (CQHA) that fulfills the requirements for a GPR-based antenna system and its characteristics is then discussed in detail. Chapter IV presents the simulation results and provides an analysis, illustrating its performance with simulation results using Microwave Studio. Chapter V presents a summary and proposes prospective developmental work in this field.

II. GPR SYSTEMS AND OPERATIONAL PARAMETERS

This chapter discusses the principal features affecting the operation and design of ground penetrating radars highlighting those features that differ from conventional radar techniques. The primary differences between land mines and UXOs, and the detection techniques employed for detecting them are examined. Lastly, this chapter introduces the various considerations and limiting factors for a GPR system that predominantly depend upon parameters such as type and texture of soil, soil water content, electrical properties of soil, soil density and operating frequency. The description is predominantly narrative. More detailed information pertaining to both system design and operation can be found in the referenced technical papers.

A. GPR APPLICATIONS

The underlying principles of GPR have been known since the beginning of the twentieth century [6,7]. GPR refers to a wide range of electromagnetic (EM) techniques designed to locate objects or interfaces buried beneath the earth's surface. Applications that drive the system design are listed in Table 1.

Application	Depth/range of interest*
Archeology	Short to medium
Wall thickness and hidden objects in walls*	Short
Unexploded ordinance and mines	Short to medium
Pipes and underground structures	Medium
Ice thickness	Long

*short: $d < 1/2\,m$; medium: $1/2 < d < 25\,m$; long: $d > 25\,m$ to hundreds of meters

Table 1. **Range of GPR application techniques (from [5]).**

In essence, the same techniques as conventional free space radar can be used, but there are four unique issues to be addressed. The first is efficient EM coupling into the ground. Ideally a surface should be smooth as possible; it need not be flat or level. In

some circumstances ground preparation by cutting back brush, or smoothing with a mechanical excavator may be required. Second, adequate radiation penetration of the signal through the ground to the target and back is necessary. Signal loss varies according to the composition of the ground especially when the ground is moist and the radar operates above 1 GHz. Third, a sufficiently large return from dielectric or metal discontinuities (targets) must be obtained to enable detection at the surface. The more different the target is from the surrounding material, the more likely the radar will pick up the difference. Finally, adequate bandwidth with regard to resolution and noise levels is required [4].

B. UNEXPLODED ORDNANCE AND LAND MINE DETECTION

1. Unexploded Ordnance

First, it is necessary to distinguish between unexploded ordnance and land mines. In general, UXO refers to bombs that were dropped from planes, or fired from rocket launchers, whose fuses did not detonate when they hit the ground. A major caliber ordnance item such as a 500-lb. bomb can dive 15 ft into the soil when dropped from a plane during a bombing exercise. Because the fuses on these items are impact fuses, the presence of these UXO is accidental; that is, they are there because they were duds [2]. They are not designed to blow up when stepped on or driven over. Thus, clearing for UXO is generally accomplished via a sweep with handheld metal detectors, without the grave danger associated with stepping on land mines. That is not to say that UXO clearance is not dangerous. There are UXO items that blur the line between bombs and mines. “Bombies” or bomblets are individual items disseminated by a cluster bomb that contain ball bearings. Like land mines, bombies have extremely sensitive fuses and can easily blow up when disturbed [2].

Improved technological efforts to detect UXO have been developed which use vehicle-deployed arrays of GPS-integrated metal detectors. These sensors can be towed behind a vehicle because UXO do not detonate when driven over, unlike land mines. Data collected are later post-processed, and any magnetic anomalies can be detected,

analyzed, located, and removed. Figure 2 illustrates a small, light, aluminum vehicle tows a magnetometer array integrated with a global positioning system (GPS).

Figure 2. **A digital geophysical mapping system for detection of UXO (from [2]).**

In contrast, clearance of land mines has historically been more of a post-conflict concern, and as such, funding for technology development for detection of antipersonnel mines has traditionally arisen from organizations such as the U.S. Department of State and the United Nations [2].

2. Antitank and Antipersonnel Mines

Land mines are divided into two broad classes: (1) antitank (AT) mines, which are designed to impede the progress of or destroy vehicles, and (2) antipersonnel (AP) mines, which are designed to kill and maim people. Most of the land mine-related activities that make it into the public eye (the Campaign to Ban Land Mines), concentrates on antipersonnel mines, as these are the most widespread and have the highest human cost. However, the majority of the funding to develop land mine detection technology has been targeted at antitank mines [2].

As shown in Figure 3, land mines come in a variety of shapes and sizes. They can be square, round, cylindrical, or bar shaped. The casing can be metal, plastic, or wood. However, this is not a completely binary function; even on a plastic land mine, the fusing

mechanism can have varying degrees of metal. Some literature categorizes mines slightly differently as metal, low metal (or minimum metal), and nonmetallic.

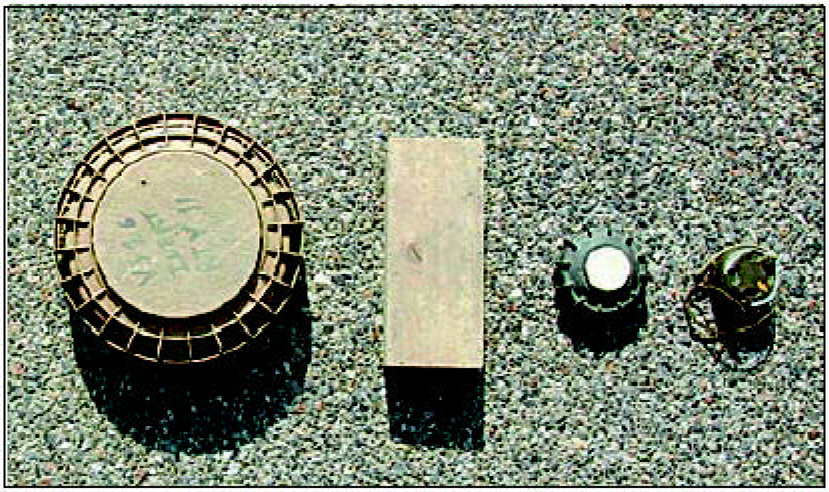

Figure 3. **Left to right, VS1.6 plastic AT mine, PMD6 wood AP mine, VS50 plastic AP mine, and M14 plastic AP mine (before removal of metal fuse clip). The M14 is roughly two inches across (from [2]).**

Although the same basic sensing technologies are used for AT and AP land mine detection, there are important differences in terms of scope and strategy. AT mines range from about 6 to 14 inches (15 to 35 cm) in size. They are typically buried up to 16 inches (40 cm) deep, but they can also be deployed on the surface of a road to block a column of machinery. They contain roughly 5 to 10 kg of explosive (TNT or RDX) [8], the explosion of which can demolish a vehicle. AT mines can be metal or plastic. AP mines range from about 2 to 6 inches (5 to 15 cm) in size; an M14 antipersonnel mine is the size of a hockey puck. They can be metal, plastic, or wood; the PMD-6 AP mine is simply a box of TNT with a fuse. AP mines are typically buried extremely shallow, detonated by very low pressure, and designed to kill or maim people.

3. Sensors Employed

If all mines were metal cased or had substantial metallic content, all that would be required for detection are metal detectors. The widespread use of plastic land mines necessitates development and deployment of additional detection technologies. Because

there is no such thing as a reliable and sensitive plastic detector, other sensors attempt to exploit ancillary disturbances in the background, such as thermal, chemical, or dielectric.

a. Metal Detectors

Metal-cased land mines are readily detected with a metal detector. While the metal used in land mine casing is typically ferrous and thus would be detected by a magnetometer, which is a passive sensor, typically an active pulsed induction-type (PI) metal detector can be employed. PI sensors use a coil to transmit an electromagnetic pulse and then receive and detect any current induced by the pulse in subsurface metallic objects, hence the term "pulsed induction" [2]. Essentially the same technology as coin detectors used by hobbyists on the beach, these PI detectors are commercially available and lightweight.

However, plastic-encased land mines pose a problem for metal detectors. These mines contain varying degrees of metal. If the fuse is metal, the mine may be easily detectable. But if only the detonating tube and firing pin (weighing approximately 0.6 g in an M14, and even less—0.35 grams—in a PMA3 [2]) are metal, the mine may not be detectable. A high-sensitivity metal detector may be able to detect this firing pin if the sensitivity is adjusted appropriately. However, the resulting false alarm rate, particularly in metal-cluttered areas such as war zones, can be extremely high. Metal detectors can also have difficulty in urban environments where there is a lot of background metal such as rebar-reinforced concrete and can generate false readings in soil with high metallic content.

b. Ground Penetrating Radar

Because of the difficulty in detecting the tiny amounts of metal in a plastic land mine with a metal detector, technology development has been moved towards ground penetrating radars [2]. When parameters such as frequency range, antenna size, antenna separation, and system timing are optimized for detection of mine-sized objects in the near subsurface, GPR is quite effective in detecting both metal and plastic land mines in a variety of soils [2]. The depth of penetration is a function of both the

frequency range produced and the soil attenuation. Lower frequency components penetrate further, but it is the higher-frequency components that are necessary to image and resolve smaller targets. Both impulse-based and swept frequency GPR systems are widely used. Generally a system with a bandwidth of roughly 1 to 4 GHz is effective for detection of land mines [2].

Ultimately, GPR images the dielectric properties of the soil, and any discontinuities appear as a signal. If soil were perfectly homogeneous, a discontinuity caused by a land mine would stand out as an anomaly against the background. Unfortunately, even under near-ideal test track conditions, soil itself is a remarkably inhomogeneous medium, and false alarms are easily generated from the background itself.

Because of this, automatic target recognition (ATR) algorithms employed by GPR-based systems typically calculate and remove background and try to detect the hyperbolic signatures that are characteristic in size and shape of land mine targets. Figure 4 demonstrates a GEO-CENTERS 400 Series energy focusing ground penetrating radar (EFGPR), which employs a fuzzy logic-based algorithm that use prototypes, or feature sets, for land mines, and prototypes for clutter [9]. The output is a plan view of the probability that at each point along a test lane, there is a land mine. A blob detector then runs on this confidence plan view, outputting target reports when a blob is of an appropriate size and shape [2]. The upper left shows a raw scan, cross-track, and into the ground. The vertical strip on the left shows the total reflected energy along a test track. The strip on the right shows the confidence plan view, which incorporates the results of the fuzzy logic-based ATR algorithms. The upper and lower right images, respectively, show the raw and contrast-enhanced classic hyperbolic signature of an antitank land mine.

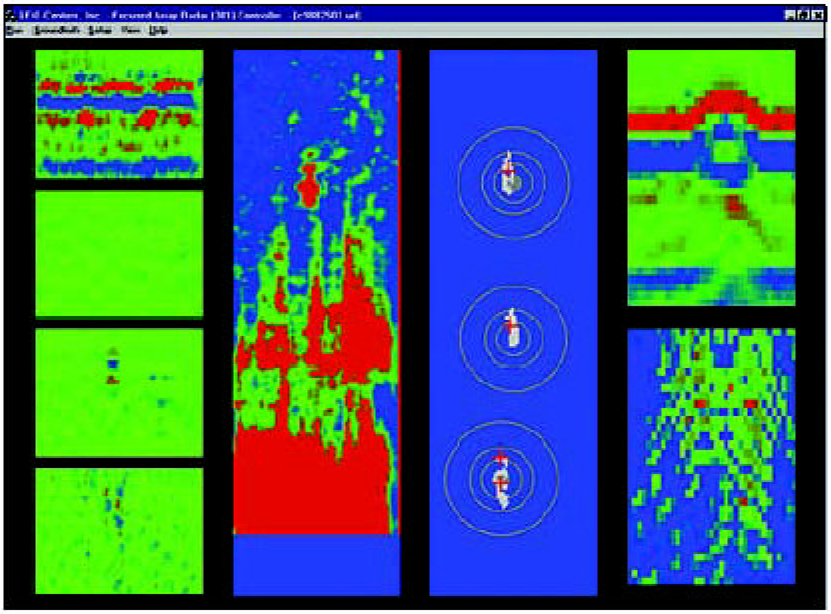

Figure 4. **Screen shot of host software from GEO-CENTERS GPR (from [2]).**

C. CONSIDERATIONS FOR GPR SYSTEMS

GPR design is complex and challenging because of the variety of hardware and system choices and the possible combinations of many of those choices, as depicted in Figure 5.

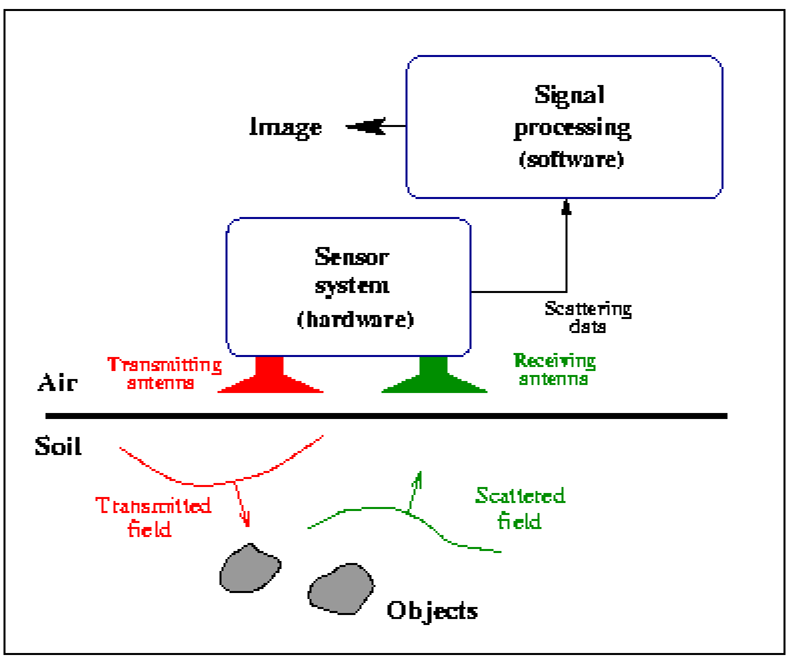

Figure 5. **Hardware and software functions for the sensor system and signal processing.**

Most GPR systems used for land mine detection are bi-static [2]; that is, they employ separate transmit and receive antennas, as illustrated in both Figure 5 and Figure 6. The transmitter sends out a series of electromagnetic pulses and then listens with the receiver connected to a high-speed sampler, which in turn feeds an analog-to-digital converter. The GPR antenna is typically moved forward along a test track. An example of such a GPR system developed by GEO-CENTERS is shown in Figure 7. An object in the near subsurface reflects the transmitted wave back to the receiver. As the array is moved forward, it gets closer to the object, and the reflection appears sooner. This traces out the traditional hyperbolic-shaped signature typically obtained with GPR, which is similar to image data from other geophysical sensors such as seismic or acoustic. A variety of signal processing techniques are typically employed to calculate and subtract background and to enhance the signal [2].

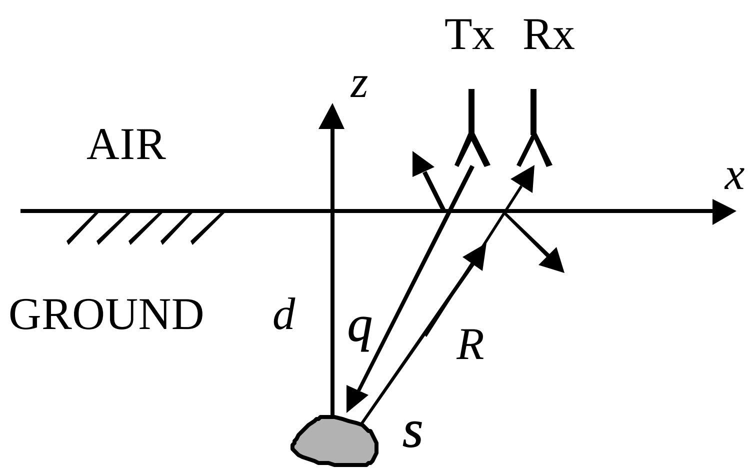

Figure 6. **Generic bi-static GPR-based system (from [4]).**

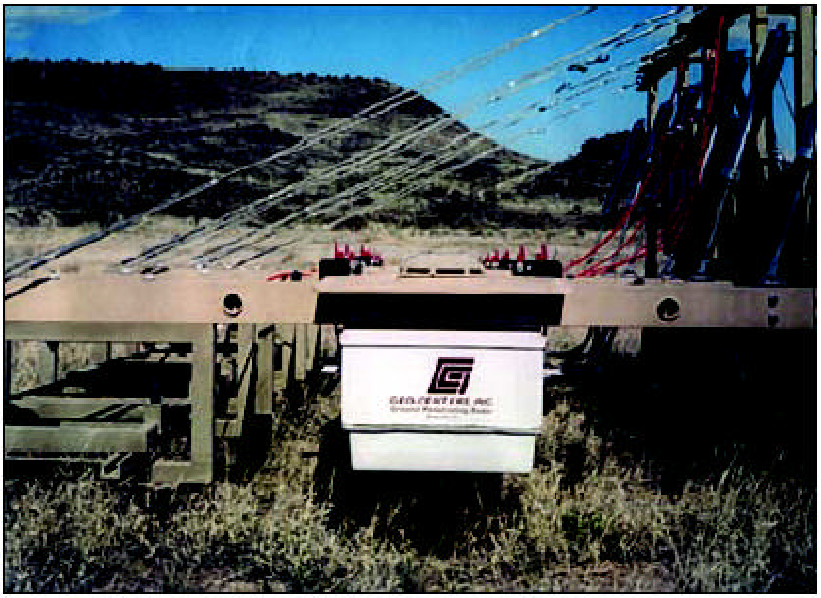

Figure 7. **Energy focusing GPR array (white box) on front-mounted cantilevered platform developed by GEO-CENTERS (from [2]).**

The remainder of this section provides a brief discussion of some of the factors affecting GPR design, some of the tradeoffs that must be made, and their implications on system performance.

1. Frequency, Bandwidth and Range Resolution

The most fundamental choice in GPR is the operating frequency and the bandwidth of the radar. Low frequencies provide the greatest soil penetration. The depth at which targets must be detected and the soil types within which they must be detected drive the choice for the lowest frequencies to be transmitted. For example, UXO detection would generally call for lower frequencies than mine detection because of the greater depths at which targets may be located. Practical limits on low-frequency performance are often determined by the maximum size of the antenna that can be deployed. Range resolution is governed by bandwidth, and an approximate relationship is [2]

$$\Delta R = \frac{c}{2B\sqrt{m_r e_r}} \qquad (2.1)$$

where c is the speed of light, B is the bandwidth, m_r is the ground's relative permeability, and e_r is its relative dielectric constant. Thus, if high resolution in range is desired, wide bandwidth is required, and the higher the center frequency, the narrower the percentage bandwidth for a given resolution. Because of the dispersive properties of soil, high frequencies will be attenuated more than low frequencies. Rather than considering the waveform that is transmitted, the GPR designer must plan his processing and detection strategies around the expected spectrum of the return after propagation to the target, reflection, and propagation back to the radar antenna [10]. Thus, having low frequencies that penetrate well may be of little consequence if the detection algorithm depends on fine resolution and the higher frequencies that provide bandwidth are severely attenuated. The chosen frequency regime also controls less obvious radar characteristics such as achievable cross-range resolution in SAR systems and the level of radio-frequency interference (RFI) with which the system must contend.

2. Wide Bandwidth

Most GPRs for mine detection are wideband devices because good range resolution is required to separate targets from clutter. Two general approaches to obtaining wideband performance are available to the system designer. Each has advantages and disadvantages. The first utilizes waveforms having time-bandwidth product that is near unity [10]. These systems are represented by the family of impulse radars that have been developed for ground-penetration missions. The major advantages of an impulse radar are that lower dynamic range receivers are required to discriminate against clutter, the waveform generation time is short, and a high-range resolution display is available with little or no processing. The major disadvantages are the need to control RF dispersion over a wide instantaneous bandwidth, susceptibility to radio-frequency interference (RFI) because of the wideband receiver front end, the need for very high speed analog-to-digital converters (or the inefficiency of a sampling oscilloscope approach) for waveform capture [10].

The alternative to impulse is to employ a waveform with a time-bandwidth product much greater than one. Such systems have been implemented using stepped

frequency, linear FM chirp, or phase codes [10]. The major advantage of stepped frequency or LFM chirp is that the frequency spectrum can easily be chosen to fit what the designer considers optimum. Stepped-frequency waveforms, in particular, allow narrow instantaneous receiver bandwidth, lower bandwidth analog-to-digital converters, and wider dynamic ranges. This last advantage is often offset by a need for the wider dynamic range because the large surface clutter return and target returns are not temporally separated, as in an impulse system. Other advantages of high time-bandwidth product waveforms are higher average powers, an ability to tailor the frequency response on receive through processing, and the coherent waveform generation required for image processing. Phase and amplitude calibration and equalization are easily accomplished at each discrete frequency step. The major disadvantages are the required dynamic range mentioned above and the time required to generate one complete waveform [10].

A GPR system currently employed by the U.S. Army Corps of Engineers is illustrated in Figure 8. The system being demonstrated employs a combination of traditional UXO detection methods and the new broadband radar technology.

Figure 8. **GPR in service with the U.S. Army Corps of Engineers (from [20]).**

3. Antenna Design Considerations

Subsurface radars pose interesting problems in antenna design. Unlike an atmospheric radar, a subsurface radar must include in its transmission path a lossy, inhomogeneous dielectric, which in some cases may also be anisotropic [11]. The targets may be planar or have some other well-defined shape; they are often of greater extent

than the antenna footprint. This has led to the design of antennas matched both to the characteristics of the medium of propagation and to the geometrical shape of the target. The material propagation characteristics affect the shape of the transmitted spectrum for a required depth resolution and depth of penetration [11]. As a result, antenna design for subsurface radar applications stresses parameters such as impulse response, fractional bandwidth and polarization state. The method of use of the antennas means that cross-coupling levels between closely-spaced transmitter and receiver, interaction of the reactive field of the antenna with the medium of propagation as well as geometry (planar or non-planar) are also important features to take into account [11].

4. Ground Reflections

Reflections are created by an abrupt change in the electrical and magnetic properties of the material the electromagnetic waves are traveling through. In most situations, magnetic effects are small. Most GPR reflections are due to changes in the relative permittivity of material. The greater the change in properties the more signal is reflected. In addition to having a sufficient electromagnetic property contrast, the boundary between the two materials needs to be sharp.

5. Depth of Penetration

The principle limiting factor in depth of penetration of the GPR method is attenuation of the electromagnetic wave in the earth materials. The attenuation predominantly results from the conversion of electromagnetic energy to thermal energy due to high conductivities of the soil, rock, and fluids. Scattering of electromagnetic energy may become a dominant factor in attenuation if a large number of inhomogeneities exist on a scale equal to the wavelength of the radar wave.

GPR depth of penetration can be more than 30 meters in materials having a conductivity of a few mS/m. In certain conditions, such as thick polar ice or salt deposits, the penetration depth can be as great as 5,000 meters. However, penetration is commonly less than 10 meters in most soil and rock. Penetration in mineralogic clays and in materials having conductive pore fluids may be limited to less than 1 meter.

6. Interference and Noise

The GPR method is sensitive to unwanted signals (interference and noise) caused by various geologic and cultural factors. Geologic (natural) sources of noise can be caused by boulders, animal burrows, tree roots, and other inhomogeneties can cause unwanted reflections or scattering. Man-made sources of noise can include reflections from nearby vehicles, buildings, fences, power lines, and trees. Shielded antennas can be used to limit these types of reflections. Electromagnetic transmissions from cellular telephones, two-way radios, television, and radio and microwave transmitters may cause noise on GPR records.

7. Horizontal Resolution

Ideally, a GPR would like to determine a target's location in three dimensions. Assuming a planar flat *x-y* coordinate system on the earth's surface, the radar should provide the target's *x-y* coordinates and its depth. This is illustrated in Figure 9. The *x*, *y* and *z* directions are referred to as the along-track, cross-range, and down-range directions, respectively.

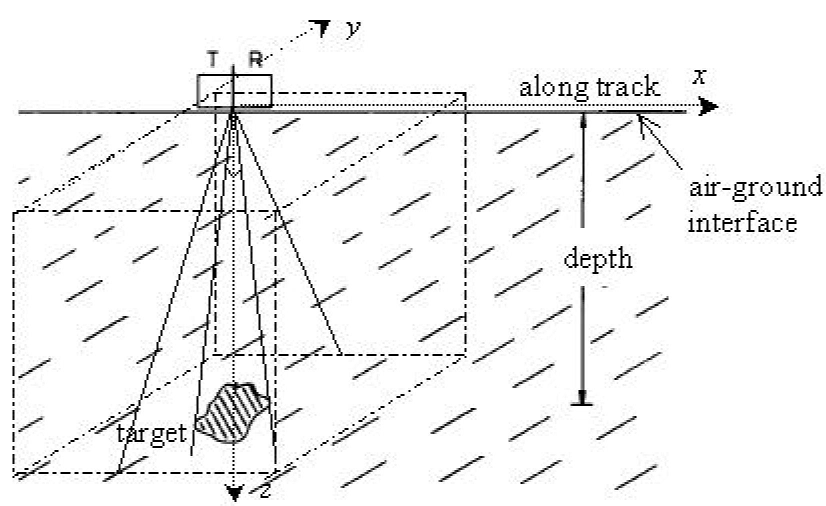

Figure 9. **GPR resolution.**

GPR provides the highest lateral and vertical resolution of any surface geophysical method. The horizontal resolution of the subsurface radar is critical when targets of the same depth need to be distinguished. The technique employed depends on

the wave attenuation of the medium. The locations of the transmitter and receiver, as to whether they are collocated or physically separated, will have to be known.

Figure 10 shows the received power from a target located 2 m below the surface for three ground attenuation values, with the radar moving on the ground (along the *x*-axis). Figure 11 shows the received power from two targets of equal RCS a distance 2 m below the surface positioned at $x = 0$ and 2 m. It can be seen that higher ground loss would actually improve the horizontal resolution [14]. Therefore, increasing the loss per meter of the medium has the same effect as narrowing the antenna beamwidth, resulting in better horizontal resolution.

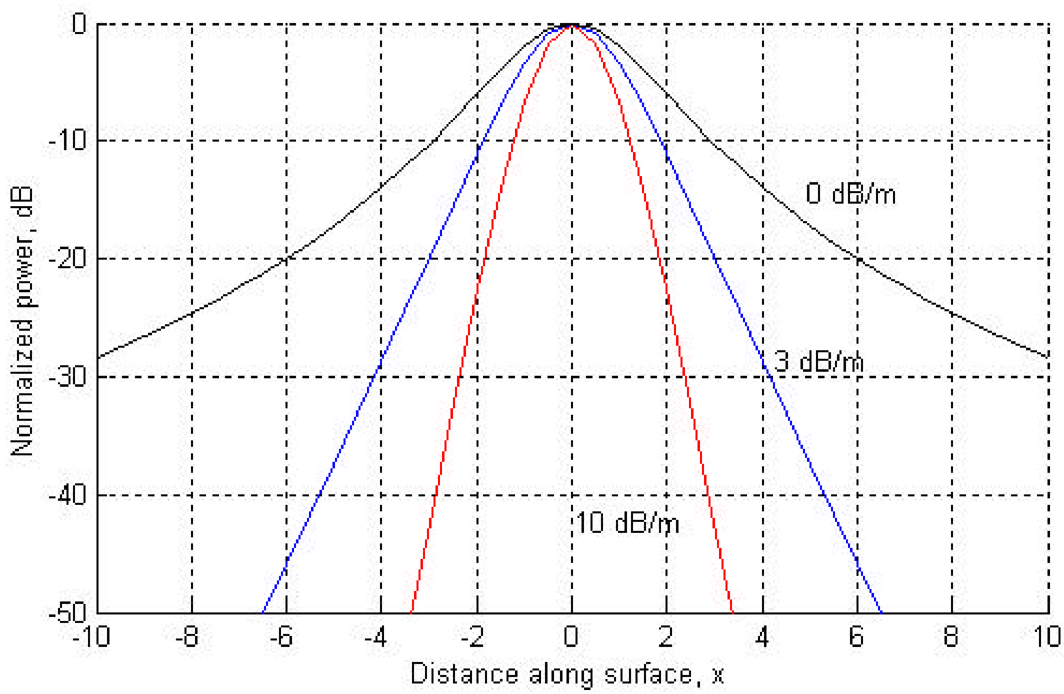

Figure 10. **Received power from a target 2 m below the surface for several ground attenuation values (from [4]).**

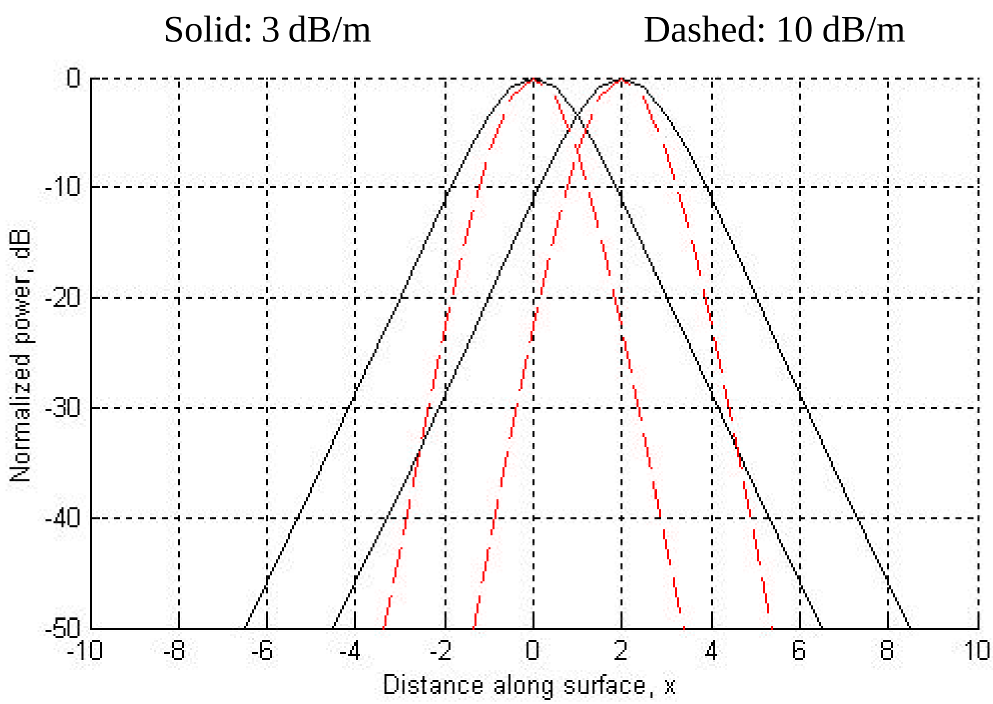

Figure 11. **Received power from 2 targets of equal RCS 2 m below the surface positioned at *x* = 0 and 2 m for two ground loss values (from [4]).**

8. Cross-Range Resolution

Cross-range information can be achieved in several ways. One is to use a narrow antenna beamwidth, which requires an electrically large antenna. This is usually not practical because of the low frequencies required for ground penetration [4], and the small "illumination spot" required for a two-dimensional (2D) image. Another method is to examine the power distribution variation as the antenna moves over the ground. The interpretation of the data depends on ground loss, variations in the scattering cross sections of objects, and the depth and separation of objects. The third is to employ SAR techniques. However, ground loss limits the synthetic aperture length because it has the same effect as narrowing the beamwidth (i.e., cannot keep the scatterer in the antenna field of view). Also, a transversal in two dimensions is required for a 2D image.

D. SUBSYSTEMS OF A GPR SYSTEM

Figure 12 shows the block diagram of a general subsurface radar system. GPR systems are digitally controlled, and data are usually recorded digitally for post-survey

processing and display. The digital control and display part of a GPR system generally consists of a microprocessor, memory, and a mass storage medium to store the field measurements. A small microcomputer and standard operating system is often utilized to control the measurement process, store the data, and serve as a user interface. Data may be filtered in the field to remove noise, or the raw data may be recorded and the data processed for noise removal at a later time. Field filtering for noise removal may consist of electronic filtering and/or digital filtering prior to recording the data on the mass data storage medium. Field filtering should be normally minimized except in those cases where the data are to be interpreted immediately after recording.

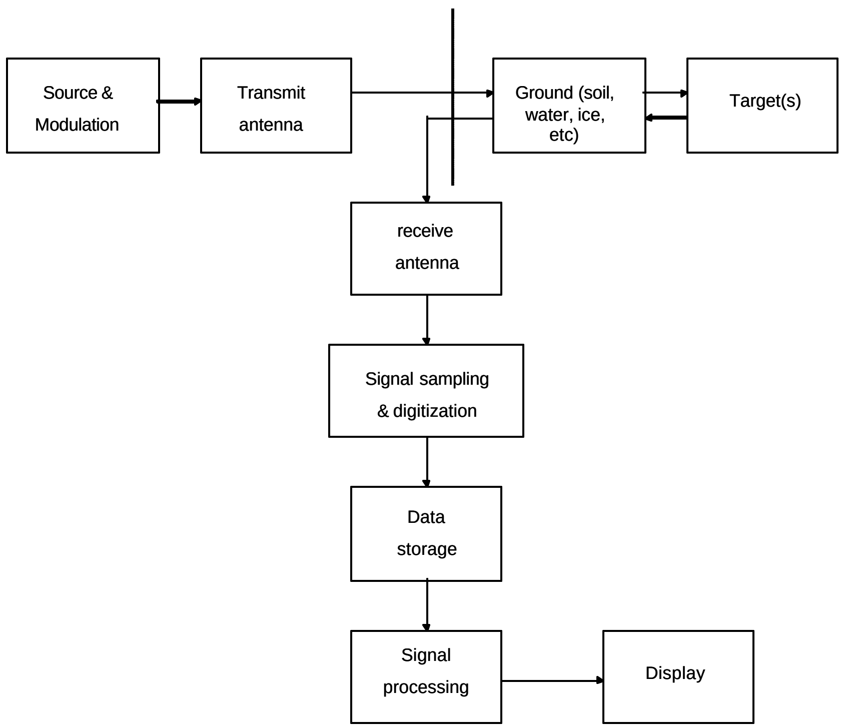

Figure 12. **Block diagram showing the operation of a typical base-band GPR system (from [11]).**

E. SOIL CHARACTERISTICS AND ELECTROMAGNETIC PROPERTIES

Velocity, attenuation, wavelength, polarization, scattering, relaxation and resonance are some of the properties and processes important to electromagnetic wave propagation in ground penetrating radar [16]. Such properties and processes determine

the performance limitations of ground penetrating radar systems. They are also the properties that are measured by ground penetrating radar to describe the ground and things buried within the subsurface. Space and time distributions of material properties are described in terms of complex dielectric permittivity and complex magnetic permeability. Complex is used in the context of phasor quantities, where a $e^{jwt} (w = 2p\ f)$ time dependence assumed.

Dielectric properties are dominantly controlled by the distribution and properties of water in the ground. Magnetic properties are dominantly controlled by the distribution and properties of iron in the ground [16]. Field polarization and scattering processes are dominantly controlled by geometric orientation and spatial distribution of contrasts in material properties at wavelength scales. Measurement of field properties and processes allows GPR to determine the corresponding material properties [16].

Dielectric properties of earth materials have been covered quite extensively in many references [14-15,19,21-24]. It has been understood that for GPR to be effective, the RF electrical properties of the mines must differ from the host soil material. In the GPR case, the physical quantities that affect electromagnetic wave propagation are permittivity and conductivity (the permeability is assumed constant and equal to that of free space, m_o). Electromagnetic waves travel at a specific velocity that is determined primarily by the electrical permittivity of the material. The velocity is different between materials with different electrical properties, and a signal passed through two materials with different permittivities over the same distance will arrive at different times. The interval of time that it takes for the wave to travel from the transmit antenna to the receive antenna is simply called the transmit time.

All systems measure the time a signal needs to travel from the surface to an interface and back again. The radar waves obey Maxwell’s Laws, which allows approximating the velocity in the ground [18] as

$$v = \frac{c}{\sqrt{e_r}} \text{(m/ns)} \tag{2.2}$$

with c = 0.3 m/ns is the speed of light and e_r as the relative dielectric constant. Since the velocity of an electromagnetic wave in air is 0.3 m/ns, the travel time for an electromagnetic wave in air is approximately 3.33 ns per meter traveled, and since the permittivity of earth materials is always greater than the permittivity of the air, the travel time of a wave in a material other than air is always greater than 3.33 ns/m. Table 2 illustrates some examples of permittivities and velocities for various earth materials. The dielectric constant principally depends on the water content.

The relative dielectric constant, which is the most important physical parameter of the soil, may vary with depth and therefore the velocity of the waves in the ground is not constant. This physical parameter not only determines the velocity of the wave in the ground but also the reflection strength between two different materials. The amplitude of the signals decays strongly. The spherical spreading describes the reduction proportional to the inverse of the distance. Additionally the signal is strongly attenuated by absorption and scattering in the ground. This is mainly an effect of the conductivity of the ground. Knowing the relative dielectric constant e_r and the conductivity s , the attenuation a due to travel over a distance x can be estimated from [18]

$$\text{Loss} = 20\log_{10}(e^{-ax})\ \text{dB} \tag{2.3}$$

where, for a dielectric

$$a = w\sqrt{\frac{m_o e}{2}}\left[\sqrt{1+\left(\frac{s}{we}\right)^2}-1\right]^{1/2}\ \text{Np/m} \tag{2.4}$$

Equation (2.4) shows that the higher the frequency, the more the signal is attenuated [18]. Table 2 shows that clay and high water content will limit the radar operating depth at a frequency of 1.25 GHz.

Material	e_r	***v* (m/ns)**	s **(mS/m)**	a **(Np/m)**
Air	1	0.3	0	-
Salt water	80	0.034	3000	4.13
Fresh water	80	0.034	0.5	1.18
Granite, dry	5	0.134	0.01	» 0
Sand, dry	5	0.134	0.01	» 0
Clay, wet	10	0.095	500	3.68
Sandy soil, dry	2.6	0.186	1.4	2.18
Sandy soil, wet	25	0.060	69	3.18
Clay soil, dry	2.5	0.190	2.7	2.36
Clay soil, wet	19	0.069	500	3.68
Frozen soil	6	0.122	0.1	1.02
Lacustrine chalk	50	0.042	-	-

Table 2. **Medium values of different materials for the relative dielectric constant e_r, the velocity *v*, the conductivity s and the attenuation a at a frequency of 1.25 GHz (after [18]).**

The center frequency of the antenna must not be confused with the frequency of the returning signal. Because of the above-mentioned stronger reduction of higher frequencies, the spectrum is always shifted towards a lower frequency and at the same time the bandwidth is reduced [18]. Figure 13 shows the spectral spread of a stepped-frequency waveform (12 pulses, frequency step size 50 MHz per pulse, start frequency 500 MHz, PRF of 10 MHz, and pulse width of 0.01 microsecond) being transmitted and received from a target buried underground.

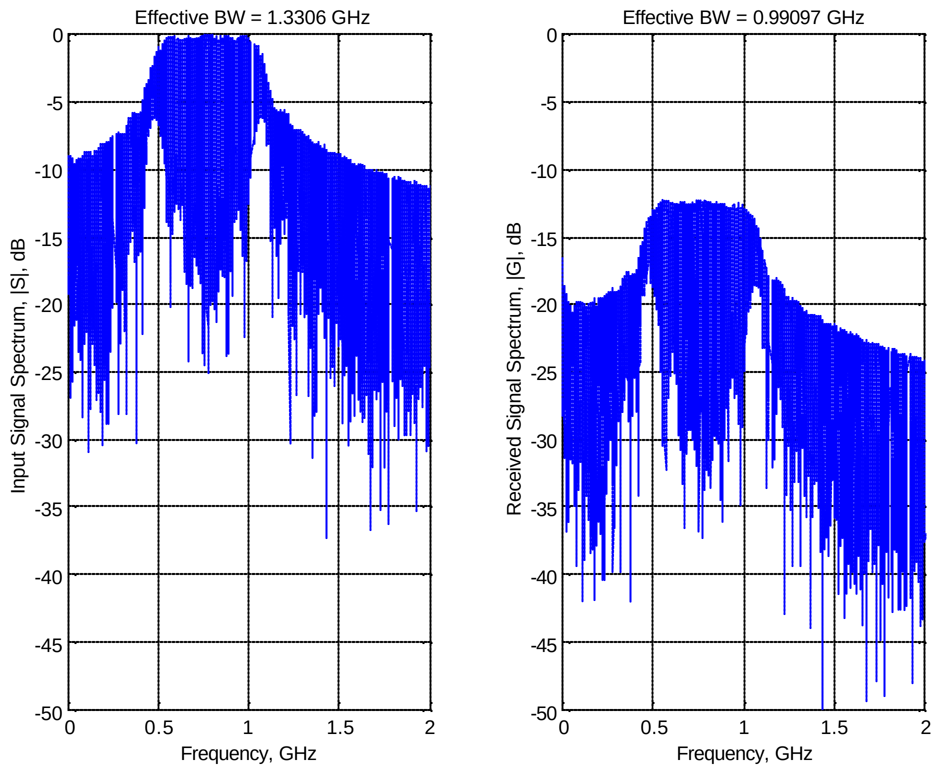

Figure 13. **Frequency spread of a stepped frequency waveform transmitted and received from the ground (from [4]).**

It has been observed experimentally that for most materials that make up the earth near its surface, the attenuation of the electromagnetic radiation increases with frequency [14]. In general, wet materials exhibit higher loss than dry ones at a given frequency. Figure 14 shows the one-way path loss for different material surfaces over a frequency range from 1 MHz to 1 GHz. It is shown here that the attenuation of wet rock is higher than dry rock, and salt water has the highest level of attenuation.

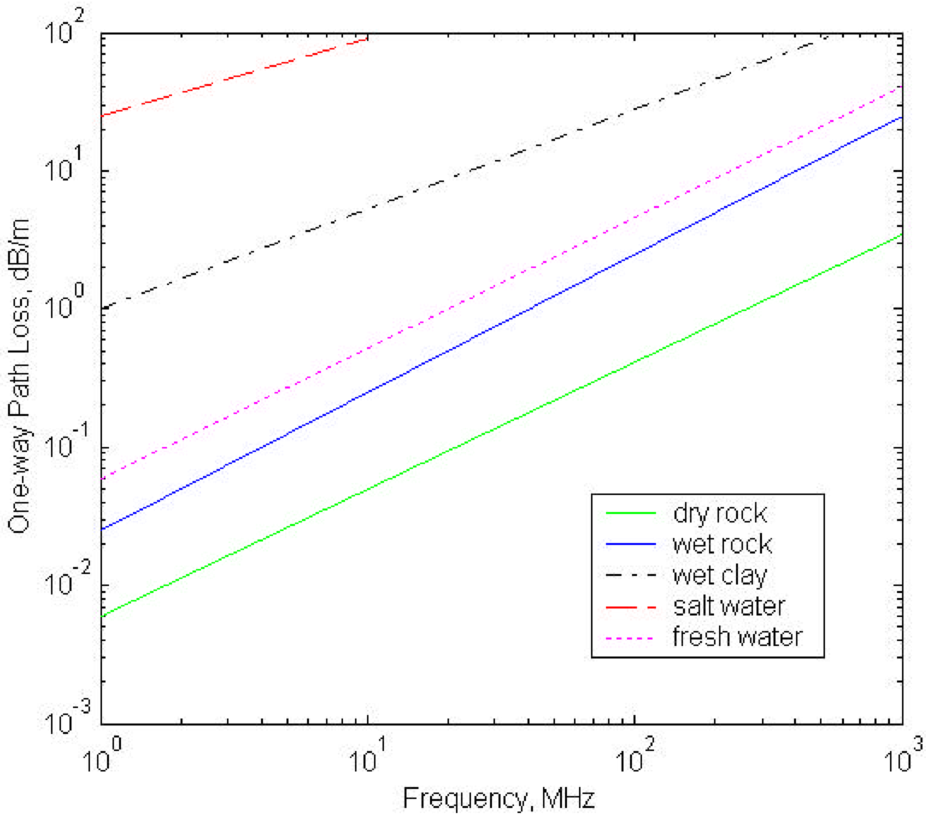

Figure 14. **One-way path loss for various ground materials from 1 MHz to 1GHz (from [4]).**

F. SUMMARY

This chapter has examined the underlying principles of GPR applications by introducing the critical factors affecting GPR design, the tradeoffs that must be made, and their implications. The distinction between detecting a landmine and UXO and the means of detecting them was studied.

The operational effectiveness of a GPR depends not only on the frequency of operation but is largely limited by the texture of soil, soil water content, electrical properties of soil and soil density. It was also observed that attenuation of the EM radiation increased with frequency for most types of materials.

The classes of antenna that can be used for significant ground penetration and resolution generally require wide bandwidth and low operating frequency. The helical antenna has been known to fulfill these needs, and will be investigated in the next chapter.

THIS PAGE INTENTIONALLY LEFT BLANK

III. THE HELICAL ANTENNA

A. THE MONOFILAR HELIX

The helix or helical antenna has been widely used as a circularly polarized radiator over a wide frequency range. Its basic characteristics have been given by Kraus [25]. His investigation covered antennas between three and ten turns and pitch angles of $5°$ to $24°$. Sufficient analysis was carried out to give an adequate understanding of the operation of the antenna in terms of inward- and outward-traveling waves along the conductor. An alternative and more complete theoretical approach to the problem of electromagnetic wave propagation along helical conductors was given by Senisper [26] in 1951, but his interest was primarily in application to traveling-wave tubes.

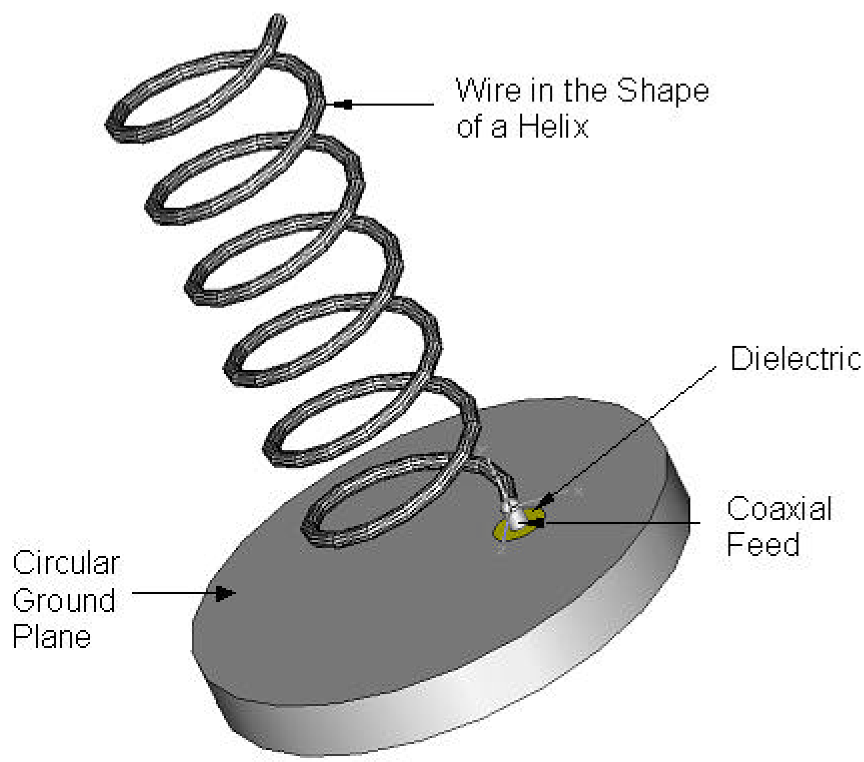

Figure 15. **Monofilar helix antenna with a ground plane and coaxial feed.**

The helix essentially consists of a single wire (monofilar case) or narrow tape wound like a left-hand or right-hand screw, self-supporting or wound on a dielectric cylinder, as shown in Figure 15. The helix has a simple 3-dimensional geometry. A

helical wire on a uniform cylinder becomes a straight wire when unwound by rolling the cylinder on a flat surface. Viewed end-on, a helix projects a circle. Thus, a helix combines the geometric forms of a straight line, a circle and a cylinder. In most cases the helix is used with a ground plane. The ground plane can take different forms. Most commonly the ground is circular, as shown in Figure 15.

Typically the diameter of the ground plane should be at least $3l/4$ [27], with l the operating wavelength. However, the ground plane can also be cupped in the form of a cylindrical cavity or in the form of a frustrum cavity [27]. Typically the helix is excited by a coaxial line over a small ground plane with diameter G and the other end of the wire is left as an open circuit. This is done by connecting the helix to the center conductor of a coaxial transmission line at the feed point with the outer conductor of the line attached to the ground plane.

For this thesis, the helix is oriented along the y-axis, perpendicular to a perfect ground lying in the x-z plane. The parameters and geometry used to describe the helical structure are described in Table 3 and defined in Figure 16.

Parameter	**Symbol**
Diameter of helix	$D = 2r$
Number of turns	N
Spacing between each turn	S
Axial Length	L
Pitch angle	a
Length of 1 turn	L_o
Tangential unit vector	$\hat{l}$
Radius of helix wire	A
Starting height	y_0

Table 3. **Design parameters for a helix antenna.**

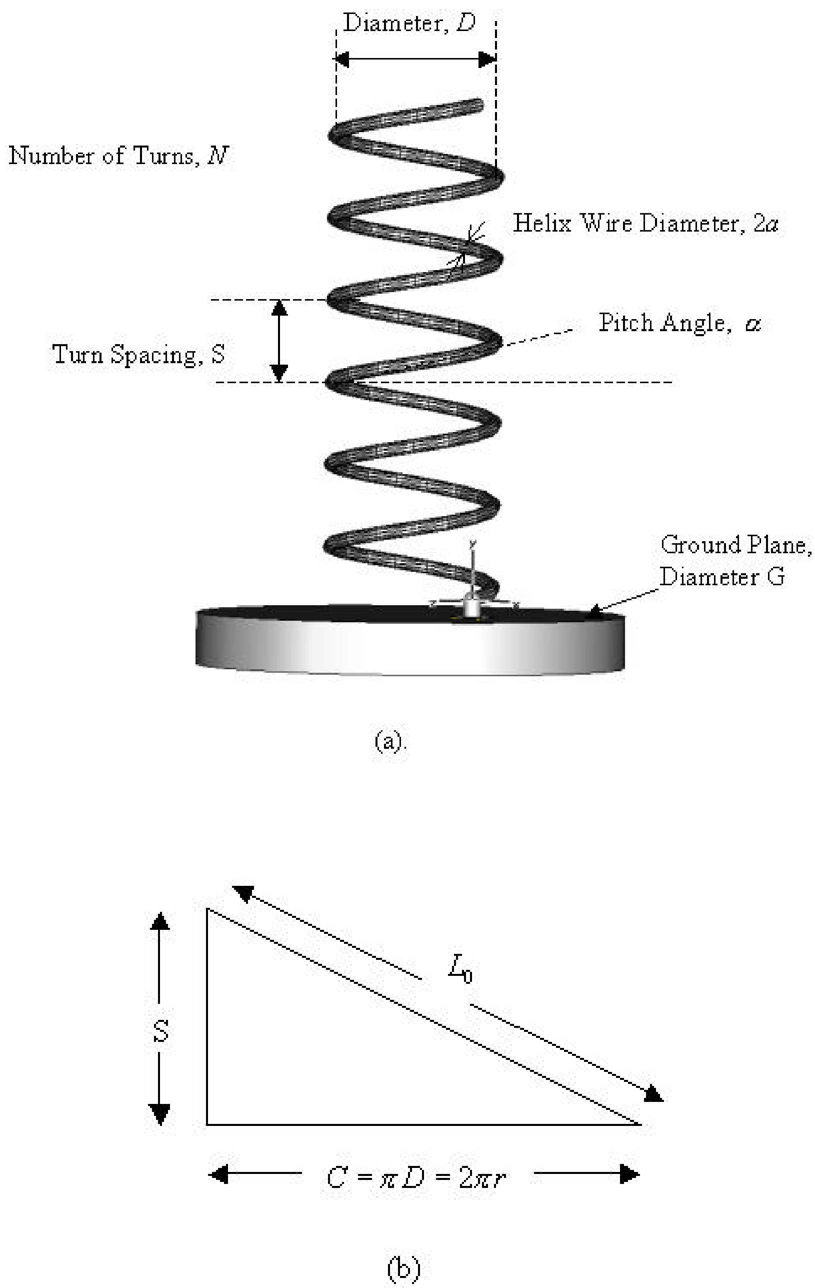

Figure 16. **Definition of helix parameters. (a) Helical antenna with a ground plane. (b) Single turn unfolded.**

The tangential unit vector, $\hat{l}$, describes the contour of the helix, while a is the radius of the wire used to wind the helix. Figure 16 (b) shows a schematic of one turn of the helix if it were unwound. The total axial length of the antenna is [27]

$$L = NS \quad \text{meters} \tag{3.1}$$

while the total length of the wire is

$$L_n = NL_o = N\sqrt{S^2 + C^2} \quad \text{meters} \tag{3.2}$$

where

$$L_o = \sqrt{S^2 + C^2} \quad \text{meters} \tag{3.3}$$

is the length of the wire between each turn and

$$C = \pi D \quad \text{meters} \tag{3.4}$$

is the circumference of the helix.

Another important parameter is the pitch angle, α, which is the angle formed by a line tangent to the helix wire and a plane perpendicular to the helix axis. The pitch angle is defined by [27]

$$\alpha = \tan^{-1}\left(\frac{S}{\pi D}\right) = \tan^{-1}\left(\frac{S}{C}\right) \quad \text{degrees} \tag{3.5}$$

When $\alpha = 0°$, the winding is flattened and the helix reduces to a loop antenna of N turns. On the other hand, when $\alpha = 90°$ then the helix reduces to a linear wire. For $0° < \alpha < 90°$, a true helix is formed with a circumference greater than zero but less than the circumference when the helix is reduced to a loop at $\alpha = 0°$.

By varying the values of the parameters, the electrical performance of the antenna can be controlled. The input impedance is critically dependent upon the pitch angle and the size of the conducting wire [27], especially near the feed point. The general polarization of the antenna is elliptical. However circular and linear polarizations can be achieved over different frequency ranges.

The wire's helical contour can be described by the vector [28],

$$\vec{r} = \hat{x}x + \hat{y}(y + y_0) + \hat{z}z \tag{3.6}$$

which points from the origin to any point (x,y,z) on the helix. The x and z coordinates are given by

$$x = r\cos\left\{\frac{2p}{L_0}(y - y_0)\right\} \tag{3.7}$$

and

$$z = r\sin\left\{\frac{2p}{L_0}(y - y_0)\right\} \tag{3.8}$$

The spacing between turns can be written as $S = L_0 \sin a$, and the y coordinate is given by $y = l\sin a$, where l is the distance along the helix in the $\hat{l}$ direction. Combining the above relationships with (3.6) gives [28]

$$\vec{r} = \hat{x}r\cos\left(\frac{2p}{L_0}l\right) + \hat{y}(l\sin a + y_0) + \hat{z}r\sin\left(\frac{2p}{L_0}l\right) \tag{3.9}$$

which describes any point on the helix.

The helical antenna can operate in several different modes. However, the two principal modes of interests are [27]:

a). the normal (broadside) mode - where the maximum field that is radiated by the antenna is in the plane that is normal to the helix axis, the minimum is along the axis;

b). the axial (endfire) mode – where there is only one major lobe of the pattern and it is in the direction of the axis of the helix

The major differences between a normal mode helix and an axial mode helix is the radius of the helix with respect to wavelength and the presence of the ground plane [27]. The radius of a normal mode helix is much smaller than a wavelength, which results in a radiation pattern normal to the axis of the helix. The axial mode helix has a radius corresponding to a circumference for one turn of approximately 3/4 $< C / l <$ 4/3 [27], which gives rise to radiation pattern maxima along the axis of the helix. The axial mode helix is usually backed by a ground plane to cut off one of the lobes of the pattern to create a unidirectional beam forward radiation pattern.

The axial (endfire) mode is usually the most practical because it can achieve circular polarization over a wider bandwidth and it is more efficient. Because an elliptically polarized antenna can be represented as the sum of two orthogonal linear components in time-phase quadrature, a helix can always receive a signal transmitted from a rotating linearly polarized antenna. Therefore helices are usually positioned on the ground for space telemetry applications of satellites, space probes, and ballistic missiles to transmit or receive signals that have undergone Faraday rotation by traveling through the ionosphere [27]. Only the axial mode is of interest for GPR applications.

A helical antenna can radiate in the axial mode, if the wavelength of the operating frequency is approximately equal to the circumference of the helix [30]. In this mode of operation, there is only one major lobe and its maximum radiation intensity is along the axis of the helix, as shown in Figure 17. The minor lobes are at oblique angles to the axis. To excite this mode, the diameter D and spacing S must be large fractions of the wavelength [27]. The axial mode exists in a limited frequency range when the circumference of the helix is between $3/4 < C/l < 4/3$ and the spacing about $S \approx l/4$ [31]. Properly designed, the antenna will have circular polarization, primarily in the major lobe (with $C/l = 1$ near optimum). The pitch angle is usually $12° < a < 14°$ [27]. Most often the antenna is used in conjunction with a ground plane, whose diameter is at least $3l/4$, and it is fed by a coaxial line. However other types of feeds (such as waveguides and dielectric rods) are possible, especially at microwave frequencies. The dimensions of the helix for this mode of operation are not as critical, thus resulting in a greater bandwidth.

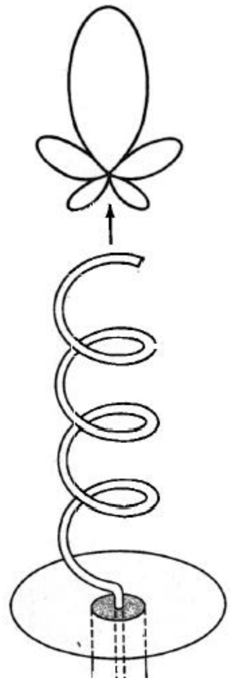

Figure 17. **Helix in axial (endfire) mode of operation1GHz (from [27]).**

1. Design Procedure for Axial Mode Operation

The terminal impedance is generally dependent on the pitch angle and the size of the conducting wire near the feed point [27]. For an axial mode radiating helix, the input impedance is nearly resistive with values between 100 and 200 ohms. Smaller values, even near 50 ohms, can be obtained by properly designing the feed. Empirical expressions based on a large number of measurements have been derived [27], and they are used to determine a number of parameters. The input impedance (purely resistive) is obtained by

$$R \simeq 140\left(\frac{C}{l}\right) \text{ ohms} \qquad (3.10)$$

which is accurate to about $\pm 20\%$.

Most antennas need to be matched to a $50\,\Omega$ transmission line, which can be achieved in one of the following ways:

a). by using a quarter-wave matching transformer between the feed line and the feed point of the helix, or

b). increase the conductor size between the end of the helix and the feed point.

The second method is the cheaper option and the most commonly used one.

Other output parameters of the antenna can be obtained from the following formulas [27]:

(1) half-power beamwidth:

$$\text{HPBW} \simeq \frac{52\, l^{3/2}}{C\sqrt{NS}} \quad \text{degrees} \tag{3.11}$$

(2) beamwidth between nulls:

$$\text{FNBW} \simeq \frac{115\, l^{3/2}}{C\sqrt{NS}} \quad \text{degrees} \tag{3.12}$$

(3) directivity:

$$D_o(\text{dimensionless}) \simeq 15N \frac{C^2 S}{l^3} \tag{3.13}$$

(4) axial ratio (polarization) for the condition of increased directivity:

$$\text{AR} \approx \frac{2N+1}{2N} \tag{3.14}$$

(5) normalized far-field pattern:

$$E = \sin\left(\frac{p}{2N}\right)\cos q \,\frac{\sin[(N/2)y\,]}{\sin[y\,/2]} \tag{3.15}$$

where

$$y\ = k_o\left(S\cos q - \frac{L}{p}\right) \tag{3.16}$$

For ordinary endfire radiation

$$p = \frac{L/l_o}{S/l_o + 1} \tag{3.17}$$

For Hansen –Woodyard endfire radiation

$$p = \frac{L/l_o}{S\Big/ l_o + \left(\frac{2N+1}{2N}\right)} \tag{3.18}$$

All these relations are approximately valid provided $12° < a < 14°$, $3/4 < C/l < 4/3$ and $N > 3$ [27].

The far-field pattern of the helix, as given by Equation (3.15), has been developed by assuming that the helix consists of an array of N identical turns (each of non-uniform current and identical to that of the others), a uniform spacing S between them, and the elements are place along the z-axis. The $\cos q$ term in Equation (3.15) represents the field pattern of a single turn, and the last term in Equation (3.15) is the array factor of a uniform array of N elements. The total field is obtained by multiplying the field from one turn with the array factor (pattern multiplication). Elaboration of the field theory can be found in [27].

B. MULTIFILAR HELIX

The quadrifilar helix antenna (QHA) was invented by Gerst [31,32]. Gerst and Worden also reported some of the characteristics of the broader class of multifilar helix antennas. The characteristics can be varied by controlling the size of the geometrical parameters relative to the wavelength. With regard to the far-field, improved performance can be achieved by adding more helix arms as shown in Figures 18 and 19, and feeding them with the appropriate phase relationships.

Bifilar and quadrifilar helix antennas consist of two and four arms respectively. One of the attractive features of helix is its wide bandwidth. A simple helix can be made

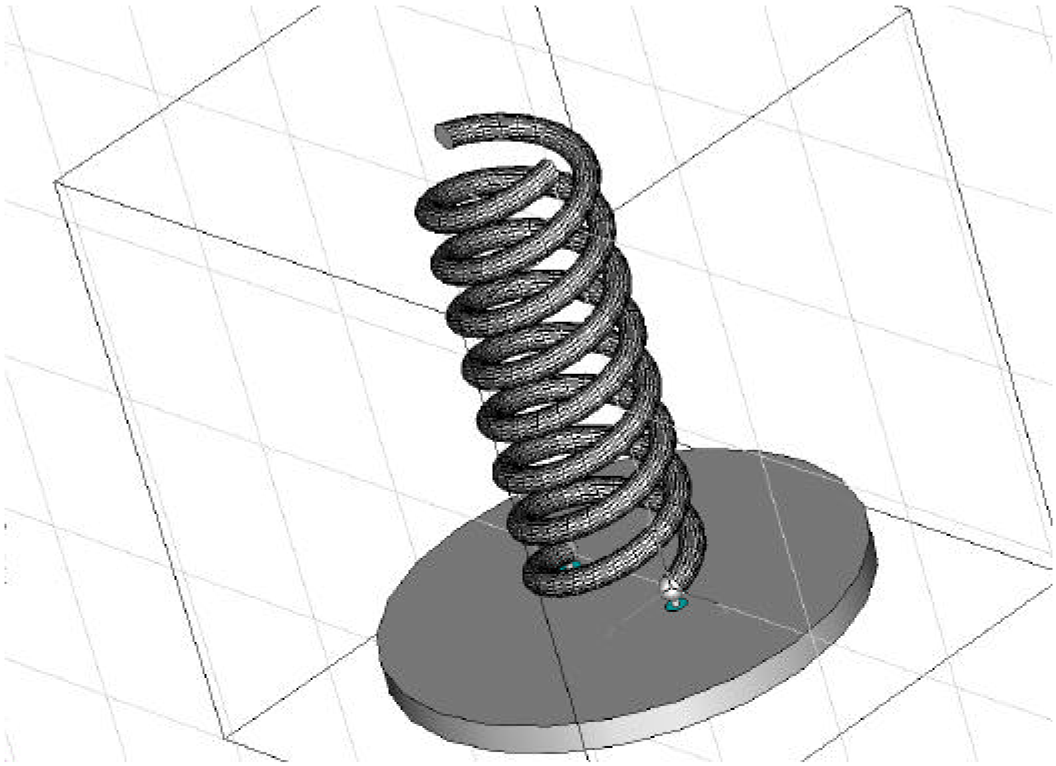

Figure 18. **Bifilar helix antenna with a ground plane and coaxial feed.**

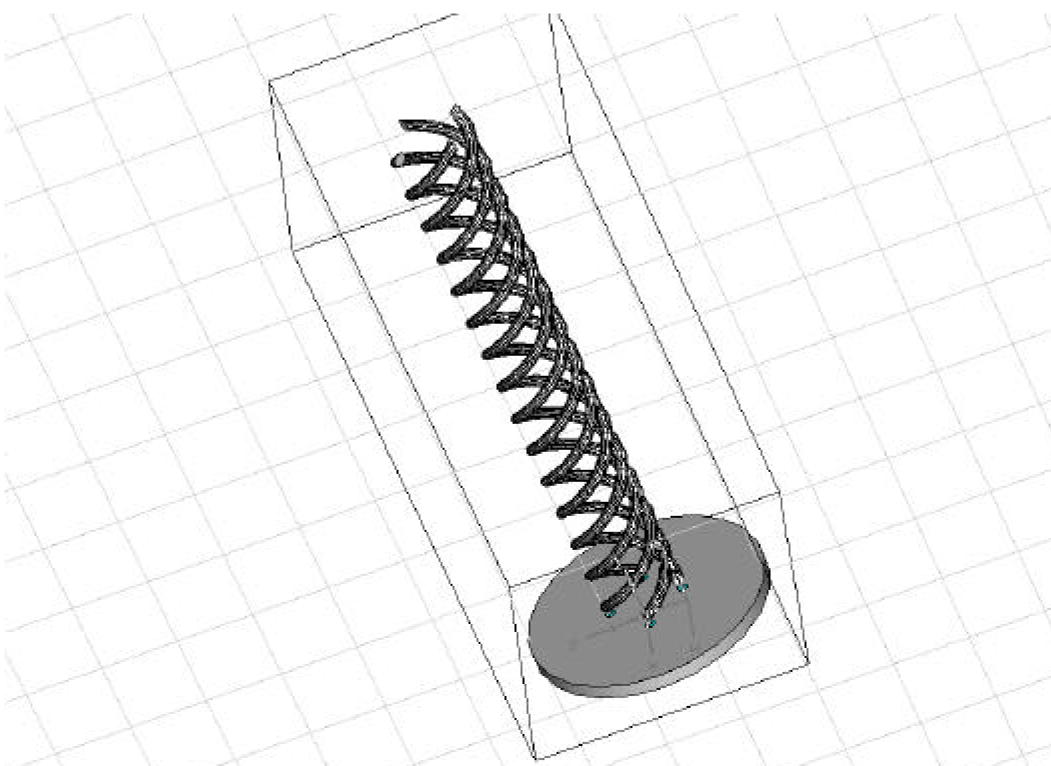

Figure 19. **QHA with a ground plane and coaxial feed.**

to operate several octaves and bandwidths of 5:1 have been reported for the quadrifilar helix [33]. Adding more arms also reduces the radiation in the back direction [34].

The polarization can also range from linear to circular as the frequency is changed. Linear polarization can be assured by adding a second set of windings that are wound in a sense opposite that of the first set (a counter-wound helix antenna) as shown in Figures 20 to 22. Previous studies on optimizing the performance of the helix have concerned its far-field behavior [33]. In the application of ground penetrating radars, the near-field performance is of interest.

This research examines the suitability of using counter-wound helix antennas for field operations. The antenna was simulated in Microwave Studio and the near-field patterns were calculated as a function of distance from the helix. Several design parameters were varied to determine their effects on the near-field behavior. The fields of monofilar, bifilar and quadrifilar helices, both counter-wound and non-counter-wound, were examined.

The multiwire helix consists of a number of single-wire helices equally spaced circumferentially. For N wires, there are N feed points, and N-1 different, independent modes. It is customary to choose the model such that they have a progressive phase variation circumferentially [29]. Arm k will thus have an excitation of

$$\Phi_{km} = \exp\left(-2p\ j\frac{km}{N}\right) \tag{3.19}$$

for mode m. As with usual discrete Fourier transforms any excitation may be expressed as a linear combination of these orthogonal excitations.

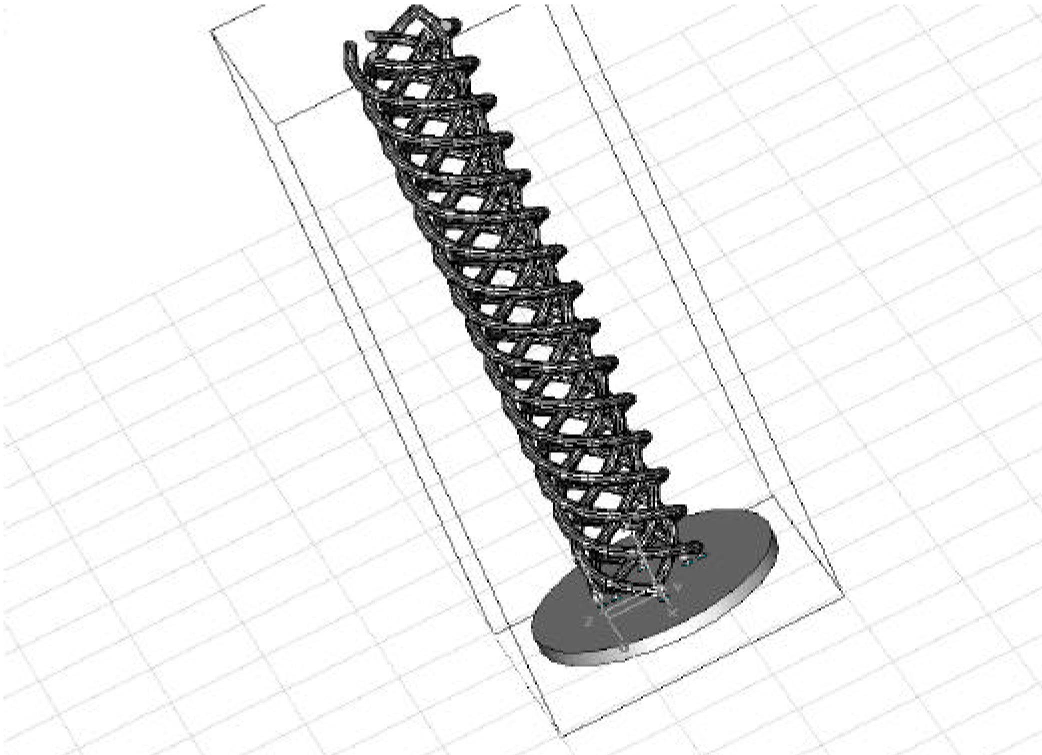

Figure 20. **CQHA with a ground plane and coaxial feed.**

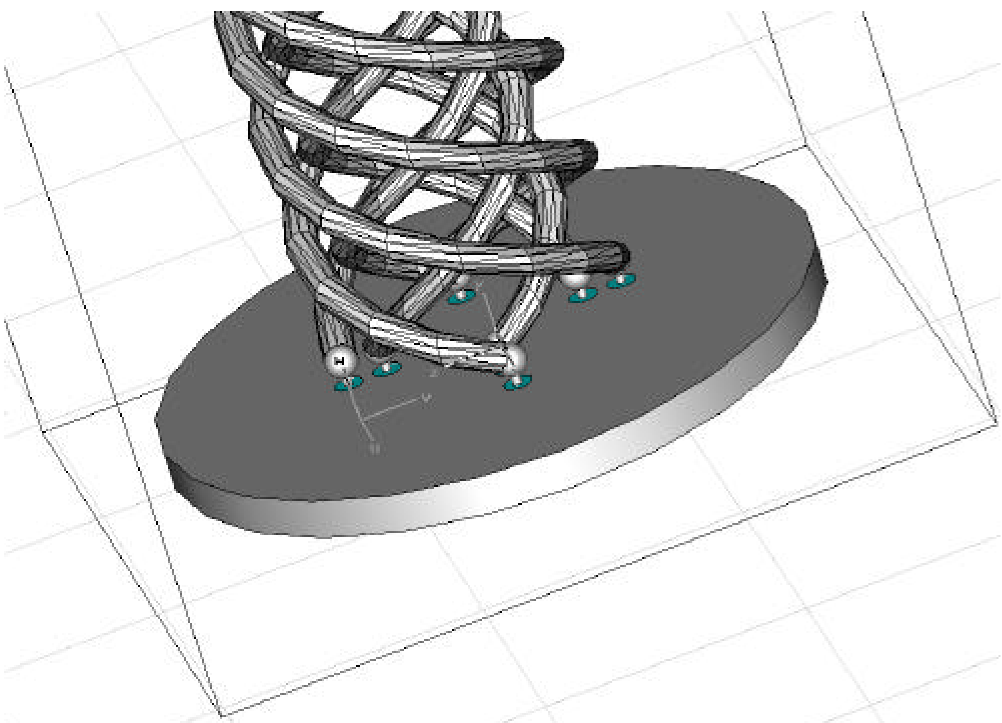

Figure 21. **Close-up view of the CQHA and its coaxial feed system.**

The Quadrifilar Helical Antenna was invented by Kilgus in 1968 [35,36]. Resonant quadrifilar helix antennas are widely used on hand-held receivers for GPS and for some mobile communication systems. The significant advantages of this type of antenna include its relatively compact size and its cardioid-shaped pattern with excellent circular polarization coverage and high axial ratio over most of the field of view [34]. Since it is a resonant antenna, its dimensions are chosen to provide optimal performance for one frequency band. Several techniques have been described in publications that would extend this antenna's capability to two frequency bands (L1 and L2 for GPS applications [37]).

Each of the four arms of the quadrifilar helix has the same number of turns. Each filament is open at one end and has a feed point at the other end. The length is chosen for resonant operation at the lower end of the frequency band. The four arms of the helix are excited with sequential phase variation, 0°, 90°, 180°, 270° [38] to obtain circular polarization. The height of a quadrifilar helix antenna is directly related to its impedance [39]. The peak of the radiation pattern for this antenna can be designed for either the forward axial direction (toward the open end of the arms) or the backfire axial direction. The former requires the placing of a small circular ground plane perpendicular to the axis at the feed points. The latter has no ground plane [34]. The initial experimental demonstration of this antenna was done for the forward direction along the axis. Since the helix inherently a backfire antenna, the ground plane serves as a reflector to redirect the energy. Because reflection of a circularly polarized electromagnetic signal from a planar conductor changes its sense of polarization, radiation of a right-hand circularly polarized signal requires the helix to have a left-hand twist. As with the conventional helix, linear polarization can be obtained by adding four arms wound in a sense opposite to the first set, a counter-wound quadrifilar helix antenna (CQHA). An example of a CQHA over a ground plane is shown in Figure 22.

It is known that a QHA produces a cardiod-shaped radiation pattern with excellent circular polarization [35,36]. The radiation patterns are controlled mainly by the pitch angle and length of helix elements. The polarization of the quadrifilar helix antenna depends only on helical winding direction [40]. The feed network is the most complicated aspect in the design of the QHA.

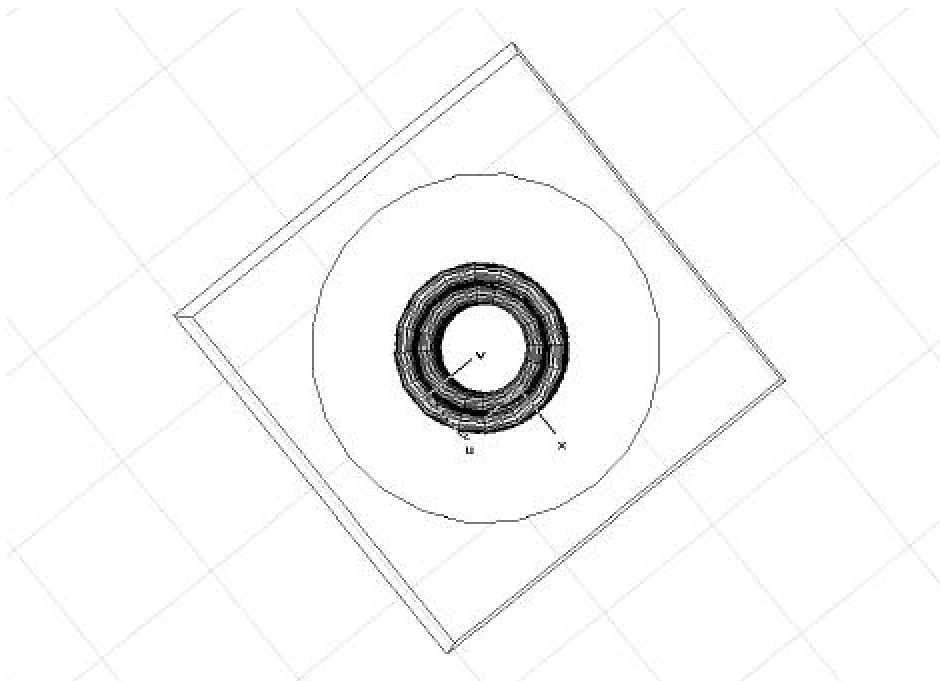

Figure 22. **Plan view of the CQHA – similar to having 2 concentric circles.**

C. OPTIMIZATION OF THE QUADRIFIALR HELIX ANTENNA

Experimental data on the quadrifilar helix antenna have led to an optimum pitch angle and an optimum ground plane size [33]. The ground plane size is an important parameter, and its optimum diameter is about three times the diameter of the helix. The optimum pitch angle is about $35°$. The behavior of the quadrifilar helix is a complex function of several parameters. In particular, pitch angle, ground plane diameter, and antenna length are all important parameters [33]. Less important is the tape width (wire diameter), which may be termed a second-order parameter. Details of the experimental study can be found in [33].

The principal results of the study presented in [33] are as follows. The ground plane size, which is not usually considered to be an important parameter for the monofilar helix, is an important parameter for the quadrifilar helix. There are two important frequency ranges in the operating band falling at approximately two and three times the

frequency at which backfire first occurs (just below the operating band for the axial mode). In these frequency ranges, there is a strong tendency towards pattern breakup. The pattern breakup can be avoided if both ground plane size and pitch angle are adjusted to "optimum" values. For this thesis, these optimum values were used in all the simulations.

Over the last few years, the characteristics of the circularly polarized QHA and the linearly polarized CQHA have been studied experimentally in some detail [33,38]. For the counter-wound quadrifilar, the feeding system induces opposite phase differences between the wires [33]. The CQHA consists of two sets of counter-wound helices, each with four filaments, one wound directly over the other. Figure 23 shows a schematic representation of the feed system for the CQHA. The feed system is divided into two identical sections, one for the left and one for the right hand helix. The feed system for the QHA consists of just one section.

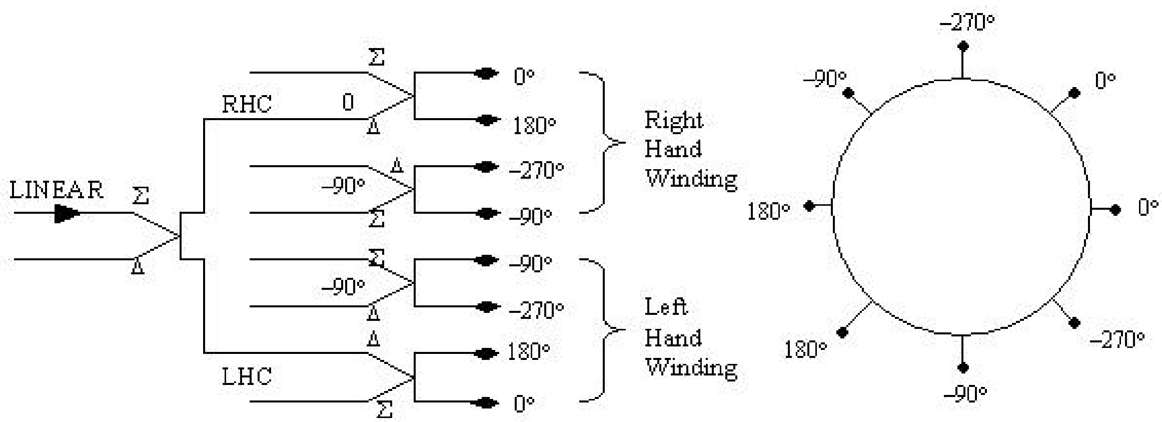

Figure 23. **Feed system of CQHA (after [33]).**

The operation of the QHA is similar in some respects to the monofilar helix antenna [31], which radiates in the normal or "radial" mode for C/l less than 0.75 and radiates in the axial or forward endfire mode for C/l between approximately 0.75 and 1.25. Experimental data shows that the QHA operates in the axial mode for C/l between approximately 0.4 and 2.0 [33]. Therefore, the bandwidth of the QHA operating in the axial mode spans that of the monofilar helix antenna. The principal disadvantage is the

increase in complexity of the feed system. Figure 24 summarizes the radiation patterns from the normal and axial mode for the quadrifilar helix.

The QHA offers two advantages over the monofilar helix:

a). an increase in bandwidth and

b). a lowered frequency for axial mode operation.

Additionally, when a set of counter windings is added to obtain a CQHA, dual linear polarization is possible.

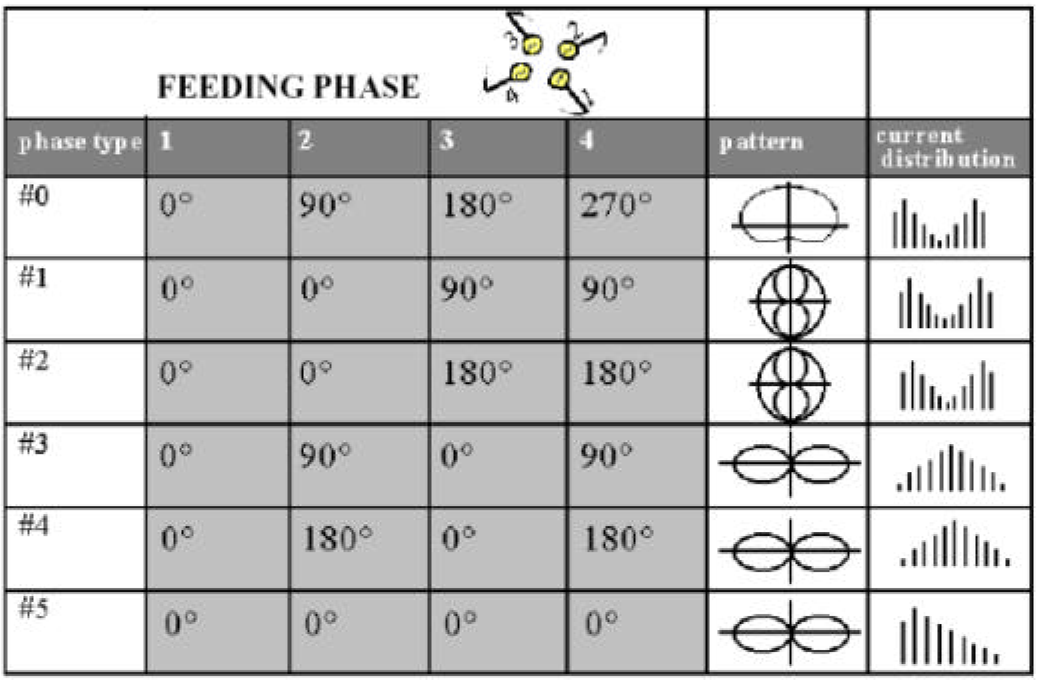

FEEDING PHASE						
phase type	1	2	3	4	pattern	current distribution
#0	0°	90°	180°	270°		
#1	0°	0°	90°	90°		
#2	0°	0°	180°	180°		
#3	0°	90°	0°	90°		
#4	0°	180°	0°	180°		
#5	0°	0°	0°	0°		

Figure 24. **Radiation pattern (elevation cuts) and current distribution (on helical elements) of a QHA in different phase combinations (from [44]).**

D. SUMMARY

This chapter has examined the helical antenna for GPR applications. The parameters describing the helix were defined, their range of values for both the normal and axial modes were specified. The axial mode helix demonstrated the desirable characteristics necessary for an antenna for subsurface radar applications. The

characteristics can be varied by controlling the size of the parameter values relative to the wavelength.

By adding more arms, as in the case of a bifilar or quadrifilar helix, wider bandwidth and a reduction of radiation in the back direction can be achieved. Linear polarization can be achieved by adding a second set of arms that are wound in an opposite sense to those of the first set, i.e., a counter-wound helix.

The radiation field patterns and the input reflection of the monofilar, bifilar and quadrifilar, both regular and counter-wound, are some of the parameters that will be investigated in the next chapter.

THIS PAGE INTENTIONALLY LEFT BLANK

IV. SIMULATION RESULTS AND ANALYSIS

This chapter presents the performance of the monofilar, bifilar and quadrifilar helices, for both regular and counter-wound antenna types. The results are obtained through simulation by means of modeling the helix structure in Microwave Studio. The computational electromagnetic (CEM) simulation program, Microwave Studio (developed by CST), was used to analyze the performance of the helical antenna in terms of its radiation field patterns, input impedance, bandwidth and the scattering parameter (S_{11}), which is related to the input reflection coefficient. The simulated results of the antenna were compared to theoretical results. While the helix has two modes of operations, only the desired axial mode has been analyzed. The axial mode has only one major lobe and it is in the direction of the axis of the helix.

A. MONOFILAR HELIX

Figure 15 shows the configuration structure for the uniform monofilar helical antenna with a ground plane and a coaxial feed as modeled using Microwave Studio. One turn of helical arm is composed of $n = N_H = 15$ horizontal segments, each having length $L_H = 0.0686\,l$, and $N = N_v = 4$ vertical segments, each having a length $L_v = 1.028\,l$. The helix was designed to be uniform (i.e., not tapered), with a $C/l = 1$ at 1.25 GHz, which produced a helix diameter of 76.2 mm. A standard coaxial connector (RG141), was modeled to feed the helix with its center conductor connected to the helix and the outer conductor attached to the ground plane. Through a comprehensive optimization process, the design parameters for the helical antenna were defined. The parameters are listed in Table 4.

Design Parameters	Dimensions
Diameter of helix, D	76.2 mm
Number of turns, N	4
Pitch angle, α	13.5°
Number of segments for each turn, n	15
Coaxial connector, feed radius (RG141)	1.7907 mm
Diameter of ground plane, D_{GP} ($\geq 3D$)	240 mm
Thickness of ground place	15 mm
Substrate, Teflon, ε_r (RG141)	2.03
Substrate length (RG141)	15 mm
Substrate radius (RG141)	5.3721 mm

(a). Design Parameters

Design Parameters	Dimensions
Circumference of helix, $C = \pi D (= \lambda)$	239.39 mm
Spacing between each turn, $S = C \tan\alpha$	57.47 mm
Axial length, $L = NS$	229.88 mm
Length of 1 turn, $L_o = \sqrt{S^2 + C^2}$	246.19 mm
Total length of wire, $L_n = NL_0$	984.76 mm
Total length of wire including feed length	1,009.27 mm
Impedance, $R \approx 140(C/\lambda)$	140 Ω
Axial ratio, $\mathrm{AR} \approx (2N+1)/2N$	1.125
Directivity, $D_0 = 10\log_{10}\{15N(C^2 S/\lambda^3)\}$	11.58 dB

(b). Calculated Parameters

Design Parameters	Dimensions
Radius of helix wire, a	6.35 mm
Coaxial connector, feed length (RG141)	25.41 mm

(c). Optimized Parameters

Table 4. **Dimensions of parameters for the monofilar helix.**

Figures 25 and 26 show plots of S_{11} for the monofilar helix with variation in its feed length and helix wire radius, respectively. The scattering parameter S_{11} is the ratio of the reflected voltage over the incident voltage (i.e., reflection coefficient). The decibel value is $S_{11},\mathrm{dB} = 20\log_{10}(S_{11})$. Values of S_{11} less than -10 dB are generally considered acceptable, but values of -15 dB or less are more desirable. The optimal values are reflected in Table 4(c). Figures 27 to 47 give various results for the monofilar helix with a ground plane using the design parameters listed in Table 4(a).

Figure 25 shows the effect that the feed length has on the overall input scattering parameter (i.e. reflection coefficient), S_{11}, of the helix. It is obvious that when the feed length is at 25.14 mm, an optimum S_{11} is obtained. Thus, for subsequent simulations, a feed length of 25.14 mm was used. Similarly, it can be seen that the radius of the helix wire affects the input reflection coefficient. From Figure 26, for a more favorable S_{11}, the helix wire radius is chosen to be 6.35 mm.

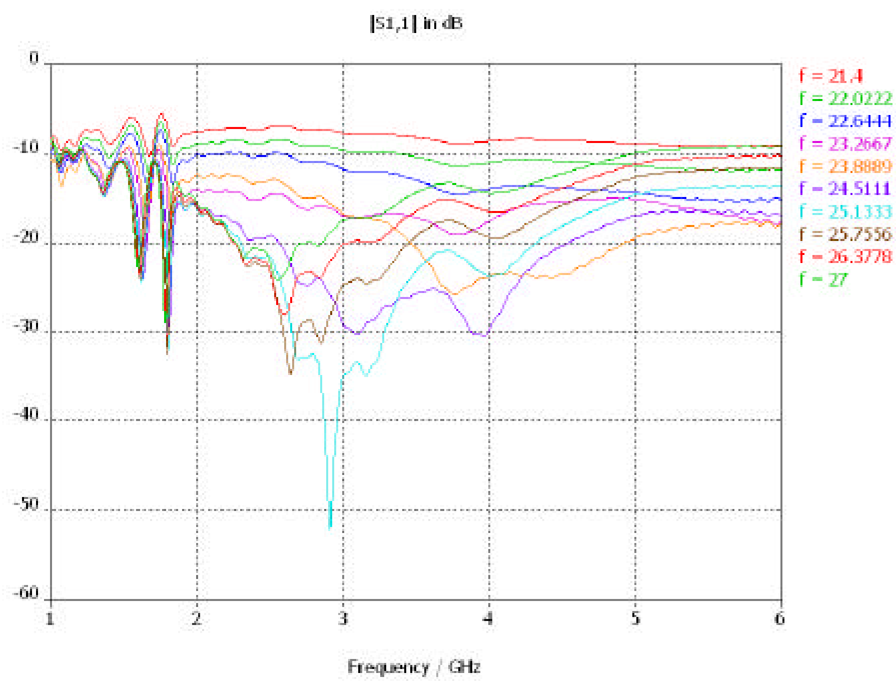

Figure 25. **Plot showing the optimization of the feed length for the monofilar helix.**

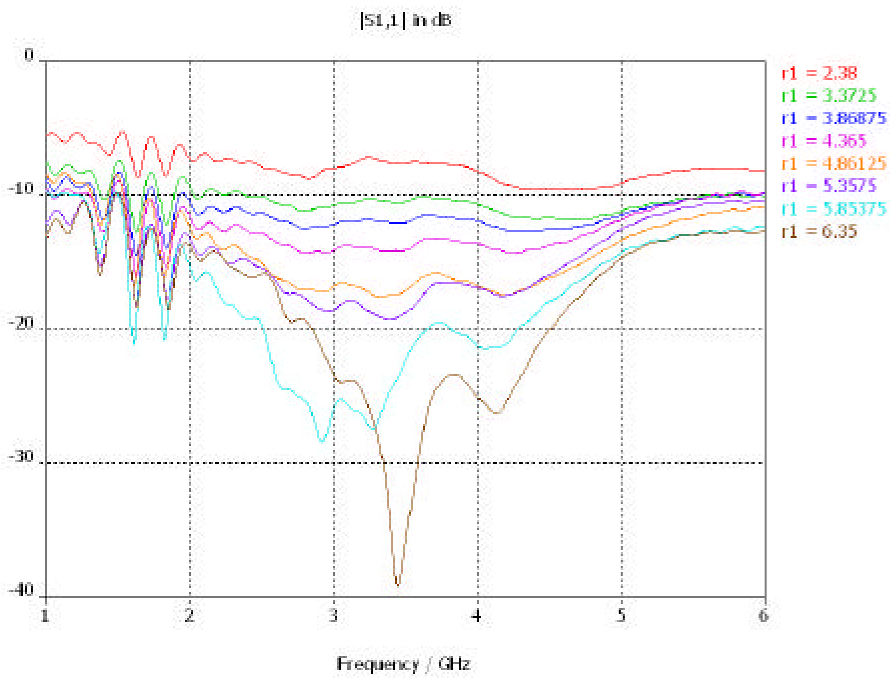

Figure 26. **Plot showing the optimization of the helix wire radius (*a*) for the simulated monofilar helix.**

The radiation pattern for the optimum feed length and wire radius for the monofilar helix is shown in Figures 27 and 28, where the axial beam is circularly polarized over a wide angular region around the *y*-axis. Figure 29 shows the input reflection coefficient for the same design parameters. An acceptable frequency bandwidth is based on a S_{11} better than –10 dB criterion. From Figure 29, it can be seen that the bandwidth is large and spans several octaves. However, Microwave Studio is unable to simulate higher frequencies for certain models because the total number of cells (increased at lower wavelengths) is beyond the limit of available computer memory. Therefore, the number of mesh cells is limited to approximately 5 million for all simulations. Figure 30 shows the impedance on a Smith chart.

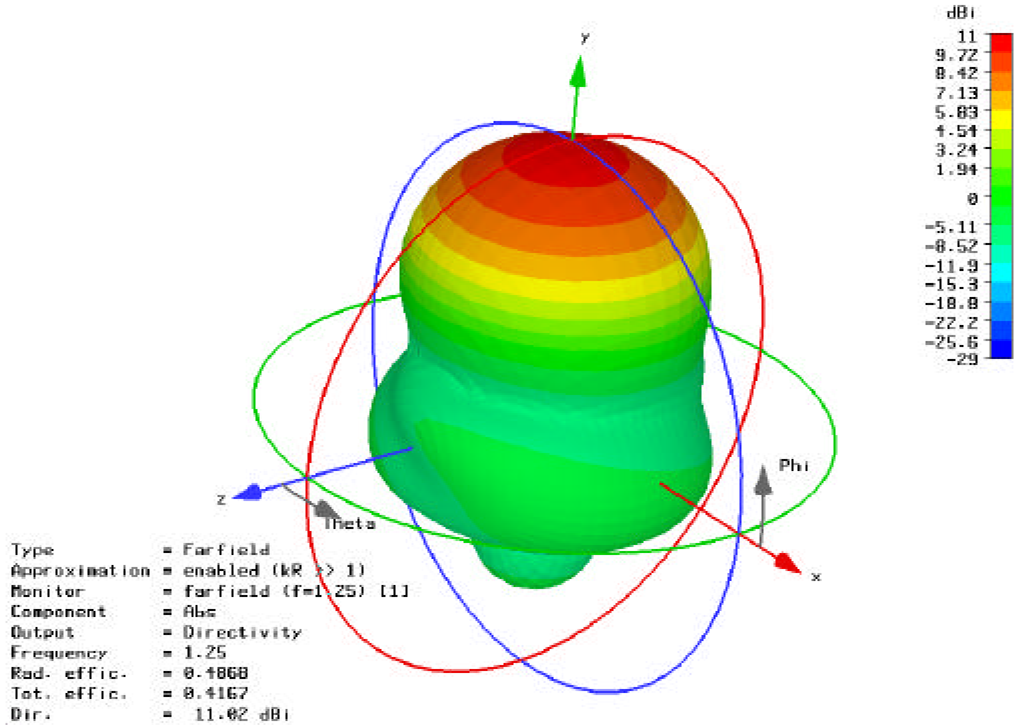

Figure 27. **Three-dimensional radiation pattern plot for the simulated optimum monofilar helix at 1.25 GHz.**

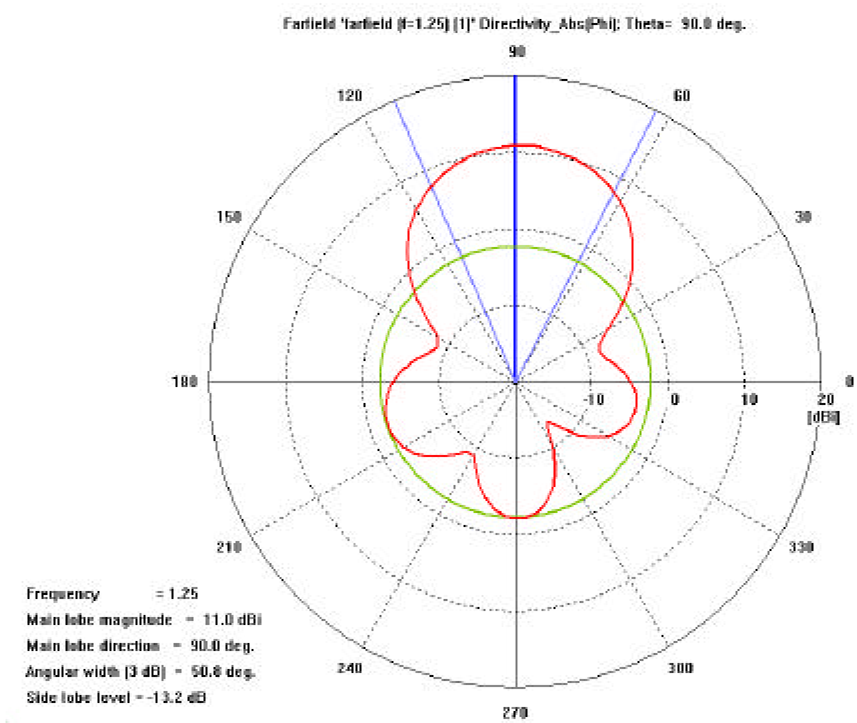

Figure 28. **Far-field directivity plot at $q = 90^{o}$ for the simulated optimum monofilar helix at 1.25 GHz.**

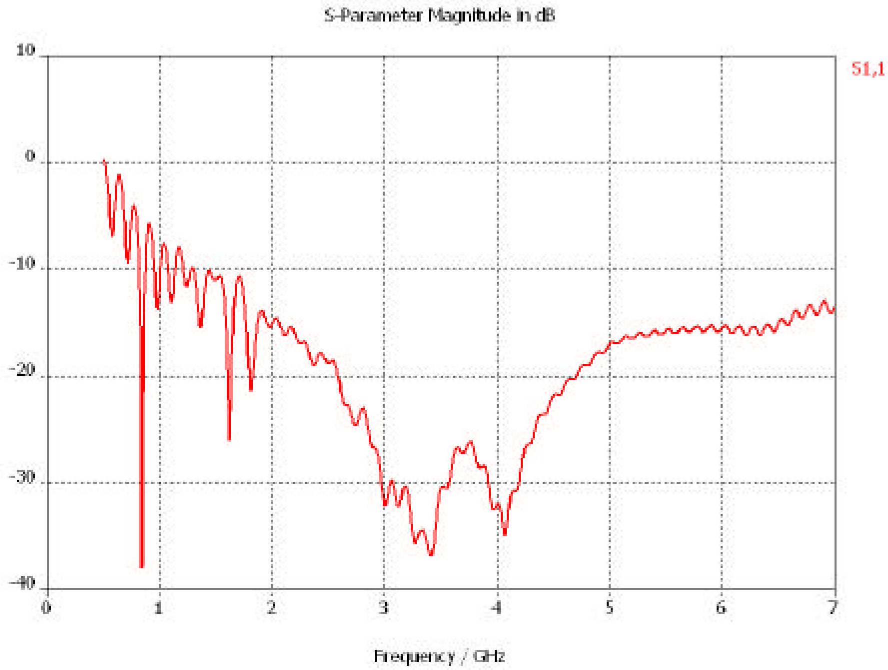

Figure 29. **Plot showing the variation of input scattering parameter (S_{11}) for the simulated monofilar helix.**

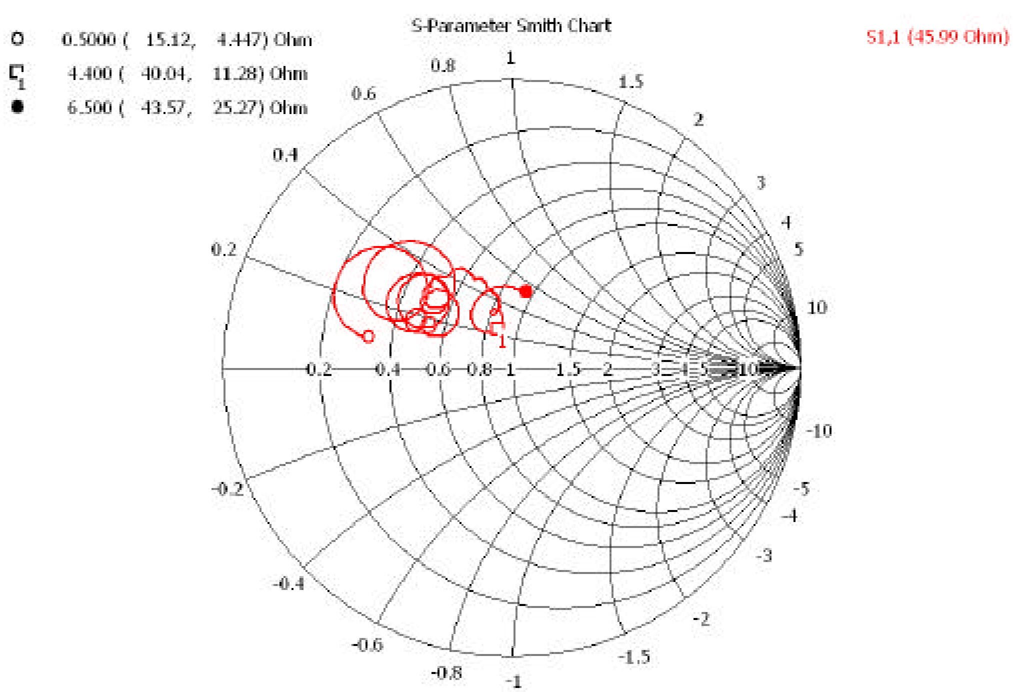

Figure 30. **Smith chart plot for the simulated monofilar helix.**

Figure 31 shows the far-field axial ratio in the xy-plane. It can be seen that the monofilar helix is circularly polarized in its main beam ($q = 90^\circ$ and $0^\circ \leq f \leq 90^\circ$) at 1.25 GHz. It is circularly polarized within $\pm 30^\circ$ of $q = 90^\circ$. The beam is circularly polarized and is more sensitive to changes in frequency than is the pattern shape. Figure 32 plots the directivity pattern, which peaks at $q = 90^\circ$ and $f = 90^\circ$. Figures 33 and 34 show the frequency response magnitude and phase of the input impedance of the helix antenna. The terminal input impedance ($Z_{\text{in}} = R + jX \approx R$) radiating in the axial mode is nearly resistive with values between 100 Ω and 200 Ω. Smaller values, near 50 ohms, can be achieved by properly designing the feed [27]. Since the diameter of the helix wire was optimized for S_{11}, and the size of the diameter significantly influences the input impedance, the simulations did not yield the expected theoretical results of the input impedance. The difference between theory and simulation can also be attributed to the finite arm length and the phase difference added by the feed length.

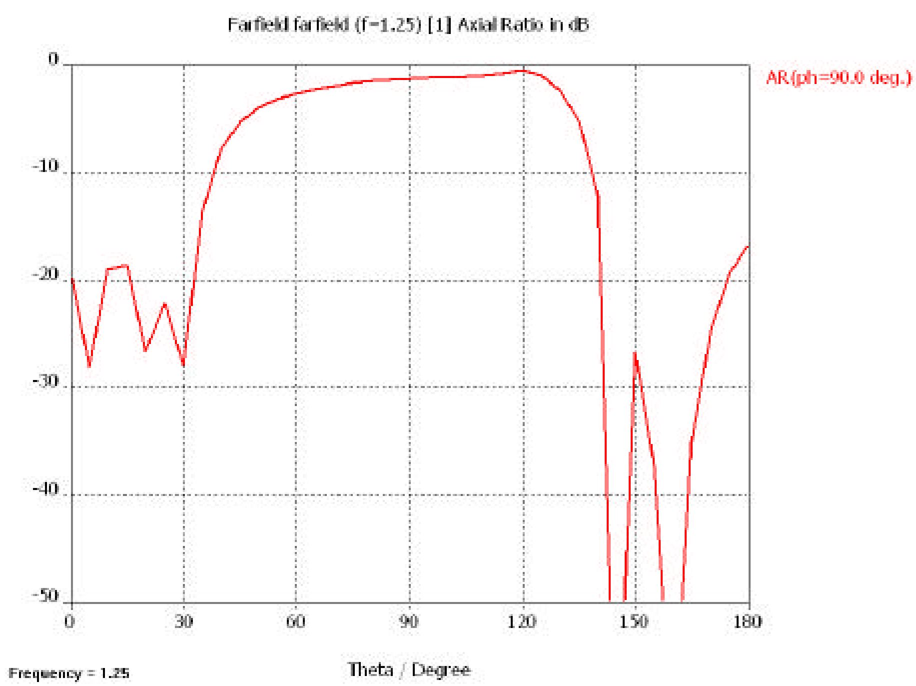

Figure 31. **Far-field axial ratio plot for the simulated optimum monofilar helix at 1.25 GHz.**

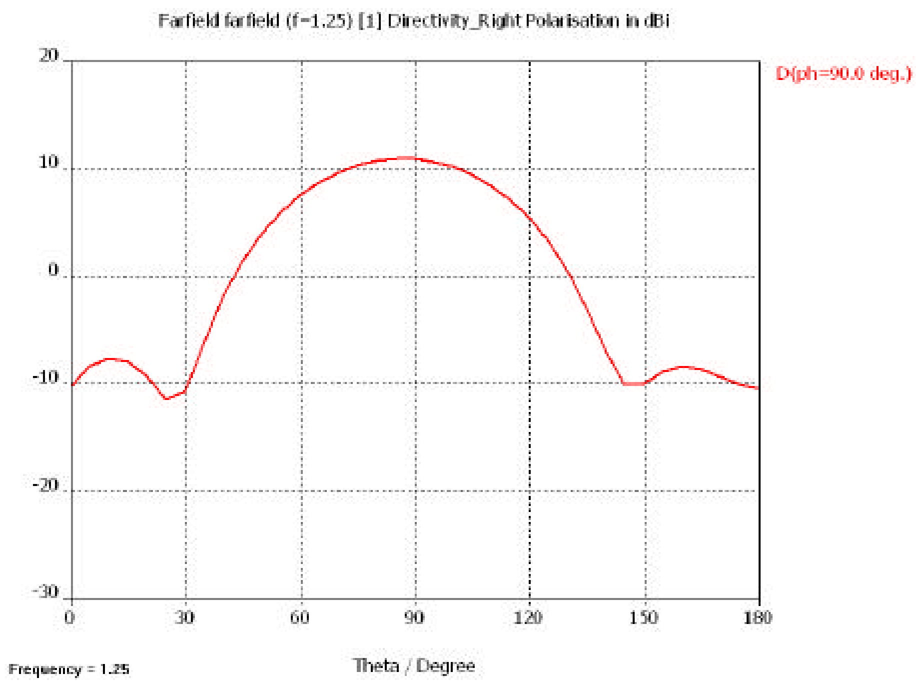

Figure 32. **Directivity plot for $f = 90°$ for the simulated optimum monofilar helix at 1.25 GHz.**

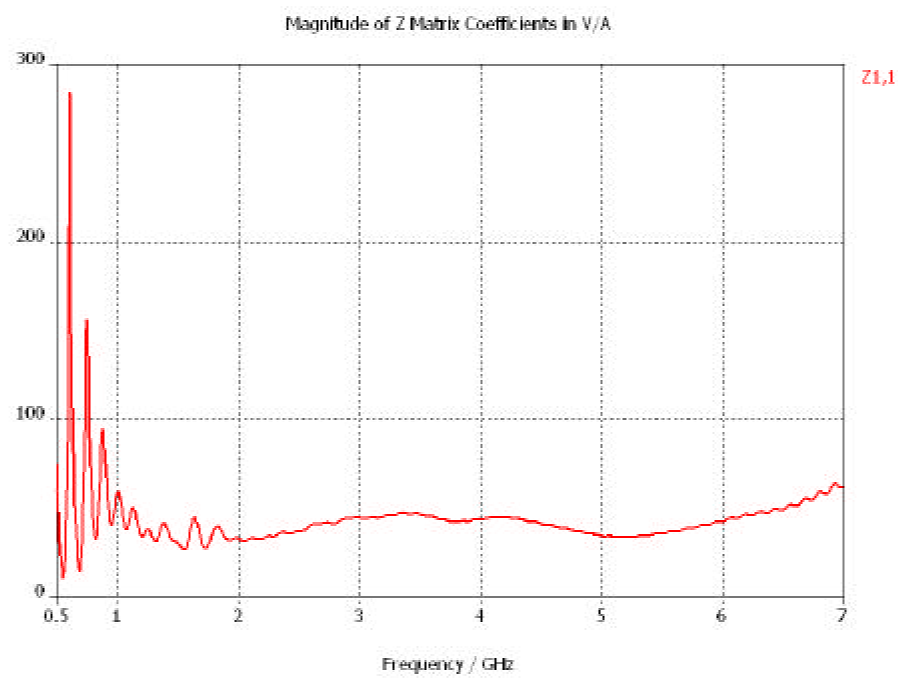

Figure 33. **Plot showing the variation of input impedance magnitude with frequency for the simulated optimum monofilar helix.**

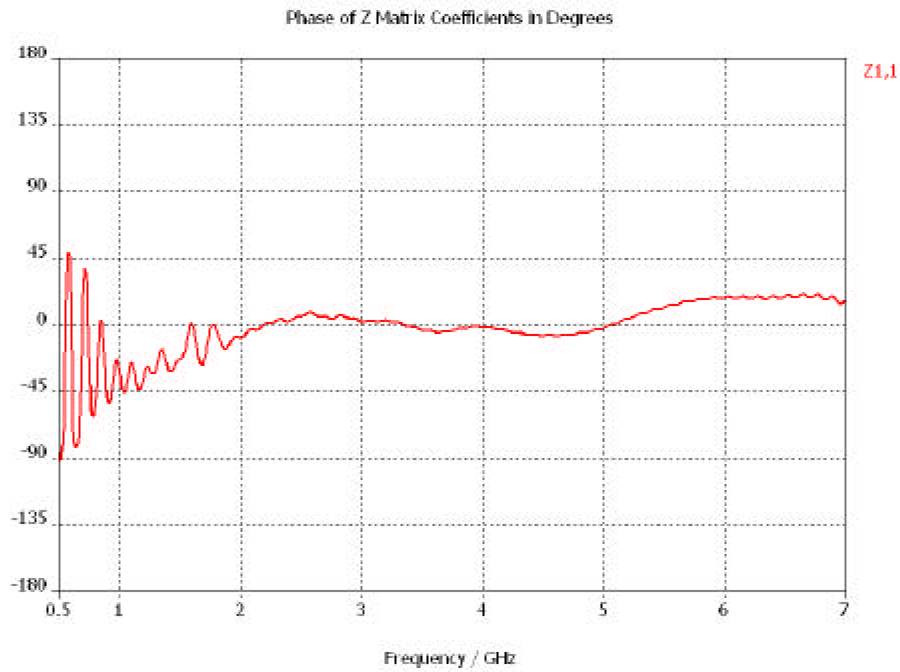

Figure 34. **Plot showing the variation of input impedance phase with frequency for the simulated optimum monofilar helix.**

Figures 35 and 36 show the same monofilar helix with the ground plane removed. Figure 35 serves to confirm that the finite ground plane acts to reduce or minimize the back radiation.

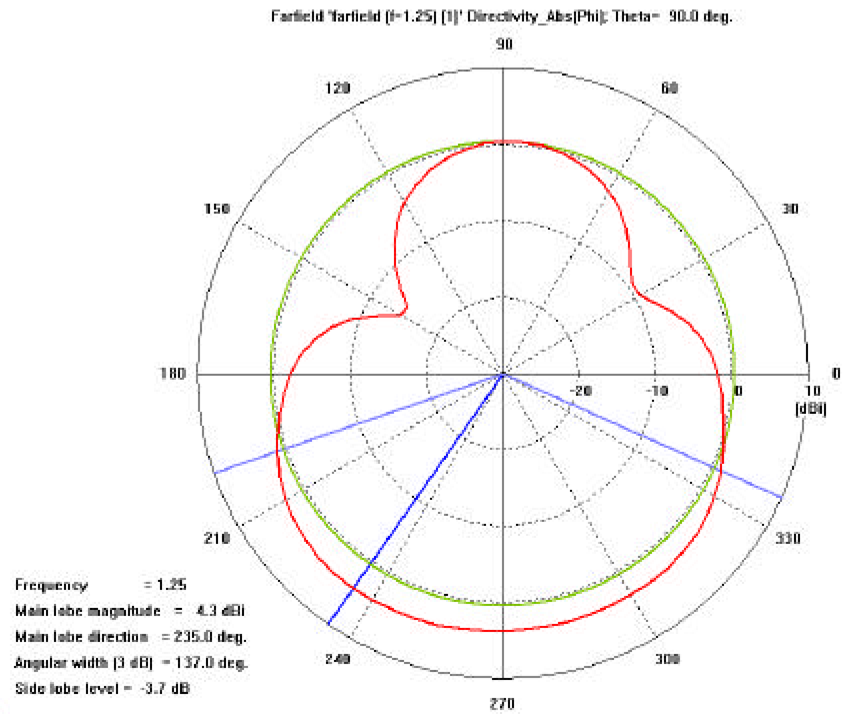

Figure 35. **Far-field directivity plot at $q = 90^{o}$ for the simulated monofilar helix without a ground plane at 1.25 GHz.**

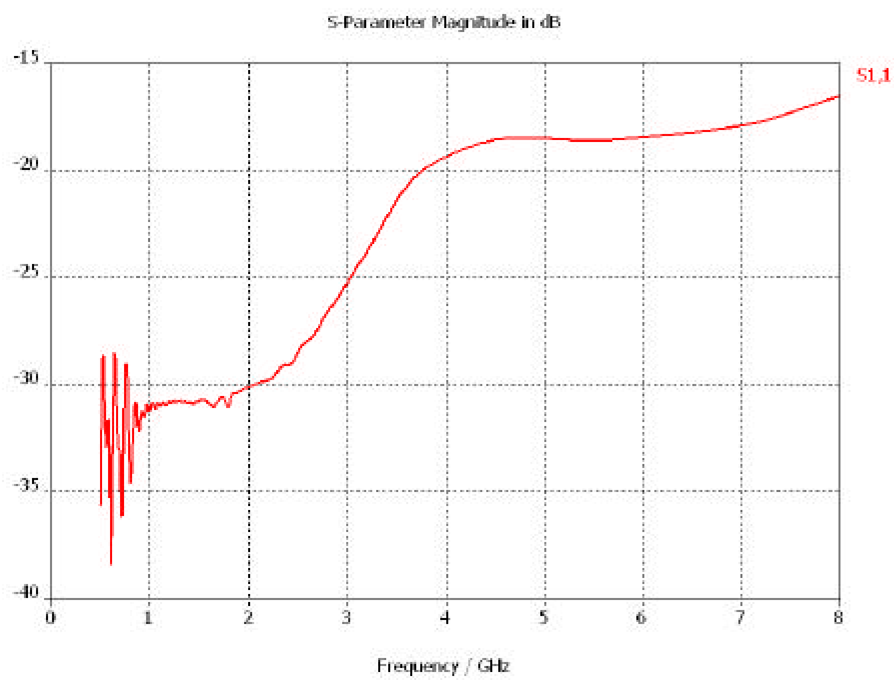

Figure 36. **Plot showing the variation of input scattering parameter (S_{11}) for the simulated monofilar helix without a ground plane.**

Figures 37 to 40 show how the beam pattern changes for different values of C/λ. As discussed in Chapter III, the helix operates in the axial mode for $3/4 < C/\lambda < 4/3$. At frequencies below the break point, $C/\lambda < 3/4$, the monofilar helix radiates in the normal (dipole) mode. While for radiation patterns $C/\lambda > 4/3$, it exhibits pattern beam-splitting.

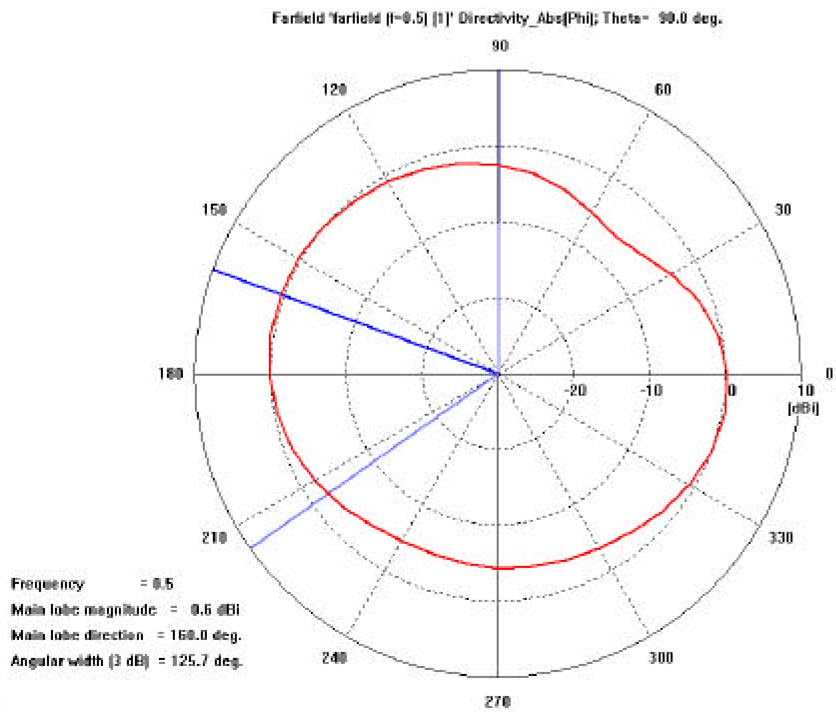

Figure 37. **Far-field directivity plot at $\theta = 90^o$ for the simulated monofilar helix for $C/\lambda = 2/5$ ($< 3/4$) .**

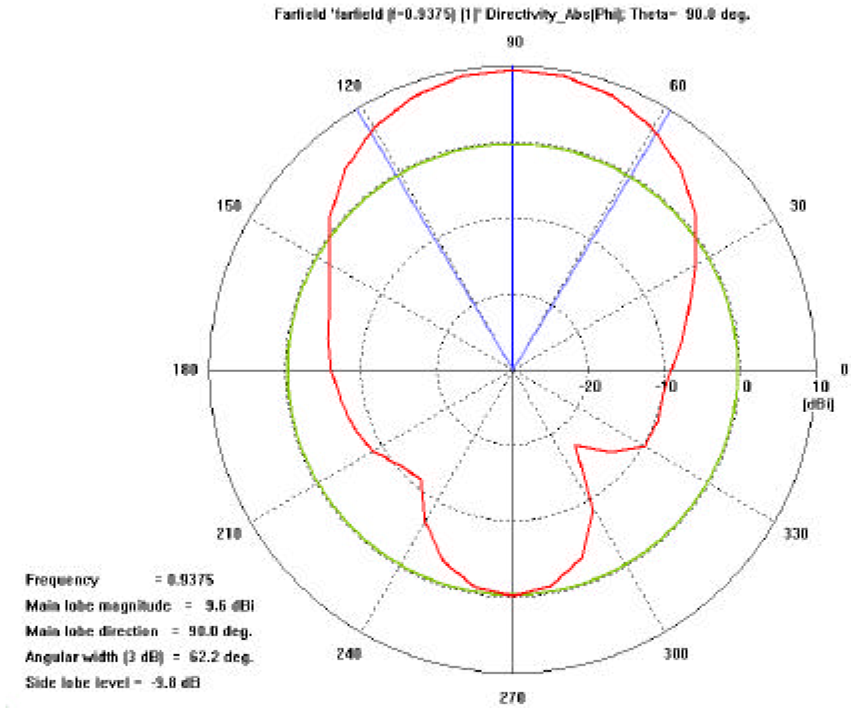

Figure 38. **Far-field directivity plot at $q = 90^{o}$ for the simulated monofilar helix for $C/l = 3/4$.**

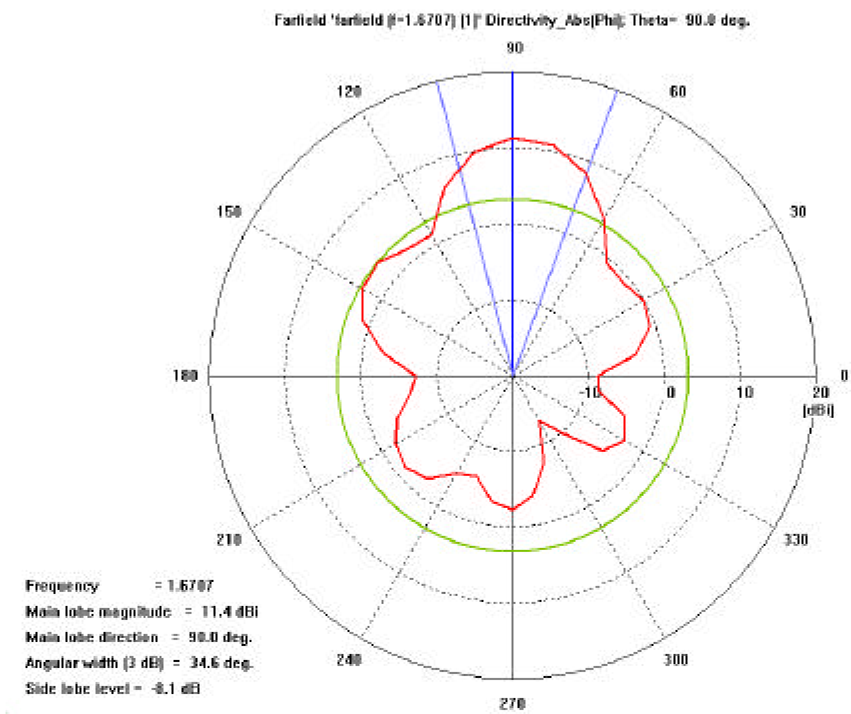

Figure 39. **Far-field directivity plot at $q = 90^{o}$ for the simulated monofilar helix for $C/l = 4/3$.**

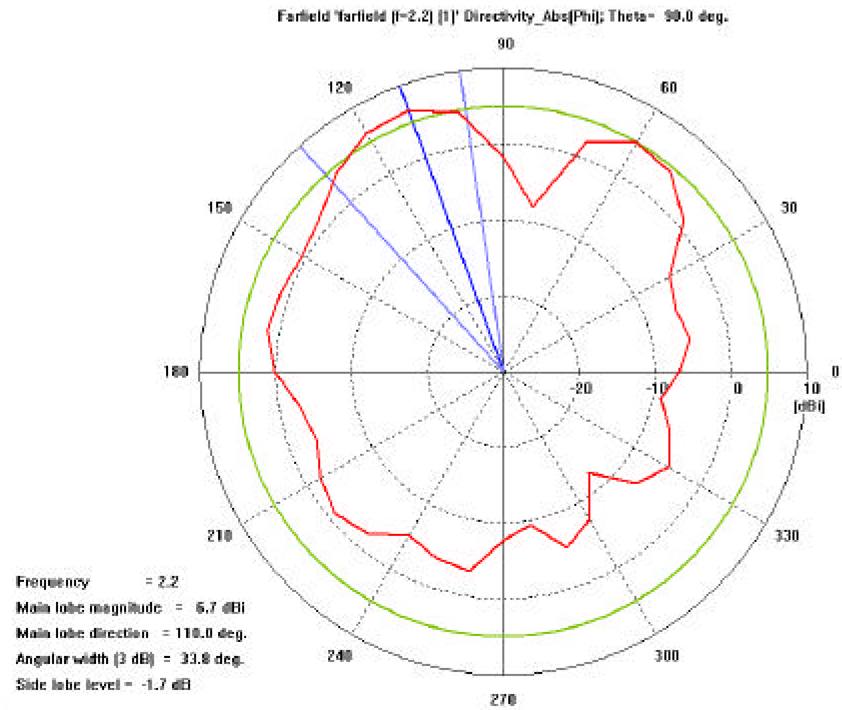

Figure 40. **Far-field directivity plot at $q = 90^o$ for the simulated monofilar helix for $C/l = 9/5$ (>4/3) .**

Another way to improve the bandwidth is to taper the ends of the helix [30]. Figures 41 and 42 show the S_{11} and the far-field axial ratio plots for a tapered helix. It can be seen that the S_{11} is significantly improved providing a much wider bandwidth. This result is depicted here for comparison and illustration purposes only. Initially, the impedance matching of the antenna was very bad and tapering was considered in order to improve the match. However, after optimizing the thickness of the wire and length of the feed as highlighted in Table 4(c), acceptable performance was achieved without tapering.

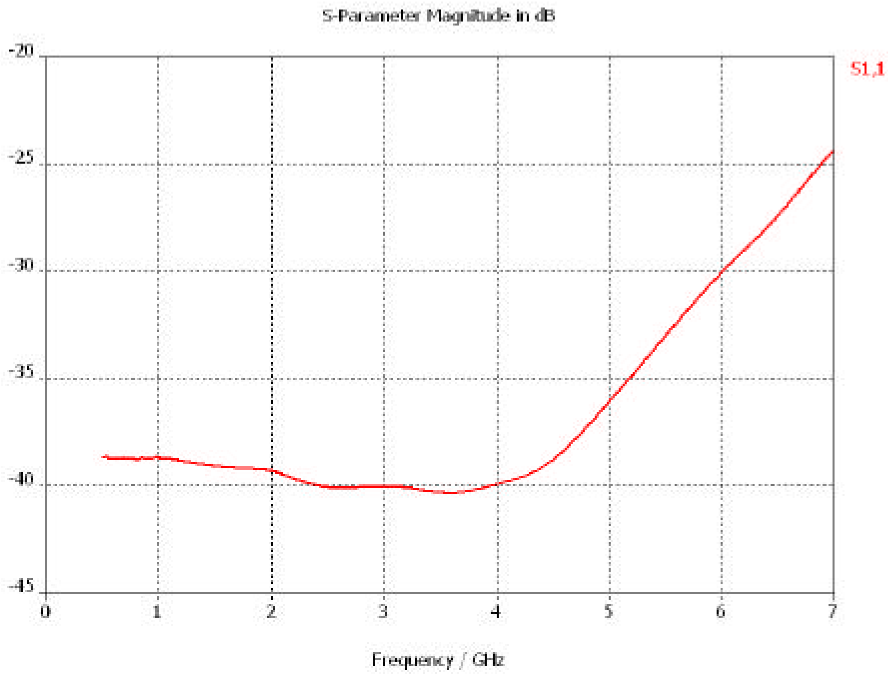

Figure 41. **Plot showing the variation of input scattering parameter (S_{11}) for the simulated tapered monofilar helix.**

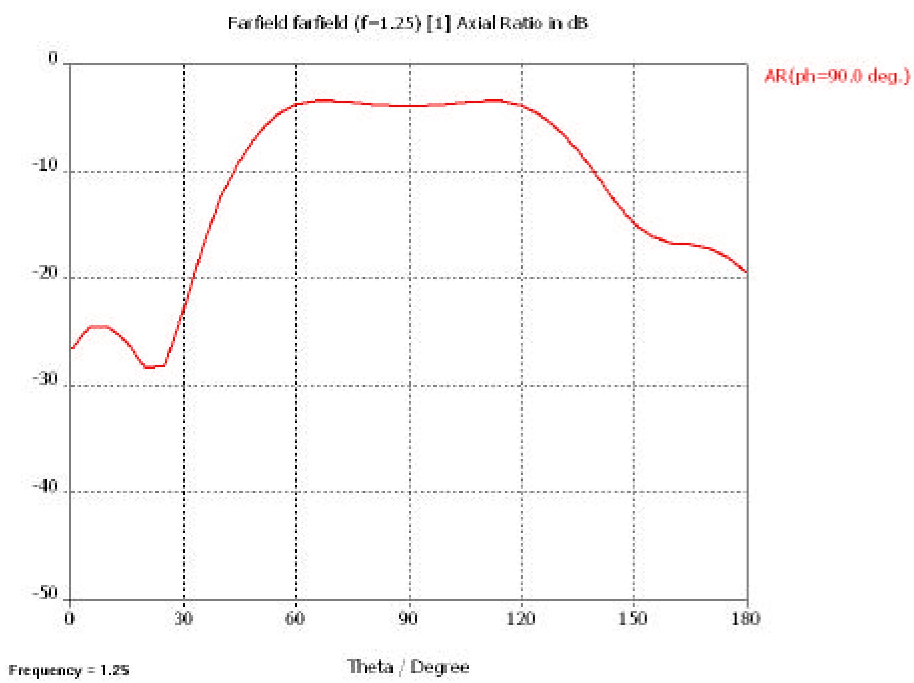

Figure 42. **Far-field axial ratio plot for the simulated tapered monofilar helix at 1.25 GHz.**

Figures 43 and 44 show the input scattering parameter, S_{11}, for the monofilar helix with different feed lengths. It is imperative that correct feed length is selected. Figure 45 shows the same helix but with half the ground plane thickness. The results are similar to the original helix. The reason that thicker ground planes were used in the earlier simulations was because Microwave Studio kept running into software errors when the waveguides were too short. Thus, a thick ground pane is used to improve the numerical stability of the simulation, and is not required for a real design.

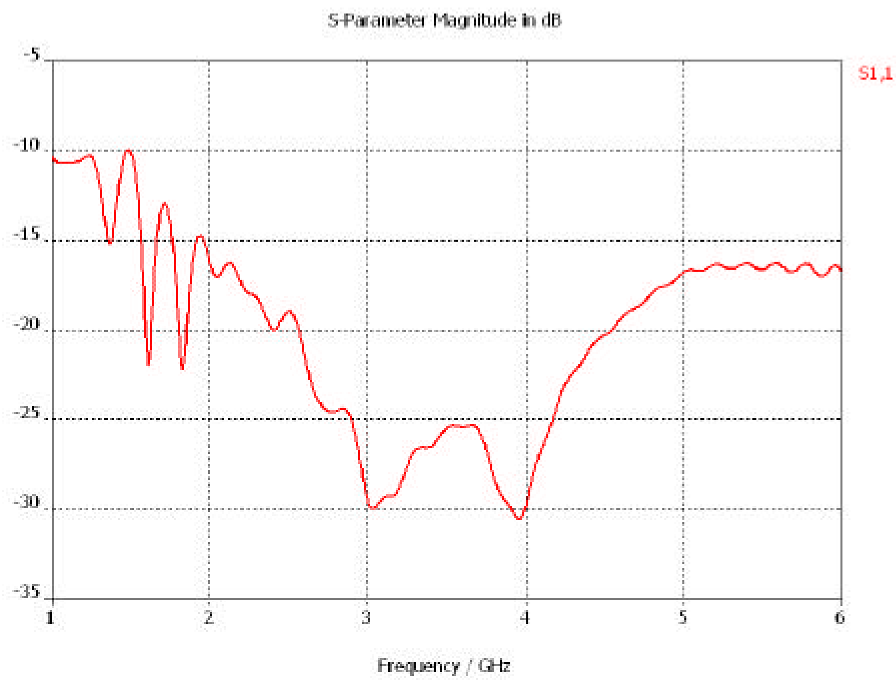

Figure 43. **Plot showing the variation of input scattering parameter (S_{11}) for the simulated monofilar helix with a feed of 21.4 mm.**

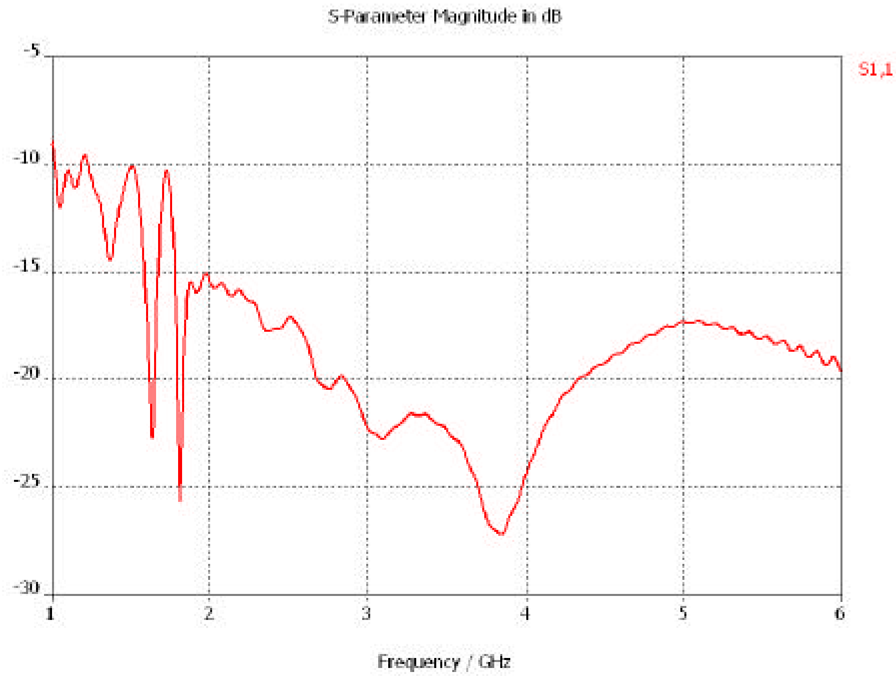

Figure 44. **Plot showing the variation of input scattering parameter (S_{11}) for the simulated monofilar helix with a feed of 24 mm.**

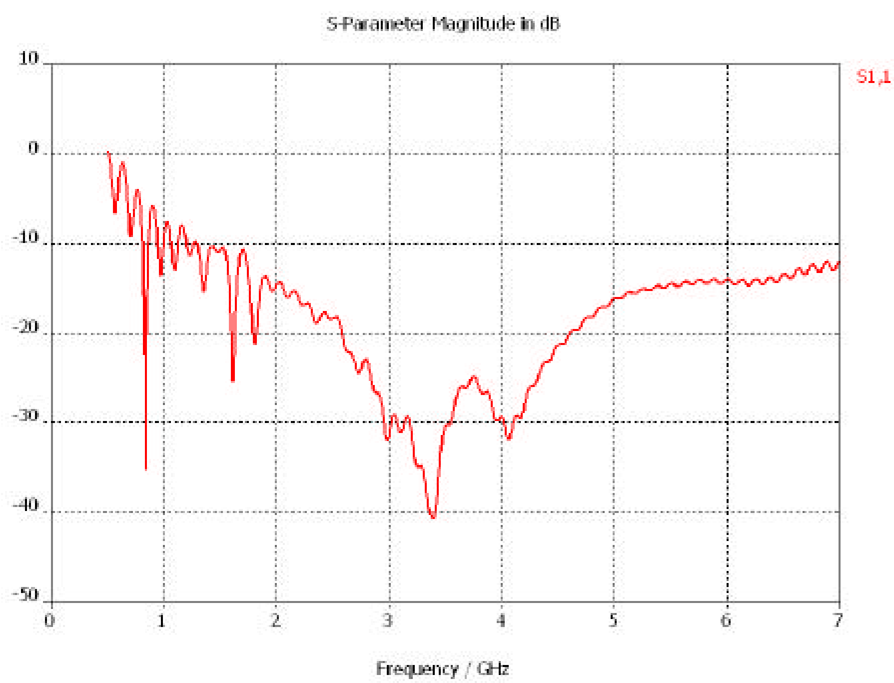

Figure 45. **Plot showing the variation of input scattering parameter (S_{11}) for the simulated monofilar helix with 7 mm ground plane thickness.**

Figures 46 and 47 show S_{11} and far-field directivity plots for a monofilar helix with its pitch angle set at $35°$, which is suitable for a quadrifilar helical antenna. It is evident from the S_{11} plot that the reflection loss has improved significantly. The higher pitch angle has reduced the input impedance to match with the coaxial input, thus resulting in a better reflection coefficient. However, the radiation plot has not turned out well. This only illustrates the importance of finding a right balance between the different dimensions for an overall improved performance.

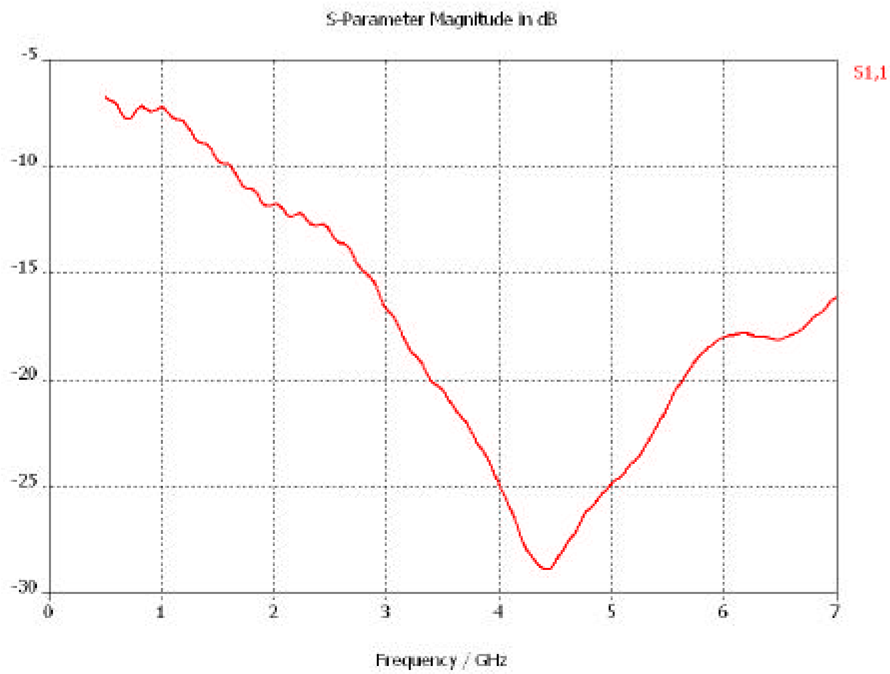

Figure 46. **Plot showing the variation of input scattering parameter (S_{11}) for the simulated monofilar helix with pitch angle set at $a = 35°$.**

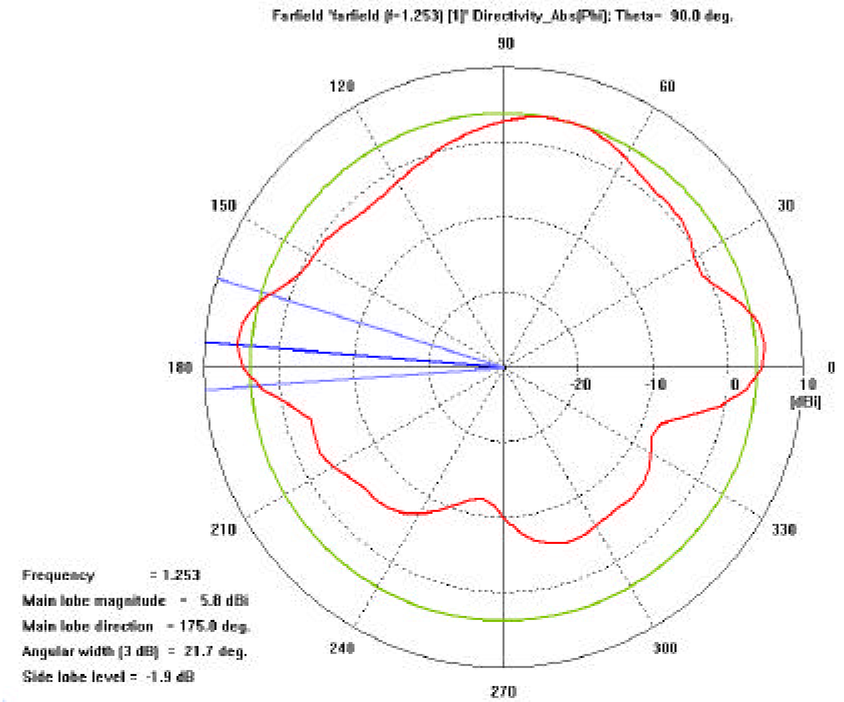

Figure 47. **Far-field directivity plot at $\theta = 90^\circ$ for the simulated monofilar helix with pitch angle set at $\alpha = 35^\circ$ at 1.25 GHz.**

Table 4 provides a summary of the performance parameters for the monofilar helix, both with and without ground plane, as obtained from Microwave Studio.

Performance Parameters	**Simulated Results**		**Theoretical Results**
	Without Ground Plane	**With Ground Plane**	
Directivity at 1.25 GHz	4.3 dBi	11 dBi	11.5 dBi
Axial Ratio at 1.25 GHz	Circular (<-10dB) at $\phi = 90^\circ$ and $45^\circ < \theta < 135^\circ$	Circular (<-10dB) at $\phi = 90^\circ$ and $45^\circ < \theta < 135^\circ$	1.125
S_{11} (< -10 dB)	From 1.2 GHz to > 8 GHz	From 1.2 GHz to > 7 GHz	-
Magnitude of Input Impedance	-	35 to 60 Ω	50 Ω
Side Love Level	-13.2 dB	-3.7 dB	-
Bandwidth (S_{11} at -10 dB)	> 6.8 GHz	> 5.8 GHz	-

Table 5. **Summary of the performance parameters for the simulated monofilar helix with and without ground plane.**

1. Observed Relationships

The parameters of the antenna all affected the simulation results as expected (as discussed in Chapter III). The most important parameter to observe was the input scattering parameter and the effect that various parameters had on its value. In this sense, the optimum helical antenna had the helix raised 9.51 cm above the ground plane. The wire connecting the helix to the coaxial feed was of a different radius than the helix wire. The input angle of the connecting wire also had a great effect on the impedance. A number of the above variables had a pronounced effect on the radiation pattern. The following effects were demonstrated through a series of simulations and by and large have been reported in the previously cited literature.

a). The beamwidth can be reduced, and thus the directivity increased, by increasing the number of turns, N.

b). The diameter of the conductor has negligible effect on the axial mode helical antenna, although it has an effect on the input impedance of the antenna.

c). By increasing the number of segments making each turn, the radiation pattern becomes more well defined and directive.

d). The antenna is slightly raised above the ground plane for the input feed point. From the simulations, it was noticed that the shorter the gap between the antenna and the ground plane (i.e. the shorter the feed wires), the better the impedance match to $50\,\Omega$. When the feed length was 24.51 mm, the optimum performance was achieved.

e). The optimum diameter for the helix wire was found to be 6.35 mm. As the diameter increased, the input impedance would decrease. Conversely, as the diameter of the wire decreased, the impedance of the antenna would increase. This allowed the expected input impedance of 140Ω to be brought down to almost $50\,\Omega$.

Theory dictates that the best way to get a good impedance match is to gradually diminish the antenna wire into a flat wire, with a slow, gradual slope into the feed point. However, this is too complex to achieve in an actual antenna.

B. BIFILAR HELIX ANTENNA

Figure 18 shows the configuration structure for the uniform bifilar helical antenna with a ground plane and a coaxial feed as modeled using Microwave Studio. Similar design parameters were used for the bifilar helix as for the monofilar helix. The only difference was the additional arm which was positioned directly opposite the first filament. The second arm was fed with the same amplitude but with a phase difference of 180° so that the radiation of both arms would add in phase, resulting in a constructive interference.

Figures 48 to 58 show various results for the bifilar helix with a ground plane using the design parameters listed in Table 4(a) and the abovementioned phase-excitations.

The radiation pattern for the optimum feed length and wire radius for the bifilar helix is shown in Figures 48 and 49, where the axial beam is circularly polarized over a wide angular region around the *y*-axis.

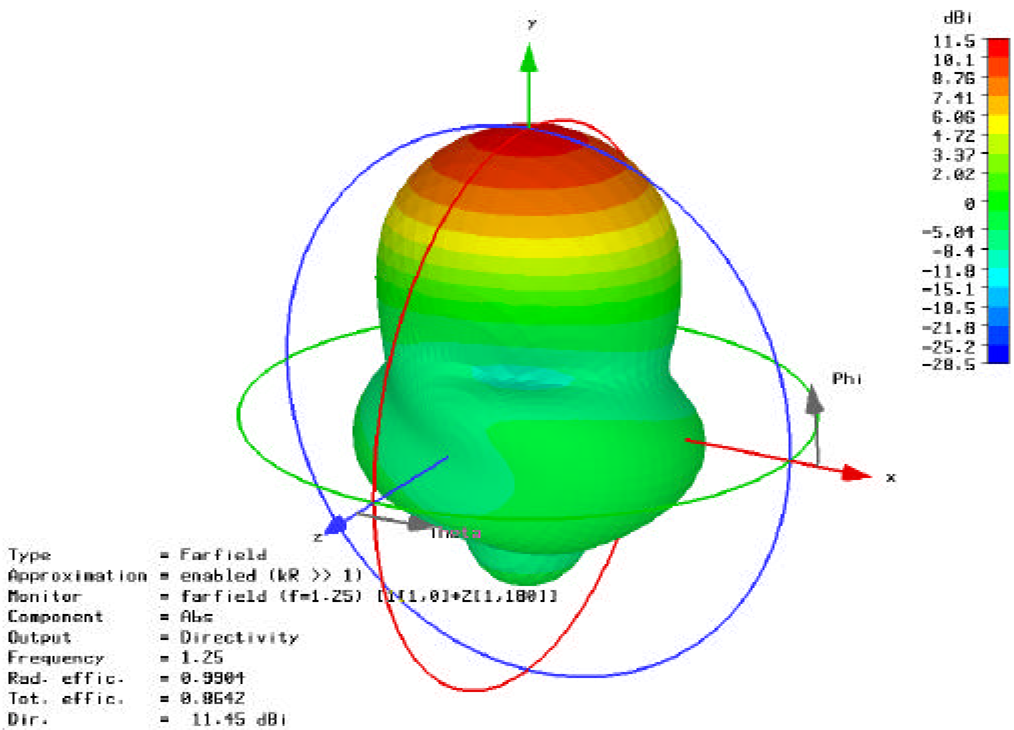

Figure 48. **Three-dimensional radiation pattern plot for the simulated bifilar helix at 1.25 GHz.**

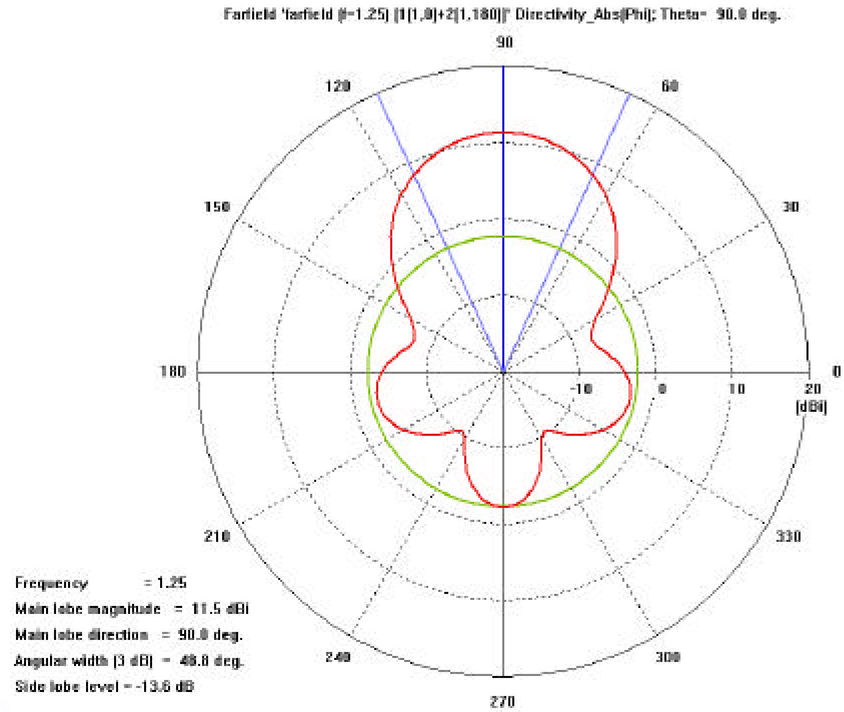

Figure 49. **Far-field directivity plot at $\theta = 90^{o}$ for the simulated bifilar helix at 1.25 GHz.**

Figure 50 shows the input scattering parameter for the bifilar helix. It can be observed that the bandwidth is large and spans several octaves. As in the case of the monofilar antenna, as the modeled structure gets more complex, it utilizes more cells and consequently, Microwave Studio is unable to simulate higher frequencies for that model. Figure 51 shows the far-field axial ratio in the main beam. It is apparent that the bifilar helix is circularly polarized in its main beam near ($\theta = 90°$ and $0° \leq \phi \leq 90°$) at 1.25 GHz. It is circularly polarized within $\pm 45°$ of the beam maximum, a wider range than for the monofilar helix. Figure 52 plots the directivity pattern which peaks at $\theta = 90°$ and $\phi = 90°$.

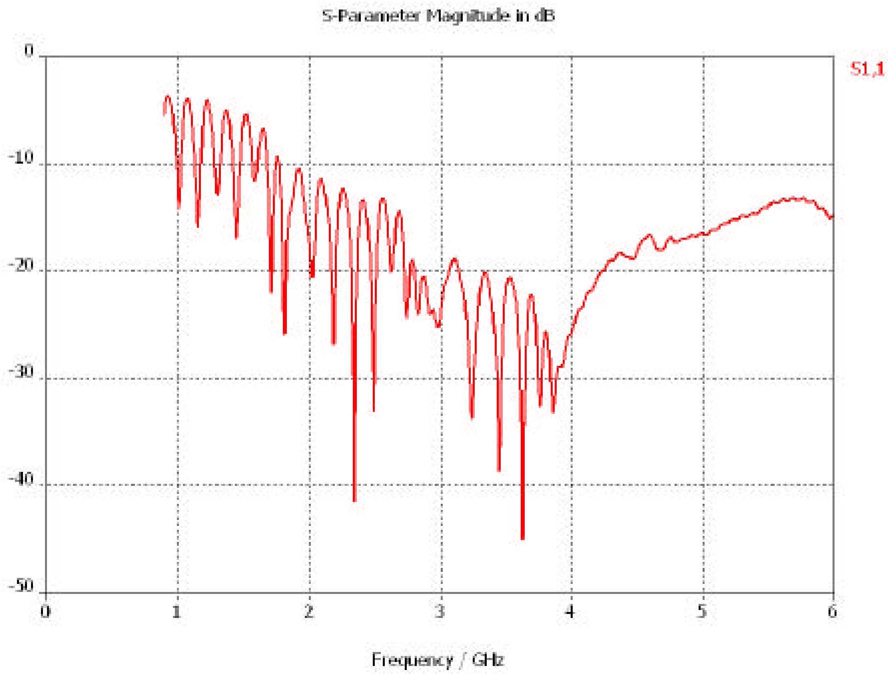

Figure 50. **Plot showing the variation of input scattering parameter (S_{11}) for the simulated bifilar helix.**

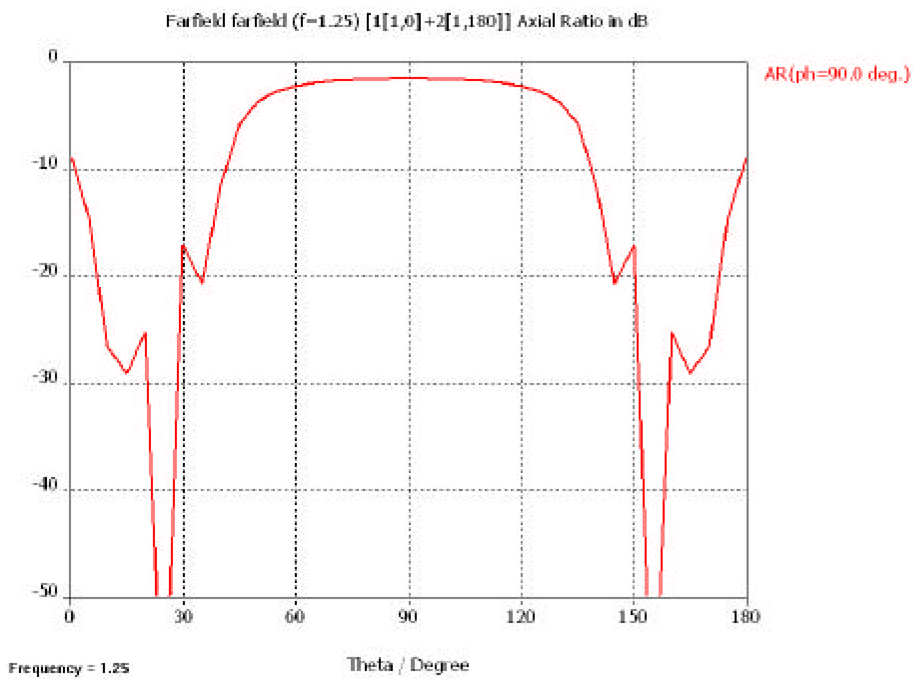

Figure 51. **Far-field axial ratio plot for the simulated bifilar helix at 1.25 GHz.**

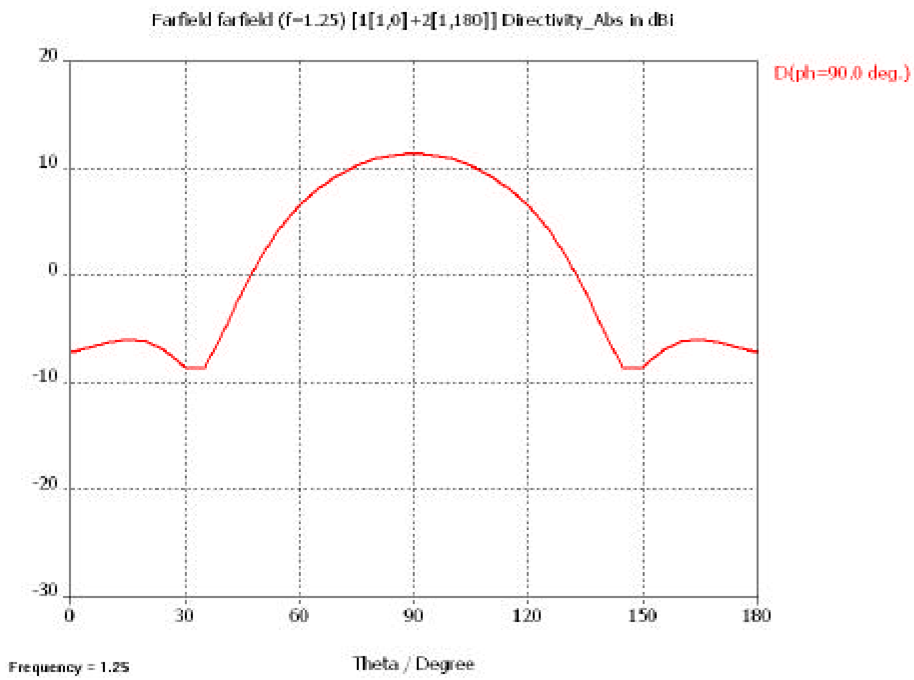

Figure 52. **Directivity plot for $f = 90°$ for the simulated bifilar helix at 1.25 GHz.**

The input impedance of the bifilar helix was not computed in view of the fact that a power divider network, which generally would be used to feed both ports of the helix, was not modeled in Microwave Studio. Instead both the ports were excited separately with the results combined after the simulation by feeding the right amount of phase difference for the two ports.

Figures 53 to 56 show how the beam pattern changes for different values of C/l. As presented in Chapter III, the helix operates in the axial mode for $3/4 < C/l < 4/3$. For $C/l < 3/4$, the radiation is in the normal mode. While for radiation patterns $C/l > 4/3$, it exhibits pattern beam-splitting.

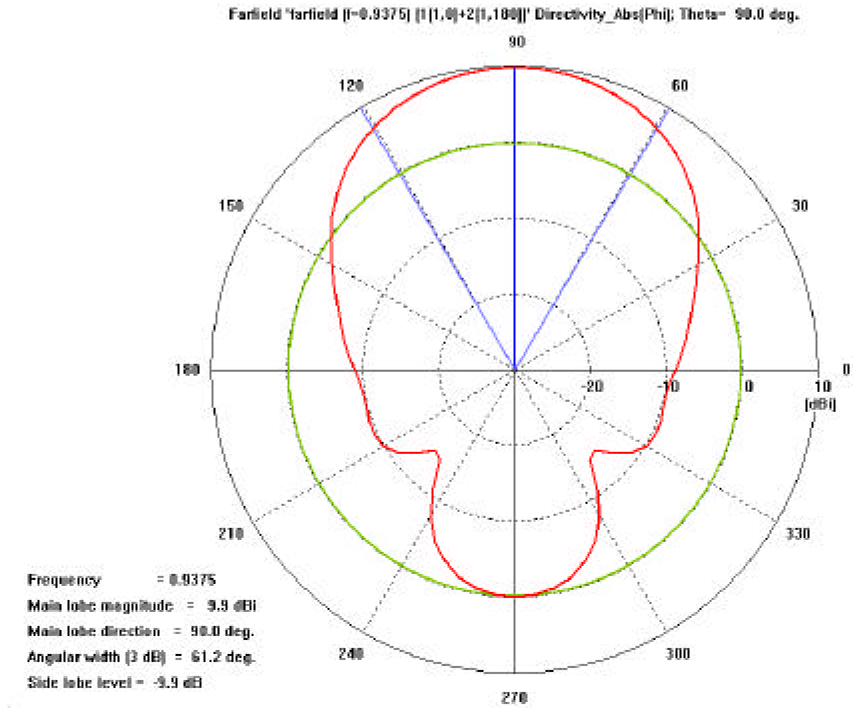

Figure 53. **Far-field directivity plot at $q = 90^o$ for the simulated bifilar helix for $C/l = 3/4$.**

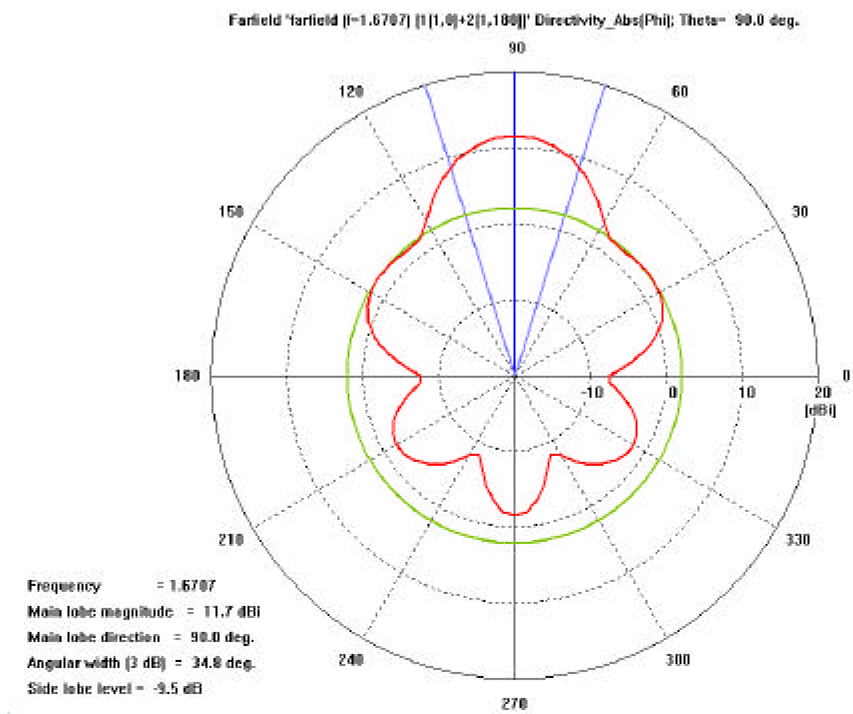

Figure 54. **Far-field directivity plot at $q = 90^o$ for the simulated bifilar helix for $C/l = 4/3$.**

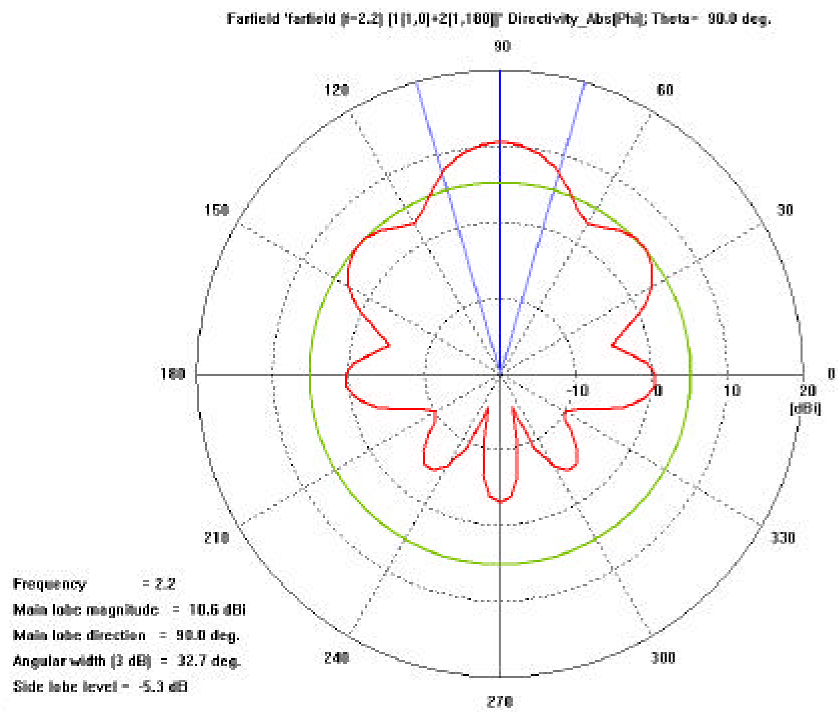

Figure 55. **Far-field directivity plot at $q = 90^o$ for the simulated bifilar helix for $C/l = 9/5$ (>4/3) .**

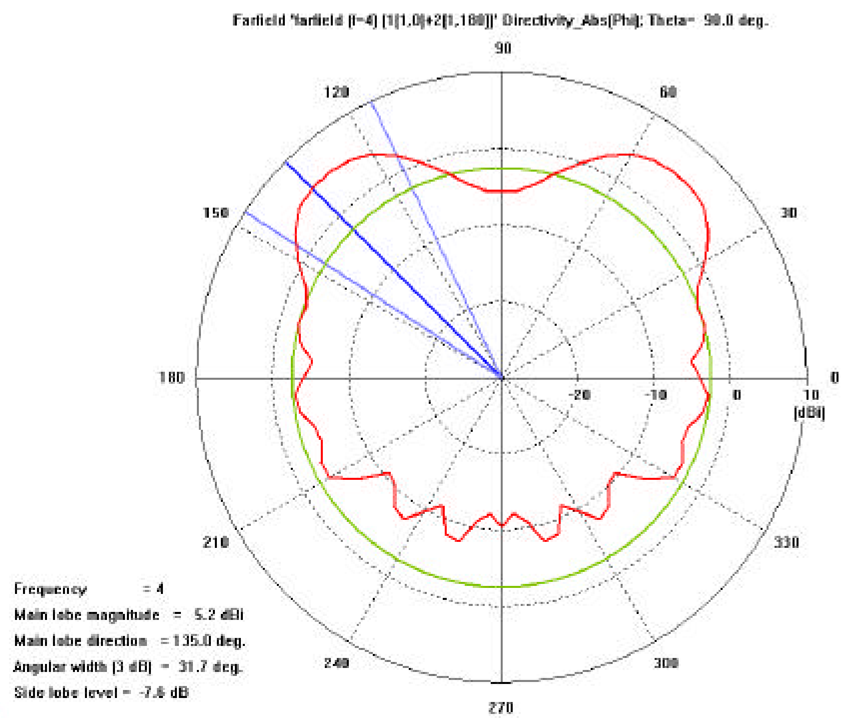

Figure 56. **Far-field directivity plot at $q = 90^o$ for the simulated bifilar helix for $C/l = 3.2$.**

Figures 57 and 58 show the S_{11} and far-field directivity plots for a bifilar helix with its pitch angle set at 35°, which is appropriate for a QHA. It is evident from the S_{11} plot, that the reflection loss has improved significantly. The higher pitch angle has reduced the input impedance to match with the coaxial input, thus resulting in a reduced reflection coefficient. However, the outcome of the radiation plot is far from the anticipated result. This again illustrates the importance of finding a right balance between the different parameters for an overall improved performance.

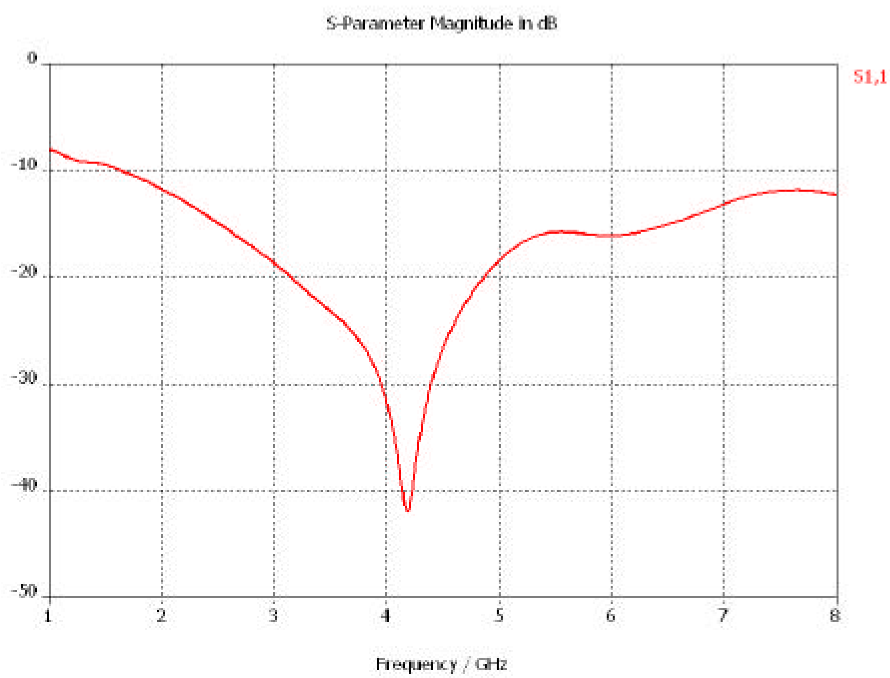

Figure 57. **Plot showing the variation of input reflection coefficient (S_{11}) for the simulated bifilar helix with pitch angle set at $a = 35°$.**

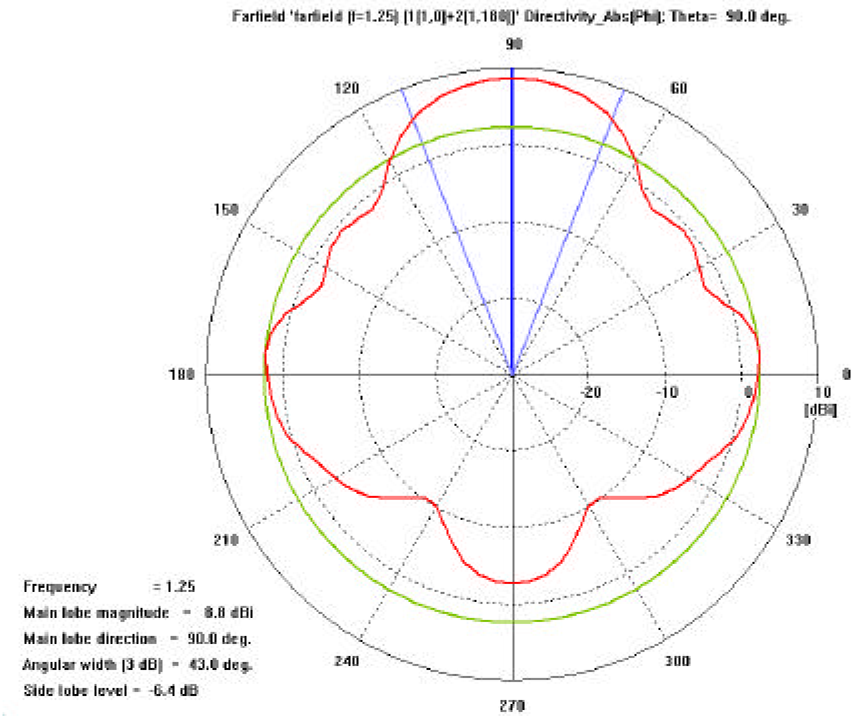

Figure 58. **Far-field directivity plot at $\theta = 90^{o}$ for the simulated bifilar helix with pitch angle set at $\alpha = 35°$ at 1.25 GHz.**

Table 6 provides a summary of the performance parameters for the bifilar and monofilar helix as obtained from Microwave Studio.

Performance Parameters	**Simulated Results**	
	Bifilar Helix	**Monofilar Helix**
Directivity at 1.25 GHz	11.45 dBi	11 dBi
Axial Ratio at 1.25 GHz	Circular (< 10 dB) at $\phi = 90°$ and $45° < \theta < 135°$	Circular (< 10 dB) at $\phi = 90°$ and $45° < \theta < 135°$
S_{11} (< -10 dB)	From 1.8 GHz to > 6 GHz	From 1.2 GHz to > 7 GHz
Side Love Level	-13.6 dB	-13.2 dB
Bandwidth (S_{11} at -10 dB)	> 5.2 GHz	> 5.8 GHz

Table 6. **Summary of the performance parameters for the simulated bifilar and monofilar helix.**

C. QUADRIFILAR HELIX ANTENNA

Figure 19 shows the structure for the uniform QHA with a ground plane and a coaxial feed, as modeled using Microwave Studio. Similar design parameters were used for the QHA helix as for the bifilar antenna. The only difference from the bifilar was the addition of two more arms which are positioned along the circumference of a circle. Each of the four arms of the quadrifilar helix has the same number of turns. The four arms of the helix are excited with sequential phase variation, 0°, 90°, 180°, 270° (1, $-j$, -1, j) [38] to obtain circular polarization so that the radiation of all four arms would add in phase, resulting in a constructive interference.

Figures 59 to 66 show various performance plots for the QHA with a ground plane using the design parameters listed in Table 4(a) and the abovementioned phase excitations.

The radiation pattern for the optimum feed length and wire radius for the bifilar helix is shown in Figures 59 and 60, where the axial beam is circularly polarized over a wide region around the y-axis. It is known that a QHA produces a cardiod-shaped radiation pattern with excellent circular polarization [35,36]. Polarization of quadrifilar helix antenna depends only on helical winding direction [40]. The feed network is the most complicated aspect in the design of the QHA.

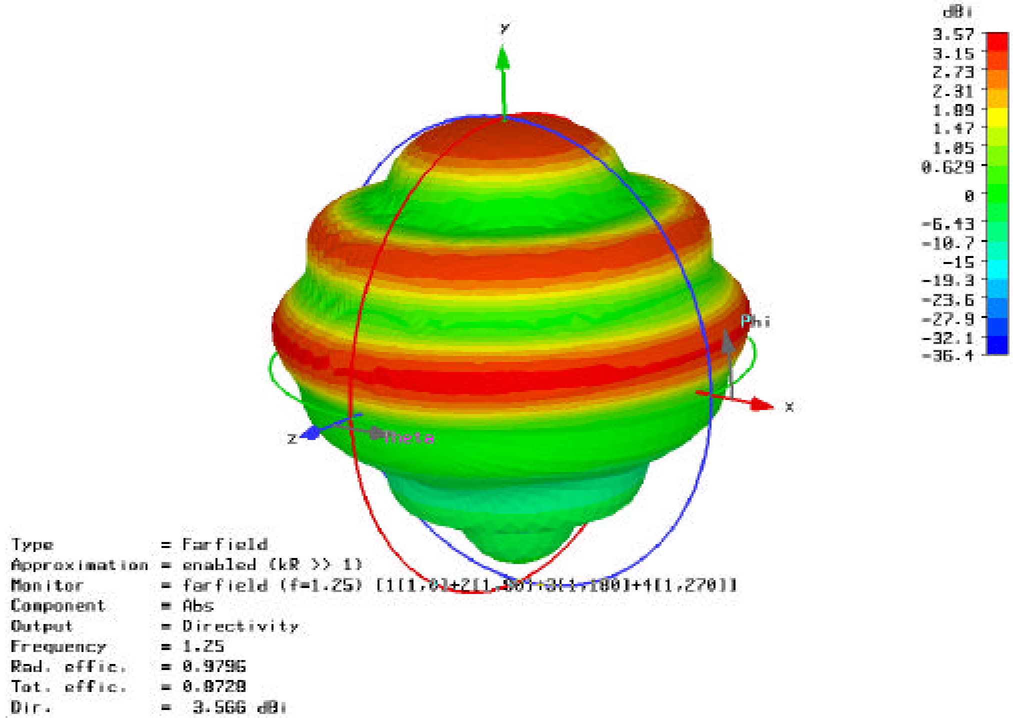

Figure 59. **Three-dimensional radiation pattern plot for the simulated QHA at 1.25 GHz.**

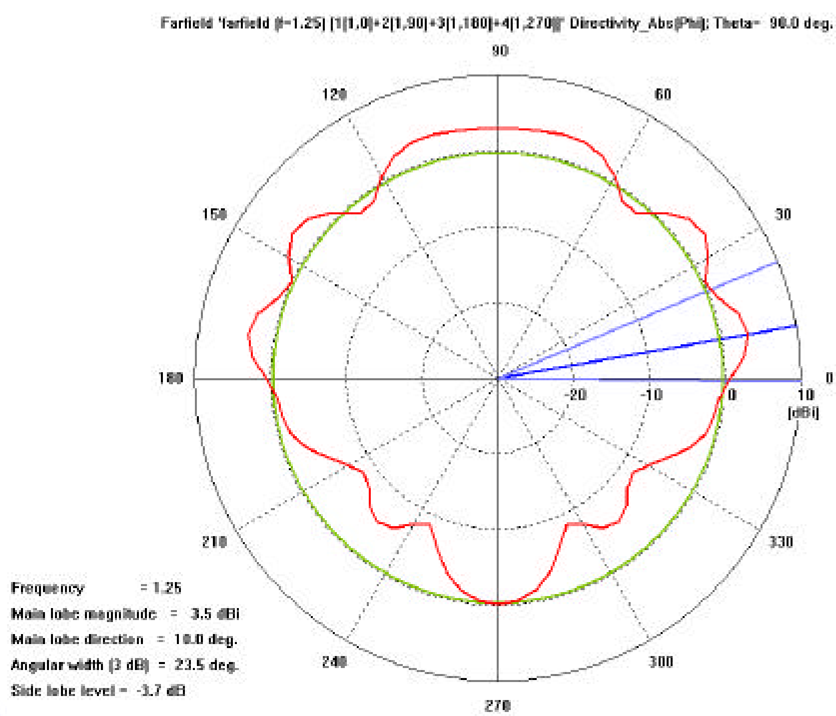

Figure 60. **Far-field directivity plot at $q = 90^{o}$ for the simulated QHA at 1.25 GHz.**

Figure 61 shows the input reflection coefficient for the QHA. It is evident that the bandwidth is large and spans several more octaves than the monofilar or bifilar. As with the monofilar and bifilar helix, as the modeled structure gets more complex, it utilizes more cells and, consequently, Microwave Studio is unable to simulate higher frequencies for that model. Figure 62 shows the far-field axial ratio in the y-direction. It is revealed that the radiation is circularly polarized around the y-axis, forming an axial beam symmetric to the y-axis at $q = 90°$ for f from $0°$ to $90°$ at 1.25 GHz. It is circularly polarized within $\pm 90°$ of $q = 90°$, a greater region than the bifilar helix.

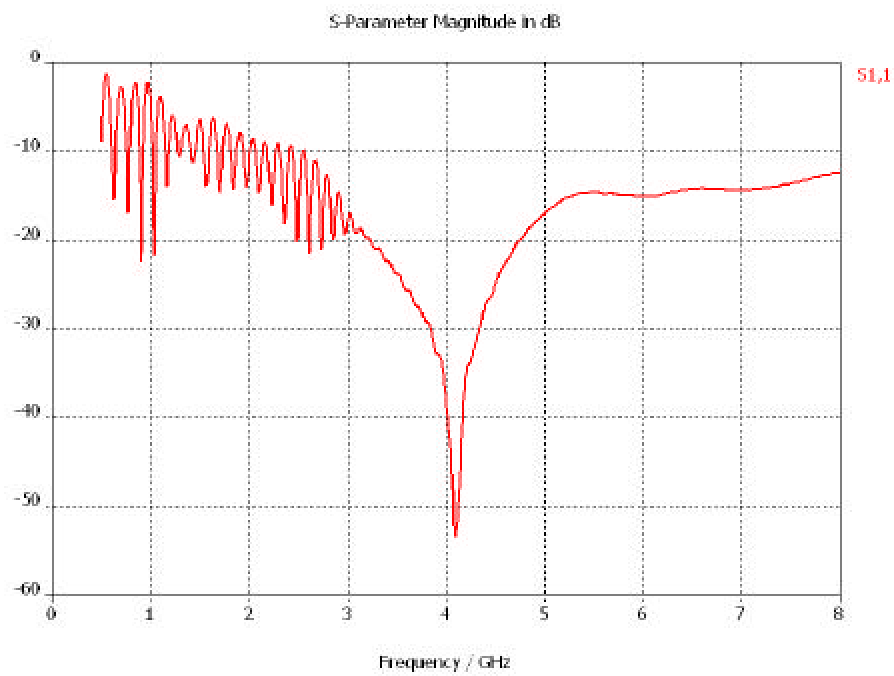

Figure 61. **Plot showing the variation of input scattering parameter (S_{11}) for the simulated QHA.**

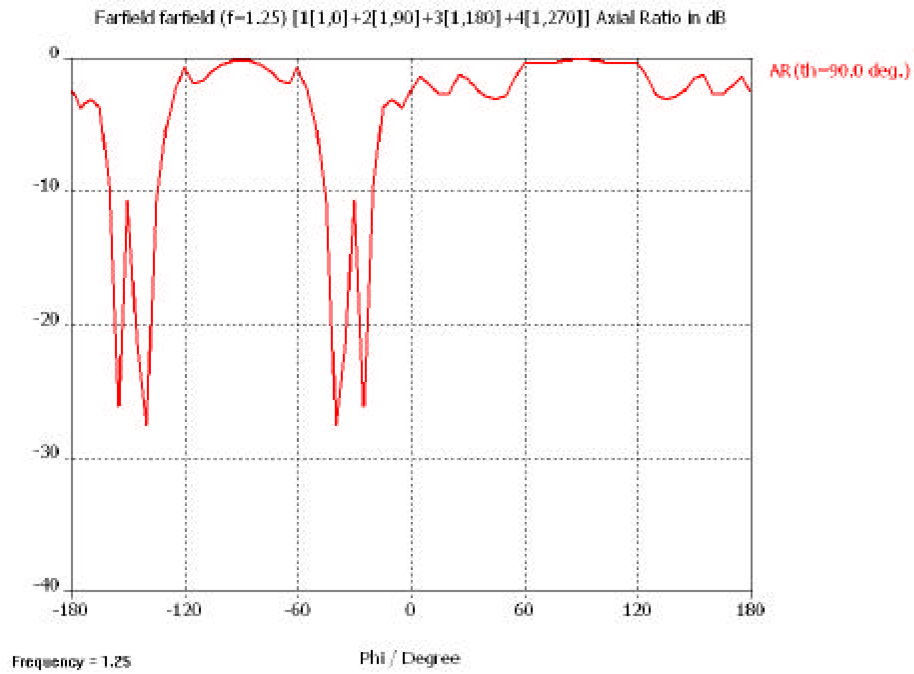

Figure 62. **Far-field axial ratio plot for the simulated QHA at 1.25 GHz.**

Figures 63 to 66 show how the beam pattern changes for different values of C/l. The quadrifilar helical antenna operates in the axial mode for $3/4 < C/l < 4/3$. For $C/l < 3/4$, the radiation is in the broadside mode, while for radiation patterns $C/l > 4/3$, it exhibits pattern break-up.

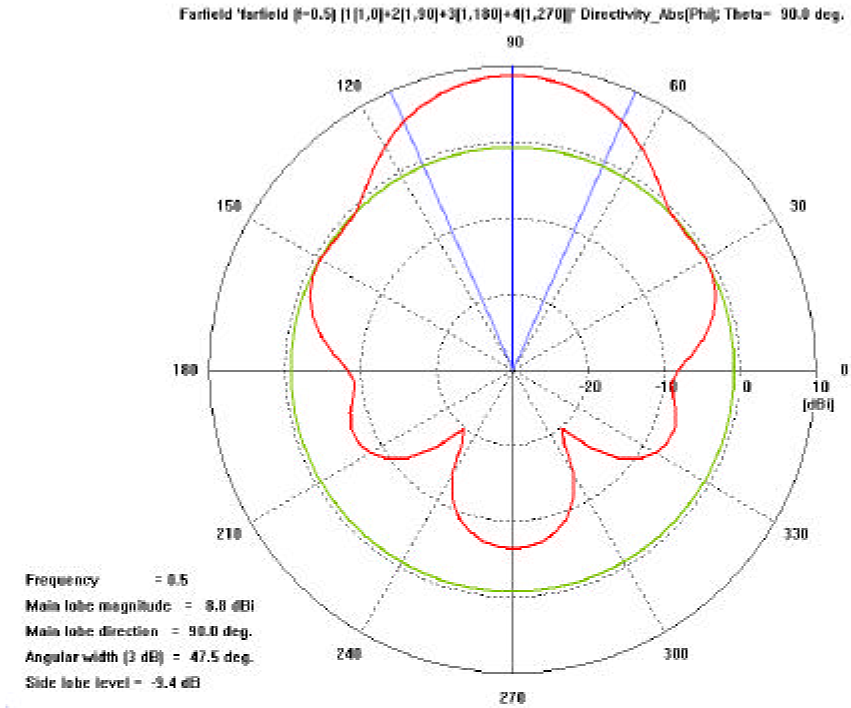

Figure 63. **Far-field directivity plot at $\theta = 90^\circ$ for the simulated QHA for $C/\lambda = 2/5\ (< 3/4)$.**

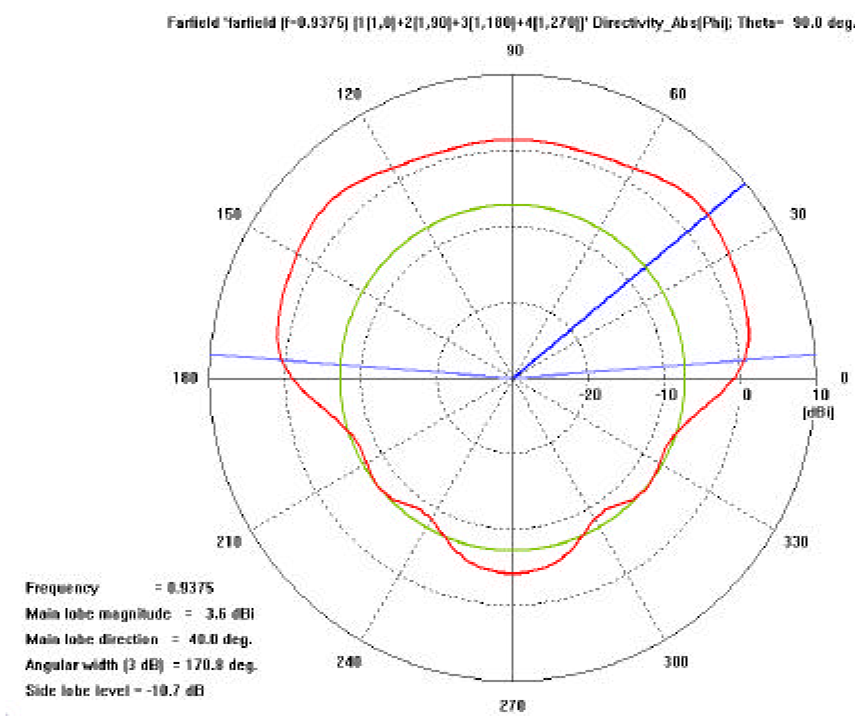

Figure 64. **Far-field directivity plot at $\theta = 90^\circ$ for the simulated QHA for $C/\lambda = 3/4$.**

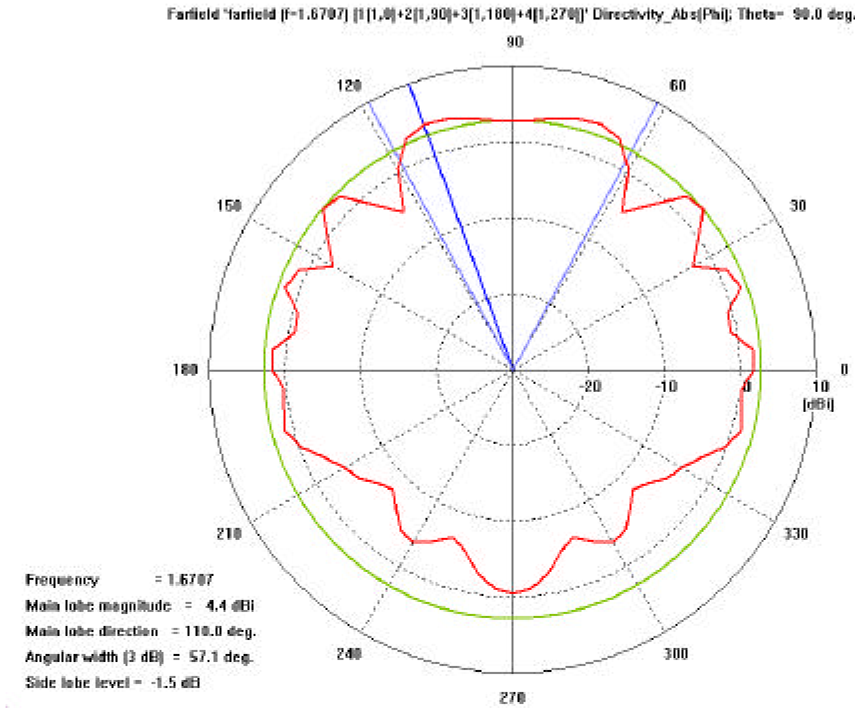

Figure 65. **Far-field directivity plot at $q = 90^{o}$ for the simulated QHA for $C/l = 4/3$.**

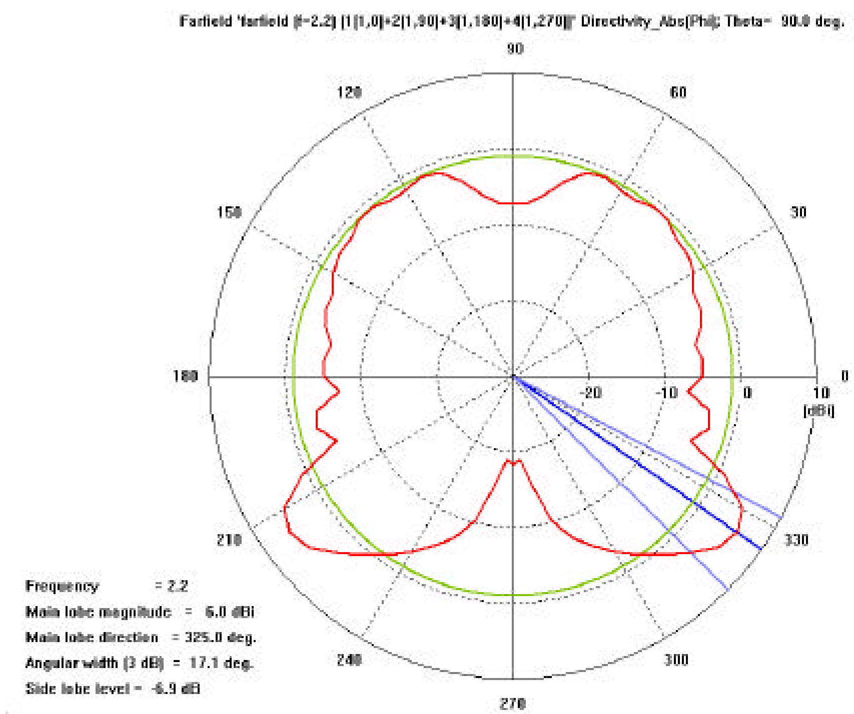

Figure 66. **Far-field directivity plot at $q = 90^{o}$ for the simulated QHA for $C/l = 9/5$ $(>4/3)$.**

Table 7 provides a summary of the performance parameters for the QHA, bifilar, and monofilar helix as obtained from Microwave Studio.

Performance Parameters	**Simulated Results**		
	QHA	**Bifilar Helix**	**Monofilar Helix**
Directivity at 1.25 GHz	3.6 dBi	11.45 dBi	11 dBi
Axial Ratio at 1.25 GHz	Circular (< 10 dB) at $f = 90^\circ$ and $0^\circ < q < 180^\circ$	Circular (< 10 dB) at $f = 90^\circ$ and $45^\circ < q < 135^\circ$	Circular (< 10 dB) at $f = 90^\circ$ and $45^\circ < q < 135^\circ$
S_{11} (< -10 dB)	From 2.0 GHz to > 8 GHz	From 1.8 GHz to > 6 GHz	From 1.2 GHz to > 7 GHz
Bandwidth (S_{11} at -10 dB)	> 6 GHz	> 5.2 GHz	> 5.8 GHz

Table 7. **Summary of the performance parameters for the simulated QHA, bifilar and monofilar helix.**

The QHA radiates in backfire for C/l in the range from 0.35 to 0.45. The bandwidth for backfire operation is about 15 to 30 percent. The break point (frequency at which broadband endfire patterns begin) occurs when C/l is between 0.40 and 0.45. The beam patterns in these ranges can be improved by adjustment of the ground plane diameter or pitch angle [33]. In the frequency range 1.6 < C/l < 2.7 the beam patterns begin to deteriorate slowly [33]. Various pattern defects appear. Complete pattern breakup occurs in the range 2.7 < C/l < 3.0. Other antenna characteristics such as impedance and axial ratio are satisfactory for C/l less than 2.7.

The pitch angle primarily affects the bandwidth [33]. As presented in Chapter III, the optimum pitch angle is about 35° to 40°. A comparison of the beam patterns at these pitch angles shows that the break point occurs at about the same frequency. The optimum ground-plane diameter is about three times the antenna diameter D for both the QHA and the CQHA [33].

Circu1ar ground planes were used in the simulations. The break point frequency decreases as ground plane size increases [33]. The small ground planes show poor beam

patterns while large ground planes show poor suppression of the scanning mode [33]. Directivity increases with increased axial length *L* as expected, but the beam patterns also change with *L* in other ways. In some cases, the shorter antennas had lower sidelobe levels in certain frequency ranges, or less beam splitting at the upper frequency limits.

At frequencies below the break point, the monofilar helix radiates in the normal (dipole) mode. Computational [28] and experimental resu1ts show that the QHA does not radiate in a normal mode because of the phase excitation $0°$, $90°$, $180°$, $270°$ of the windings. However, the excitation exp *(-j f)* is a type of supergain excitation [27], and the antenna *Q* is, therefore, an important, parameter in this frequency range.

D. COUNTER-WOUND QUADRIFILAR HELIX ANTENNA

Figure 20 shows the configuration structure for the uniform CQHA with a ground plane and a coaxial feed modeled using Microwave Studio. The only difference from the QHA was the addition of four oppositely wound arms which are positioned along the circumference of a slightly larger circle. Linear polarization is achieved with this second set of filaments that are wound in a sense opposite that of the first set as shown in Figures 20 to 22. Equation (3.9) describes the sequential phase variation required so that the radiation would add in phase, resulting in constructive interference and linear polarization. Figures 67 to 73 show various plots of the CQHA with a ground plane using the design parameters listed in Table 4(a) and the abovementioned phase excitations.

The radiation pattern for the CQHA is shown in Figures 67 and 68. The feed network is the most complicated aspect in the design of the CQHA. Figure 69 shows the input reflection coefficient for the CQHA. It is apparent that a matching network is required for an improved transmission coefficient. As the structure gets more complex, as it is for a CQHA, it utilizes more cells and consequently the software is unable to simulate higher frequencies.

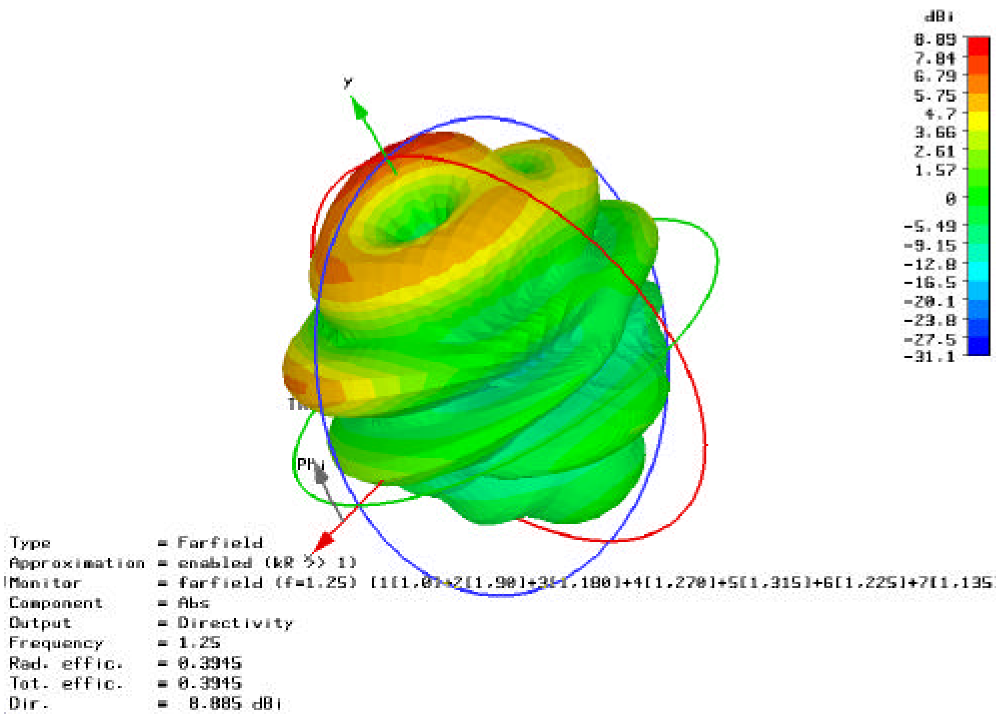

Figure 67. **Three-dimensional radiation pattern plot for the simulated CQHA at 1.25 GHz.**

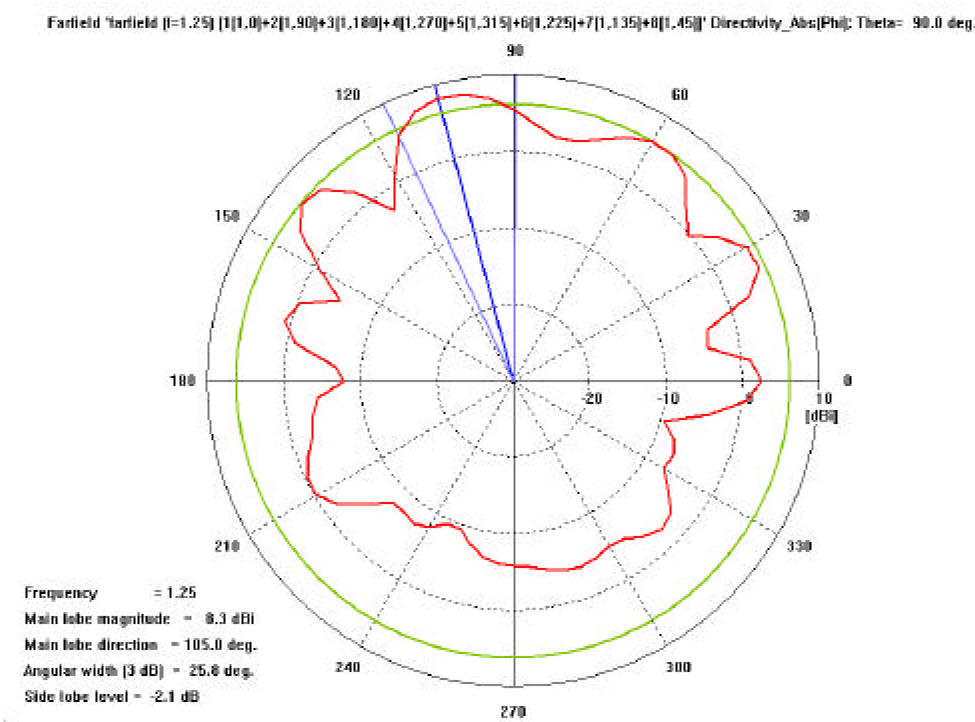

Figure 68. **Far-field directivity plot at $q = 90^{o}$ for the simulated CQHA at 1.25 GHz.**

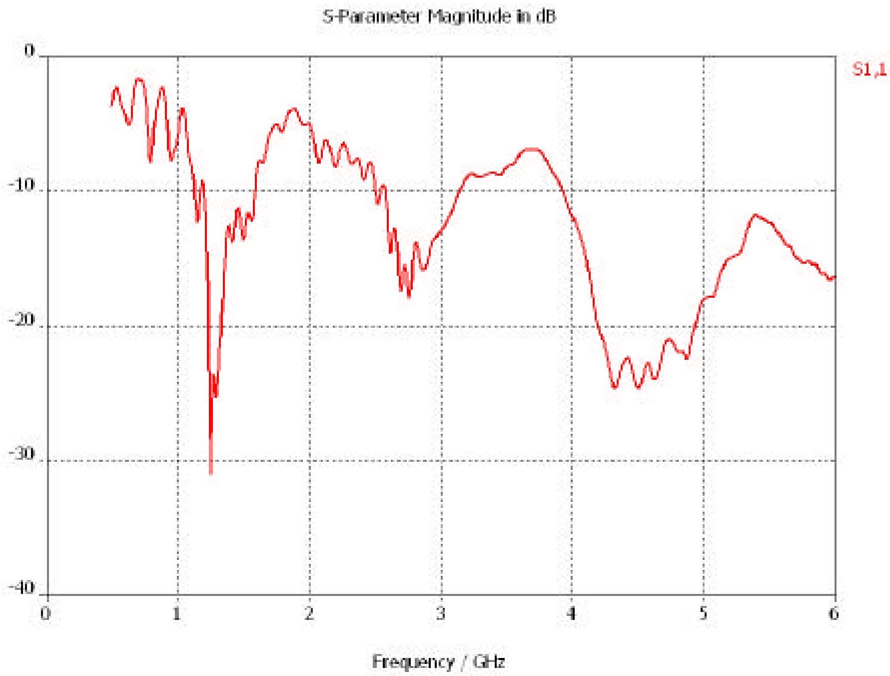

Figure 69. **Plot showing the variation of input scattering parameter (S_{11}) for the simulated CQHA.**

Figure 70 shows the far-field axial ratio in the *yz*-plane. It is evident that the radiation is linearly polarized around the *y*-axis at $q = 90^\circ$ at 1.25 GHz. It is linearly polarized within from $q = 60^\circ$ to $q = 115^\circ$. The counter-wound quadrifilar helix has a broad bandwidth and a linear polarization with a controllable plane of polarization from a planar geometry. The plane of polarization of the linearly polarized wave varies in f as a function of frequency.

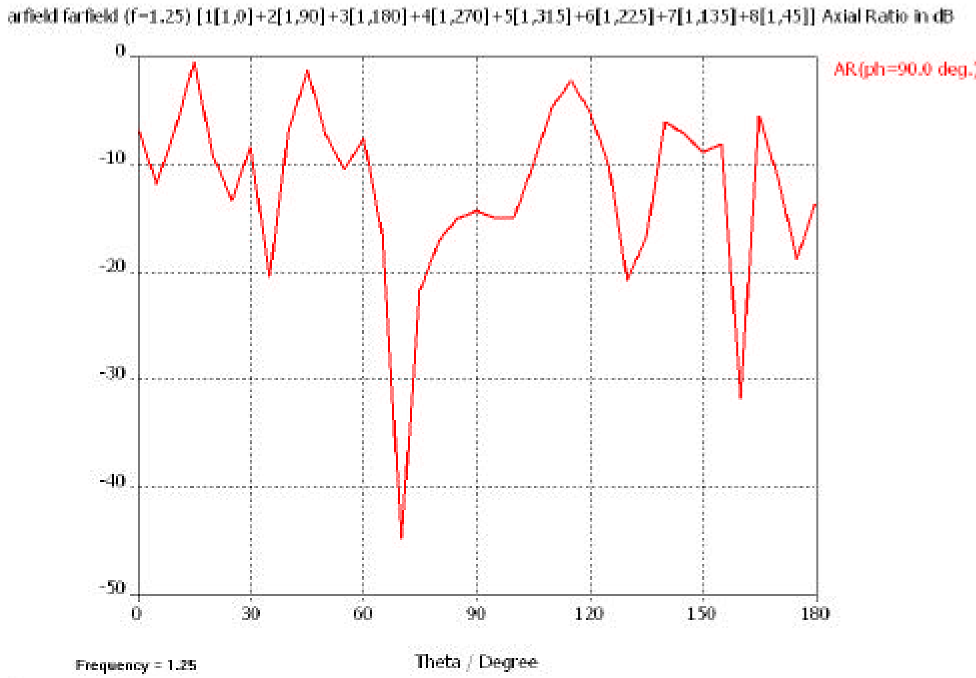

Figure 70. **Far-field axial ratio plot for the simulated CQHA at 1.25 GHz.**

Figures 71 to 73 show how the beam pattern changes for different values of C/l. The characteristics of the linearly polarized CQHA differ somewhat from those of the QHA. In particular, the "scanning" mode appears to be more effectively suppressed [33]. The beam pattern characteristics are shifted downward in frequency; both the break point and the upper frequency limit, occur at lower frequencies [33].

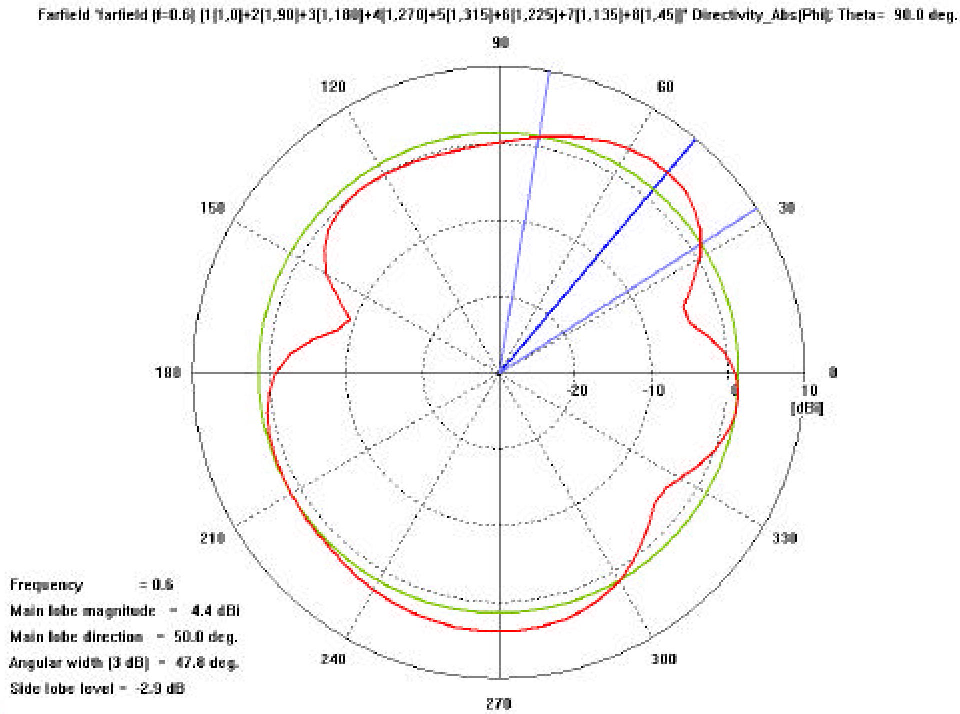

Figure 71. **Far-field directivity plot at $q = 90^o$ for the simulated CQHA for C/l =0.5 .**

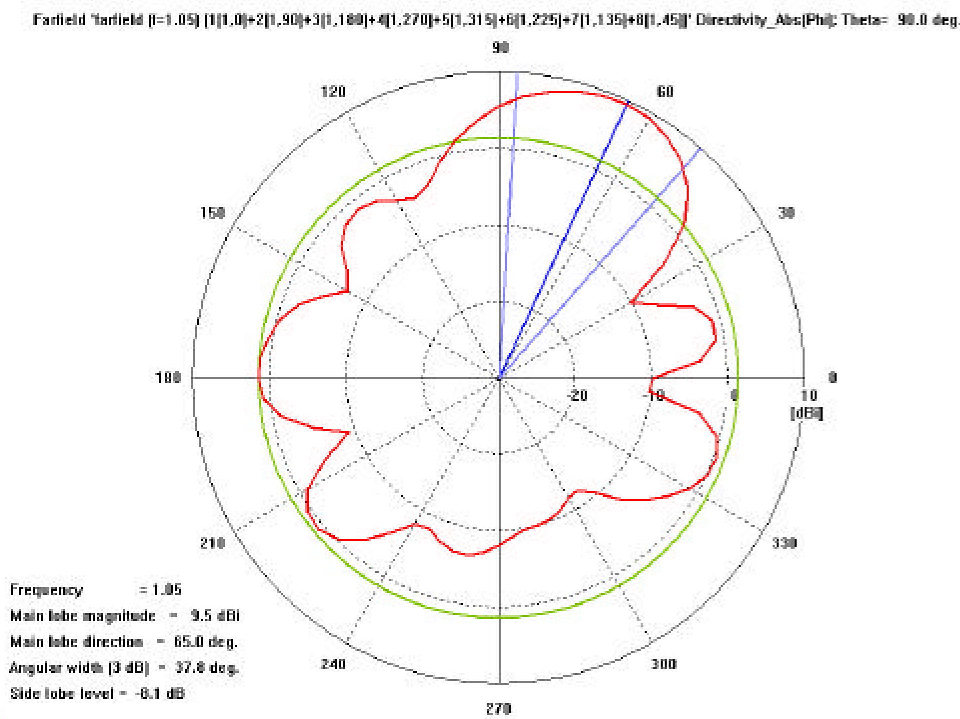

Figure 72. **Far-field directivity plot at $q = 90^o$ for the simulated CQHA for C/l =0.8 .**

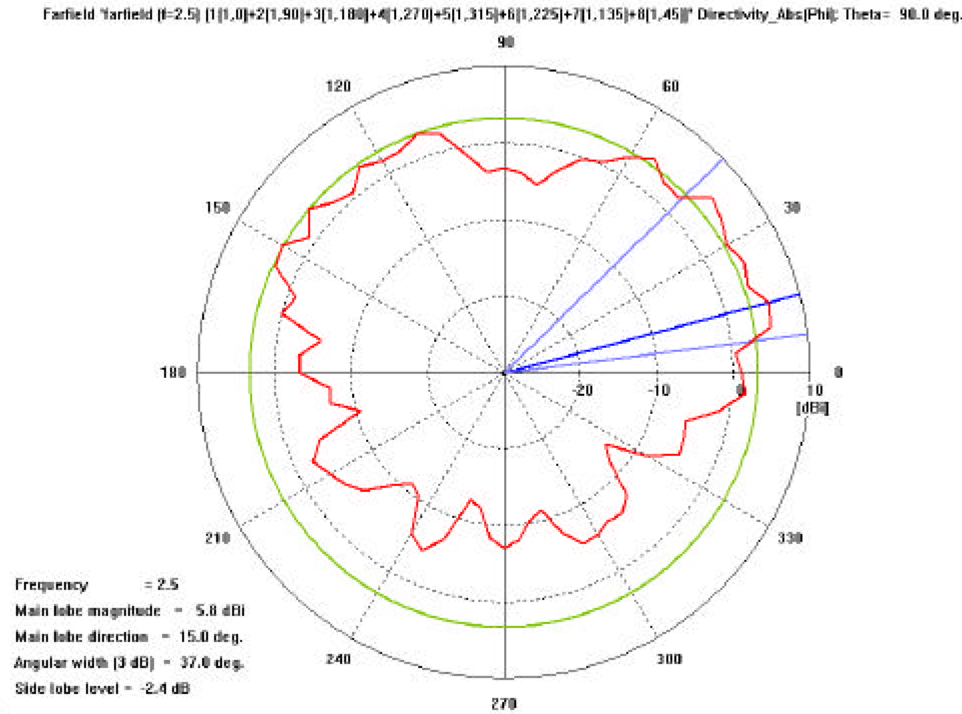

Figure 73. **Far-field directivity plot at $q = 90^o$ for the simulated CQHA for C/l =2 .**

E. SUMMARY

This chapter has verified several important aspects of the performance of the monofilar, bifilar, QHA and CQHA through a series of simulations. All of the single sense helices demonstrated circular polarization, and the CQHA linear polarization.

By adding more arms, as in the case of a bifilar or quadrifilar helix, wider bandwidth and a reduction of radiation in the back direction was achieved. Linear polarization for the CQHA was achieved by adding a second set of windings that were wound in an opposite sense to those of the first set. The CQHA far-field polarization has also been verified to be linearly polarized off-axis. However, the input reflection coefficient has not been optimized for a practical implementation. This can be achieved in two ways: (1) by controlling the size of the parameter values relative to the wavelength, especially the pitch and the helix wire diameter and, (2) by designing a balun (balanced-unbalanced) matching network between the helix and coaxial feed.

Employment of the CQHA can be extended to other applications where a large antenna bandwidth is required. The CQHA retains the wideband antenna characteristics of the helical antennas with an improved detection capability for a GPR by using linearly polarized (both vertical and horizontal) waves.

THIS PAGE INTENTIONALLY LEFT BLANK

V. CONCLUSION AND FUTURE WORK

A. CONCLUSION

This thesis project has addressed many issues pertaining to the design of ground penetrating radar systems, including the considerations and limiting factors imposed by the penetrated medium as well as the antenna perspective. The limitations predominantly depend upon the type of soils, its texture, soil water content, electrical properties and density, as well as operating frequency. It was observed that attenuation of the EM radiation increased with frequency for most types of materials. The reflections due to the returns from the air/ground interface can be reduced by using signal processing techniques.

The research investigated the factors contributing to the performance of the GPR radar system which resulted in a new antenna design, the CQHA, which is capable of dual-linear polarization over a wide bandwidth. The thesis discussed the various tradeoffs that must be made, and their implications for an overall improved design. The helical antenna for GPR applications was studied in detail. Parameters describing the helix were defined; their range of values for both the normal and axial modes was specified. The axial mode helix demonstrated the desirable characteristics necessary for an antenna for subsurface radar applications. The characteristics can be varied by controlling the parameter values relative to the wavelength.

By adding more arms, it was revealed that wider bandwidth and radiation in the back direction can be suppressed. Linear polarization was achieved by adding a second set of windings that are wound in an opposite sense to those of the first set, as demonstrated for the counter-wound quadrifilar helical antenna. The wave can be made horizontally or vertically polarized by varying the delay to the antenna feeds. This design allows buried objects with unknown aspect angle with respect to the antenna, to be detected by the radar system without large polarization loss. The CQHA design may be extended to other applications where large antenna bandwidth is required.

B. FUTURE WORK

The counter-wound helical antenna can be fabricated and its performance measured using the Network Analyzer and its radiation pattern measured in the anechoic chamber. The antenna patterns of the fabricated antenna can then be measured and compared with the theoretical values and simulation results. The matching between the complex feed network with the helix is a crucial design consideration. It will therefore be necessary to design a broadband balun for a superior performance. However, more simulations may need to be run to enhance the radiation pattern for the CQHA.

For the model discussed here, the air/ground interface was a smooth, planar surface. In practical applications, the interface could be rough and may even support various forms of vegetation. The effects of these factors on the performance of the GPR using CQHA can then be determined by measurement. The benefits of using this antenna structure for bistatic GPR have not been examined and is worthy of investigation.

LIST OF REFERENCES

[1] Scheck, W.C., “The Origins of Military Mines, Part I,” *The Engineer Bulletin*, Nov. 1998.

[2] Siegel, R., “Land Mine Detection,” *IEEE Instrumentation & Measurement Magazine*, Dec. 2002.

[3] IDA Document D-2416, Inst. Defense Analysis, “Research on Ground Penetrating Radar for Detection of Mines and Unexploded Ordnance: Current Status and Research Strategy,” Dec. 1999, p. ES-1.

[4] Jenn, D.C., “Ground Penetrating Radar,” lecture notes on Radar system, Naval Post Graduate School, 2003.

[5] Olhoeft, G.R., “Applications and Frustrations in Using Ground Penetrating Radar,” IEEE Transactions on Aerospace and Electronic Systems Magazine, vol. 17, no. 2, pp. 12-20, 2002.

[6] Hü lsmeyer C., 1904. Patent 165546. Deutschland.

[7] Hü lsenbeck. 1926. Patent 489434. Deutschland.

[8] “Mine/countermine Operations,” Field Manual 20-32, Hqtrs., Dept. U.S. Army, 29 May 1998.

[9] Gader, P.D, Frigui, H., Nelson, B.N., Vailette, G., Keller, J.M., “New Results in Fuzzy Set Based Detection of Land Mines With GPR,” *Proc. SPIE Conf. Detection and Remediation Technologies for Mines and Minelike Targets IV*, Orlando, FL, Apr. 1999, pp. 1075-1084.

[10] IDA Document D-2416, Inst. Defense Analysis, “Research on Ground Penetrating Radar for Detection of Mines and Unexploded Ordnance: Current Status and Research Strategy,” Dec. 1999, p. I-10 to 12.

[11] Daniels, D.J., Gunon, D.J., Scott, H.F., “Introduction to Subsurface Radar,” *IEEE Proceedings F on Radar, Sonar and Navigation*, vol. 135, no. 4, 1988.

[12] Jenn, D., “Plane Wave Transmission Lines and Waveguide,” lecture notes on Radio Wave Propagation, Naval Postgraduate School, 2003.

[13] Jenn, D., “Progress Report – Technical,” Naval Postgraduate School, 2003

[14] Lim, T.Y., “Broadband Counter-wound Spiral Antenna for Subsurface Radar Applications,” Naval Postgraduate School, Dec. 2003.

[15] Adams, A.T., Greenoungh, R.K., Wallenberg, R.F., Mendelovicz, A., Lumjiak, C., “The Quadrifilar Helix Antenna,” *IEEE Transactions on Antenna and Propagation*, vol. AP-22, No. 2, Mar. 1974.

[16] Olhoeft, G.R., “Electromagnetic Field and Material Properties in Ground Penetrating Radar,” 2nd International Workshop on Advanced GPR, 14-16 May 2003, Delft, The Netherlands.

[17] Mendelovicz, A., “Numerical Solution for Scattering and Radiation of a Quadrifilar Helix,” M.S. Thesis, Dep. Elec. Eng., Syracuse Univ., Syracuse, N.Y., Jun.1970.

[18] Leckebusch, J., “Ground Penetrating Radar: A Modern Three-Dimensional Prospection Method,” *Archaeological Prospection* vol.10, Issue 4, Oct./Dec. 2003, p. 213-240.

[19] Storme, M., Huynen, I., Vorst, A.V., “Characterization of Wet Soils from 2 to 18 GHz, Experimental Results,” In CLAWAR'98, pp.237-239, Brussels, Belgium, Nov. 1998.

[20] www.geo-centers.com/GPR/index.html accessed on 21 Oct. 2003.

[21] Fano, W.G., Trainotti, V., “Dielectric Properties of Soils,” 2001 Annual Report Conference on Electrical Insulation and Dielectric Phenomena, pp. 75-78, 2001.

[22] John, O.C., “Moisture Effects on the Dielectric Properties of Soils,” *IEEE Transactions on Geoscience and Remote Sensing*, vol. 39, no. 1, pp. 125-128, 2001.

[23] Peter, R.L., William, W.C., Kelly, S., “Studies of Ground Penetrating Radar Antennas”, 2nd International Workshop on Advanced GPR, pp. 24-29, 2003.

[24] Annan, A.P., Davis, J. L., Redman, J. D., "Detecting AP Mines Using Ground Penetrating Radar," Sensors and Software Inc, Y. Das, and D. Benson, Defense Research Establishment Suffield.

[25] Kraus, J.D., "Helical Beam Antenna," *Electronics*, vol. 20, pp. 109-111, Apr. 1947.

[26] Sensiper, S., "Electromagnetic Wave Propagation on Helical on Conductors," Res. Lab. of Electronics, Mass. Inst. Tech., Cambridge, Tech. Rept. No. 194, May 1951.

[27] Constantine, A., Balanis, *Antenna Theory Analysis and Design*, Harper and Row, 1982.

[28] Caswell, E. D., "Analysis of a Helix Antenna Using Moment Method Approach with Curved Basis and Testing Functions," Naval Postgraduate School, Sep. 2003.

[29] Rudge, A. W. *The Handbook of Antenna Design*, IEE Electromagnetic Waves Series, v. 15-16.

[30] Kraus, J.D., *Antennas*, 2nd Ed. ch. 7, McGraw Hill, 1988.

[31] Gerst, C., Worden, R.A., "Helix Antennas Take Turn for Better," *Electronics*, vol.39, no.17, pp.10-110, Aug. 1966.

[32] Gerst, C., "Multifilar Contrawound Helical Antenna Study and Analysis," Surveillance Technology Study and Analysis, vol. I Tech. Rep. RADC-TR-67-145, May 1967 and vol. II, Final Rep. Feb. 1967.

[33] Adams, A.T., Lumjak, C., "Optimization of the Quadrifilar Helix Antenna," *IEEE Transactions on Antenna and Propagation*, July 1971.

[34] Lamensdorf, D., Smolinski M.A., IEEE 2002.

[35] Kilgus, C.C., "Resonant Quadrifilar Helix Design," *Microwave Journal*, vol. 13-12, pp.49-54, Dec. 1970.

[36] Kilgus, C.C., "Shaped-Conical Radiation Pattern Performance Check of the Backfire Quadrifilar Helix," *IEEE Trans. Antennas Propagation*, vol. AP-23, pp.393-397, May 1975.

[37] Tranquilla, J.M., Steven, R.B., "A Study of the Quadrifilar Helix Antenna for Global Positioning System (GPS) Applications," *IEEE Transactions on Antennas and Propagation*, Vol. 38, No. 10, p.1545, Oct. 1990.

[38] Lumjak C., "An Experimental Study of the Quadrifilar Helix Antenna," M.S.E.E. Thesis, Syracuse Univ., Syracuse, N.Y., Nov. 1969.

[39] Petros, A., Licul, S., "Folded Quadrifilar Helix Antenna," Bradley Department of Electrical and Computer Engineering.

[40] Terada, N., Kagoshima, K., "Backfire/Endfire Radiation Performance of Quadrifilar Helical Antennas," *Electronic Letters* vol.27, No.12, Apr. 1991.

[41] Kraus, J.D., "The Helical Antenna," *Proc. IRE*, vol. 37, pp. 263-272, Mar. 1949.

[42] Johnson, R.C., *Antenna Engineering Handbook*, 3rd Ed. New York, McGraw-Hill, ch.4 and 6, 1993.

[43] Nakano, H., Masui, N., Ikeda, H., Yamauchi, J., "Monofilar and Quadrifilar Helical Antennas Wound on Dielectric Rods," Faculty of Engineering, Hosei University, Tokyo, Japan.

[44] Leach, S.M., Agius, A.A., and Saunders, S.R., "Intelligent Quadrifilar Helix Antenna", *IEEE Proc. Microwave Antennas Propagation*. Vol. 147, No. 3, Jun. 2000.

[46] Harrington, R.F., *Time-Harmonic Electromagnetic Fields*, New York, McGraw-Hill, p. 211, 1961.

INITIAL DISTRIBUTION LIST

1. Defense Technical Information Center
   Ft. Belvoir, Virginia

2. Dudley Knox Library
   Naval Postgraduate School
   Monterey, California

3. Professor Dan C. Boger, Chairman, Code IS
   Department of Information Sciences
   Naval Postgraduate School
   Monterey, California

4. Professor David C. Jenn, Code EC/jn
   Department of Electrical and Computing Engineering
   Naval Postgraduate School
   Monterey, California

5. Professor Daniel C. Schleher, Code IW
   Department of Information Sciences
   Naval Postgraduate School
   Monterey, California

6. W.T. Wollny
   Quick Reaction Corporation
   P.O. Box 1023
   Pebble Beach, CA93953

7. Dilipkumar Shivandas
   Republic of Singapore Air Force, MINDEF
   Singapore